National & Kapodistrian
University of Athens
Department of Physics
Section of Astrophysics, Astronomy and Mechanics

MSc Thesis

Hadronic signatures of baryon-loaded AGN jets

Filippos-Panteleimon Psarras
AM:2020302

Supervisor:
Maria Petropoulou

Co-Supervisors:
Apostolos Mastichiadis
Nektarios Vlahakis

Athens 2022

Contents

Acknowledgements

This thesis is a result that is accomplished by the help of a group of people. First and foremost, i would like to thank my supervisor, Dr. Petropoulou M., for introducing me to this project, for helping me and investing a lot of time in this work, and for her patience with me. I would also like to thank Dr. Mastichiadis and Dr. Vlahakis, who inspired me as a student to follow astrophysics, and who also happen to be the rest of my thesis committee. Last, but not least, i would like to thank my friend and colleague, Stamatios I. Stathopoulos, for our conversations throughout this project, that helped me and gave me courage.

Abstract

Blazars are the most energetic subclass of active galactic nuclei (AGN) with relativistic jets pointing towards the observer. It is believed that jets are launched as cold non-relativistic Poynting-flux dominated outflows which accelerate to relativistic speeds at the expense of the available magnetic energy. Part of this energy is also thought to be converted into energy of non-thermal particles. In this work, we consider electron-proton jets and assume that particles are energized via magnetic reconnection in parts of the jet where the plasma magnetization is still high, namely $\sigma \geq 1$. Particle-in-cell simulations of reconnection have shown that the power-law slope of the particle energy distributions depends on σ, while the amount of energy transferred into relativistic protons and electrons is roughly constant. Neutrino production is also expected to occur via photohadronic interactions between relativistic protons and photons. In our calculations, we worked under the assumption that all jets are launched with the same total energy flux per unit rest-mass energy flux, μ. This relates to the plasma magnetization and bulk Lorentz factor as $\mu = (\sigma + 1)\Gamma$. We adopt an observationally motivated relation between Γ and the mass accretion rate $\dot{m}$, which also controls the luminosity of external radiation fields. We compute self-consistently the multi-messenger emission from blazar jets as a function of μ, σ, and $\dot{m}$, and present our results for BL Lac objects and flat spectrum radio quasars.

1 Introduction

Starting this thesis, we will present some fundamental information about the objects that will be further investigated, known as Active Galactic Nuclei (AGN).

1.1 Active Galactic Nuclei

AGN are astrophysical objects that constitute a small fraction ($\sim 10\%$) of galaxies in our Universe. The distinctive factor between AGN and other normal galaxies is that they are able to produce very high luminosities in a very concentrated volume, through different physical processes other than nuclear fusion that occurs in stars. In fact, it is universally accepted that AGN emission is related to the presence of an actively accreting supermassive ($\geq 10^6 M_\odot$) black hole (SMBH). Furthermore, we present below some basic characteristics of AGN:

- High bolometric luminosity, up to $L_{bol} \simeq 10^{49}$ erg/s. For comparison, this is 3 or more orders of magnitude higher than the respective luminosity of Milky Way.
- Detectable emission covering the whole electromagnetic spectrum.
- Emission lines in Ultraviolet(UV)/Optical frequencies, produced in high density clouds of gas moving in Keplerian orbits, in the potential of the black hole.
- Non-thermal radiation that extends in many orders of magnitude (namely observed from radio waves to γ-rays).
- A fraction of AGN present fast variability in their emission profile and a central radio jet associated with high γ-ray energy emission and particle acceleration.

1.2 Components of a typical AGN

The basic components of an AGN (Fig.1) are summarized below.

- A SMBH at the center ($10^6 M_\odot \leq M \leq 10^{10} M_\odot$), which pulls matter from the surroundings due to its strong gravitational field.
- An accretion disk which is formed by the infalling matter to the SMBH. As matter accretes, part of the gravitational energy that is lost is released as radiation from the disk.
- An X-ray corona between the accretion disk, that is composed of hot plasma that Comptonizes the UV/optical disk radiation in order to produce hard X-rays (usually up to 100 keV).
- An obscuring torus located at several ($1 - 10$ parsec (pc)[1]) from the SMBH. It is a cold dusty structure that intercepts some fraction of radiation which is produced by the disk and re-emits it at the infrared (IR) band.

[1] $1pc \simeq 3 \times 10^{18}$cm

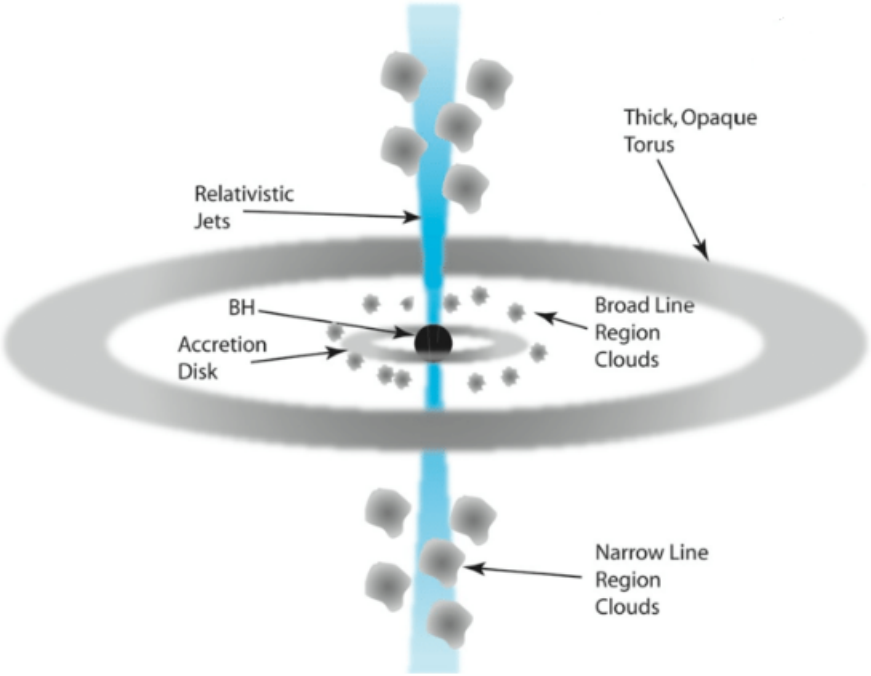

Figure 1: Schematic represantation of an active galactic nucleus. Taken from [69]

- A region of small rapidly moving ($\sim 1000km/s$), dense ($\sim 10^{10}cm^{-3}$) gas clouds at $\sim 0.1 - 1pc$ from the SMBH. A fraction ($\sim 10\%$) of the disk radiation is processed by these clouds resulting in observing emission lines in the spectra. These lines are broadened eventually due to Doppler shifting. This region is known as Broad Line Region (BLR).
- A similar region, but with less dense ($\sim 10^{3}cm^{-3}$) gas clouds at a large distance ($\sim 100pc$) from the SMBH. This region is responsible for the narrow lines in the spectra and this is why it is known as Narrow Line Region (NLR).
- A fraction of AGN ($\sim 10\%$) that besides accreting matter, has the ability to expel it in two oppositely directed jets. Jets are thought to originate from the vicinity of the SMBH and can extend up to kiloparsec distances. These jets are carrying electromagnetic fields and plasma that moves with relativistic speeds.

First, we take a closer look at the accreting SMBH. The luminosity of the accretion disk depends on the amount of the mass accretion rate $\dot{M}$. The efficiency of this process is defined as the fraction of rest mass energy that is converted into radiation, before being swallowed by the SMBH. The value that is often adopted for this parameter is $\eta \sim 0.1$ ([19],[6]).

$$L_{disk} = \eta \dot{M} c^2 \tag{1.1}$$

However, L_{disk} cannot be arbitrarily high. There is an upper limit which is known as Eddington luminosity and it applies when radiation pressure balances gravity, regarding spherical accretion

and electron-proton plasma. It is defined as:

$$L_{Edd} = \frac{4\pi c G M_{BH} m_p}{\sigma_T} = 1.26 \times 10^{38} \frac{M}{M_\odot} \text{ erg/s} \tag{1.2}$$

The "standard" accretion disk is relatively cold, meaning that even the inner regions cannot reach $\sim$ keV temperatures. Knowing that AGN are powerful X-ray emitters ([36]), one has to assume the presence of another component that is responsible for this emission. Without getting into details, the observed X-ray spectrum could be approximated by a power law (ending in an exponential cut-off) which is explained by thermal Comptonization ([81]).

As we mentioned, the presence of emission lines in the UV/optical frequencies is a result of the BLR and NLR. Typical value of temperature is about 10^4 K, which applies for the NLR, too. Regarding the BLR, for a typical AGN, the most prominent lines are Hydrogen Lyα, and lines from partially ionised C, Mg, O and Ha. Moreover, there is another parameter called the covering factor that can be estimated by calculating the luminosity of the lines divided by the continuum luminosity. Typical values is 0.1 for BLR and 0.01 for NLR ([29]).

Jets produce non-thermal emission across the electromagnetic spectrum (see Fig. 2). The bolometric jet luminosity is either dominated by X-ray or γ-ray emission. In addition to the electromagnetic (Poynting) component of the jet, its total power is carried by plasma that moves relativistically. It is important to state that since the material is macroscopically moving with a bulk Lorentz factor Γ, its radiation will be beamed and therefore amplified for an observer looking at a small angle with respect to the jet axis (see Appendix A). Jet plasma will, eventually, reach sites known as radio lobes. Radio lobes are extended structures that are located tens of kpc from the central engine and have similar values of radius. They emit mainly in radiowaves with power-law spectra. It is believed that the radio emission of the lobes is synchrotron radiation by relativistic electrons.

1.3 AGN Types

AGN can be classified into subcategories, using different observational criteria, such as their radio power and presence of emission lines. In the latter case, AGN are identified as narrow or broad line objects, while radio power is a criterion that divides AGN into radio-loud and radio-quiet. Moreover, objects in these categories can be further divided, as described below.

1.3.1 Seyfert Galaxies

In 1943, Seyfert identified the first class of AGN. These objects showed very bright nucleus with broad emission lines. They were, also, found at in low redshifts and were mainly hosted by spiral galaxies. Seyfert galaxies belong to the radio-quiet class of AGN and they are further divided into two subcategories, based on the width of their emission lines. The Seyfert 1 type has broad and narrow emission lines, while, Seyfert 2 present only narrow lines. After the launch of Fermi γ-ray space telescope sattelite, variable γ-ray emission from a few radio-loud narrow-line

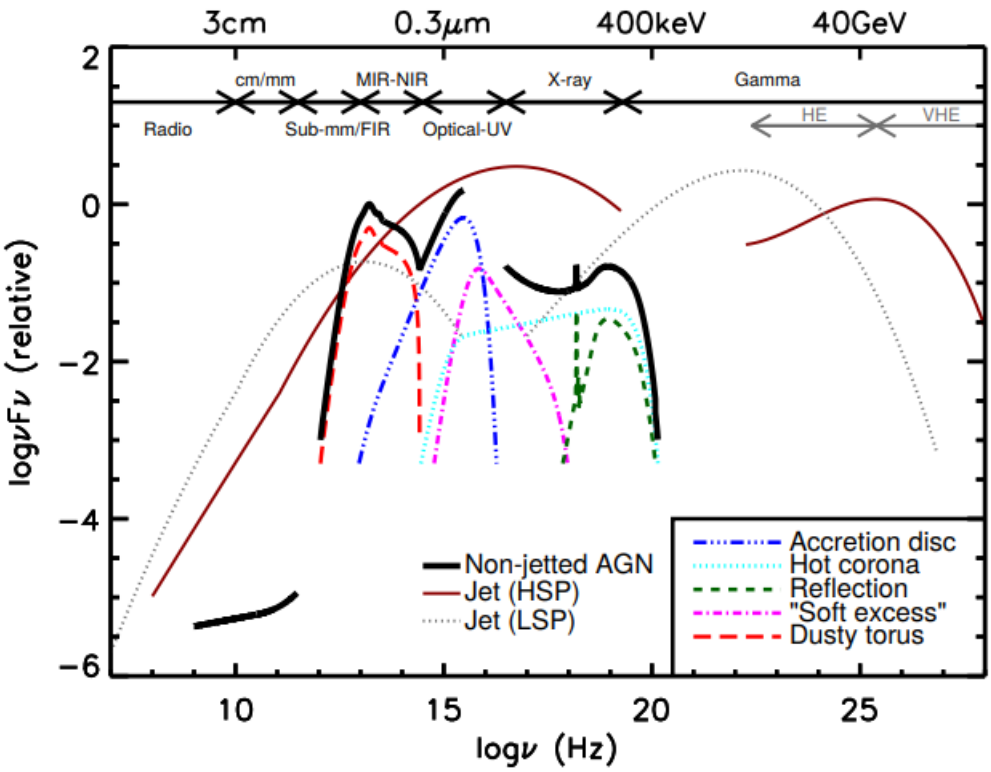

Figure 2: Schematic representation of an AGN spectral energy distribution (SED), loosely based on the observed SEDs of non-jetted quasars. The black solid curve represents the total emission and the various coloured curves (shifted down for clarity) represent the individual components. The primary emission from the AGN accretion disk peaks in the UV region. The jet SED is also shown for a high synchrotron peaked blazar (HSP) and a low synchrotron peaked blazar (LSP). Adapted from [34]

Seyfert 1 Galaxies (NLSy1), was discovered. Specifically, the fourth Fermi-LAT source catalog (4FGL [2]) presented nine NLSy1, with range of luminosity values of blazars, in particular of FSRQs. ([55],[18])

1.3.2 Low-Ionization Nuclear Emission Line Region (LINERs)

LINERs are objects that show only weak nuclear emission line-regions. It is not clear if these objects are actually AGN, since there are not other signatures of typical AGN emission. These are the lowest luminosity objects of radio quiet AGN.

1.3.3 Quasars

In 1960s there were found sources that were initially considered to be stars, since their spectra presented broad and narrow lines, but they could not be specified. Eventually, M. Schmidt examining the object 3C273, identified that these lines correspond to Balmer lines of Hydrogen ([70]). The difficulty in identifying these lines was due to their high redshift ($z = 0.158$), which

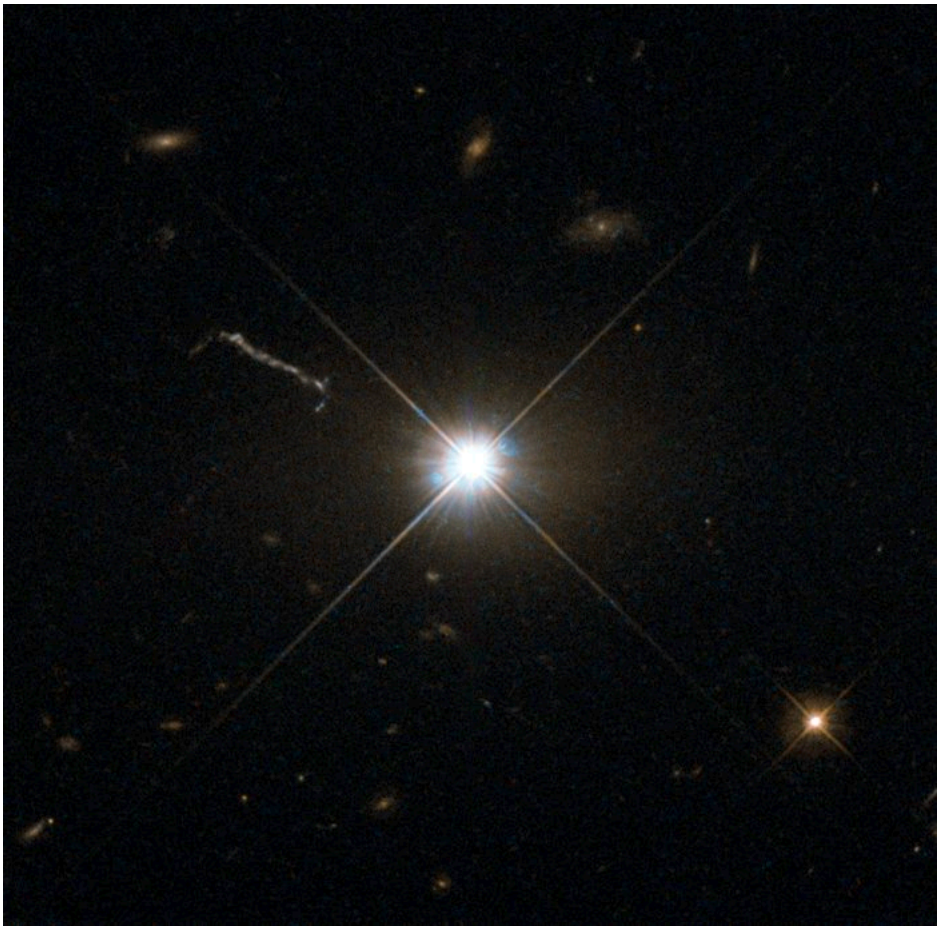

Figure 3: The bright quasar 3C 273 (Credit: ESA/Hubble & NASA)

means that these objects are so bright, that could exceed the Milky Way luminosity by thousand times. Quasars are similar to Seyfert 1 objects, but are more distant and brighter. In later years, it was found that quasars can be either radio-loud or radio-quiet. Most of them belong in the latter case (only $\sim 10\%$ is radio-loud) and are called quasi-stellar objects (QSO). They also show optical and X-ray continuum emission (see Fig.3) and they present optical emission lines, as well. On the other hand, emission from radio-loud quasars present an additional component that comes from their jets and radio lobes.

1.3.4 Radio galaxies

In general, radio galaxies (Fig.4) are distant objects, usually found in elliptical galaxies that strongly emit in radiowaves. This emission is mainly non-thermal and is explained by synchrotron radiation from relativistic electrons, but they also present emission lines in optical wavelengths. Based on the width of the lines they are further divided into broad line radio galaxies (BLRG) and narrow line radio galaxies (NLRG). Radio galaxies can be further divided into two categories; FRI and FRII, named after Fanaroff and Riley ([23]). This division is based upon the morphology and brightness of the jet. In particular, FRI objects have brighter jets, while FRII present brighter radio lobes. Furthermore, from an observational point of view, FRI appear to have two faint jets, while in the FRII case, there is one bright jet.

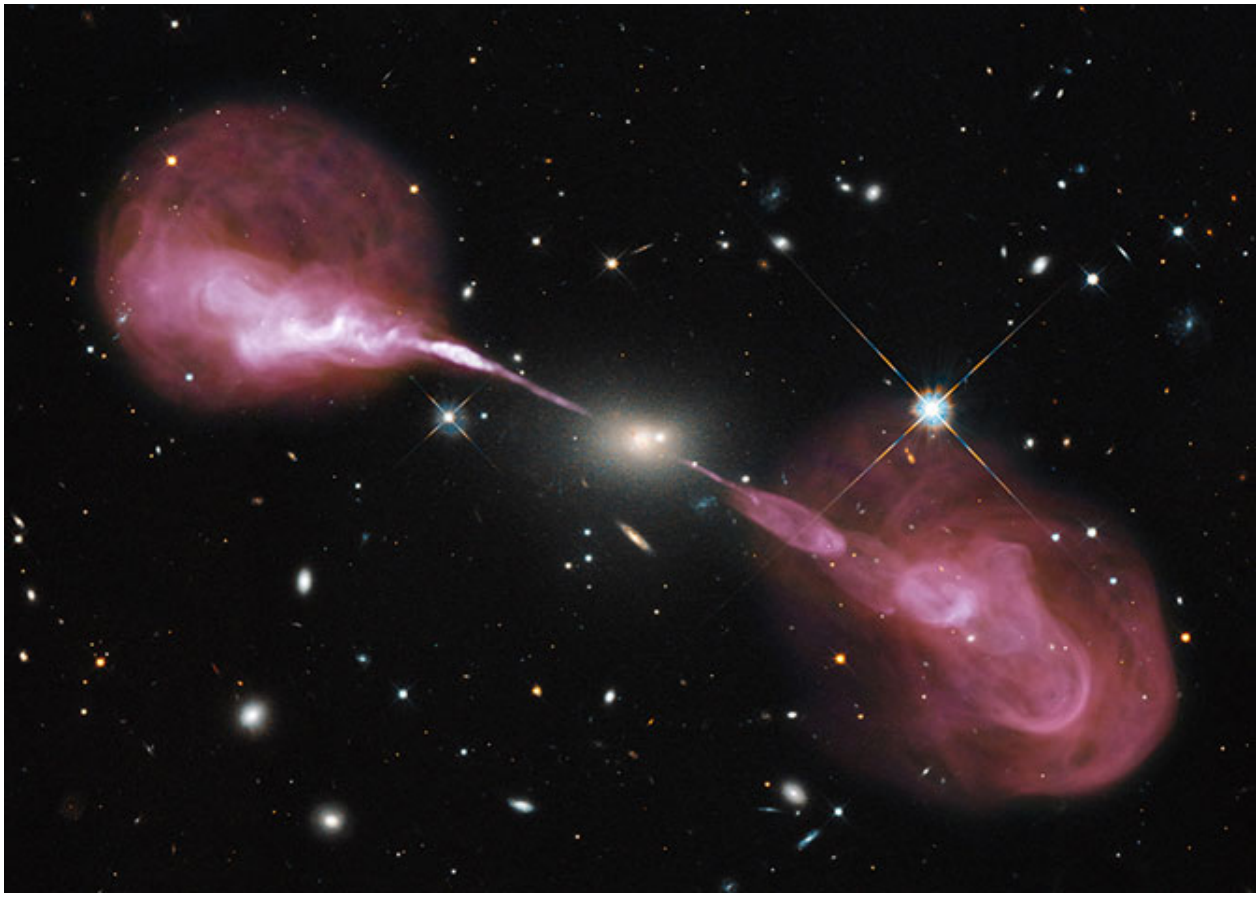

Figure 4: The elliptical radio galaxy Hercules A illustrated with the combined imaging power of the Hubble Space Telescope's Wide Field Camera 3 and the recently upgraded Karl G. Jansky Very Large Array (VLA) radio telescope in New Mexico. (Credit: NASA, ESA, S. Baum and C. O'Dea (RIT), R. Perley and W. Cotton (NRAO/AUI/NSF), and the Hubble Heritage Team (STScI/AURA))

1.3.5 Blazars

Blazars are the most energetic subclass of AGN, having relativistic jets pointing towards the observer. This leads to the amplification of their observing luminosity, due to relativistic effects. Blazar emission extends from from radiowaves to γ-rays and is mainly non thermal.The SED is composed of two main components; a lower energy one, whose emission is maximised in the frequency range of IR to soft X-rays, and a higher energy one whose emission peaks at γ-rays.

Blazars are also classified into two subcategories: BL Lacertae (BL Lac objects) and flat spectrum radio quasars (FSRQs). Their main difference is the existence of optical emission lines, which are found in FSRQs. Examining the SED from typical objects of these categories, the low energy component is attributed to synchrotron radiation, while the high energy component is thought to be produced by the Inverse Compton process. Usually, in FSRQs the seed photons for this interaction are considered to be external (BLR), in contrast to BL Lacs where the seed photons are the ones produced by synchrotron emission, i.e. synchrotron-self Compton

(SSC) process. Another criterion for classifying blazars is the frequency where the synchrotron component is peaked. For low values of $\nu_{syn,pk}$ ($\leq 10^{14}$ Hz) objects are classified as LBLs (Low-frequency peaked BLazars), in contrast to HBLs (High-frequency peaked BLazars) where $\nu_{syn,pk}$ takes higher values ($\geq 10^{15}$ Hz).

The blazar sequence

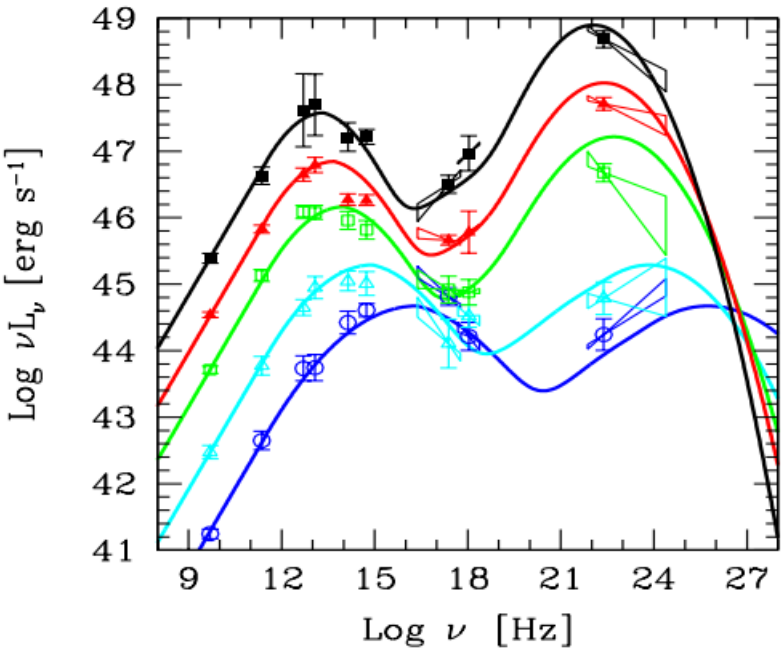

Figure 5: The blazar sequence. Adapted from [24]

Fossati et al. (1998) ([24]) studied a total number of 126 blazars, where 33 of them were detected in γ-rays by EGRET. This study showed a connection between the observed bolometric luminosity and the shape of the blazar SED. More specifically, the luminosity of the lower energy component appears to anti-correlate with the peak synchrotron frequency, $\nu_{syn,pk}$ (see Fig.5). In particular, low power blazars (namely BL Lac objects) are bluer (meaning that have large peak frequencies) than powerful blazars (FSRQs). Moreover, the high energy hump is getting more dominant as the bolometric luminosity increases (Fig. 5).

In more recent studies ([27],[63]), which revisit the blazar sequence is reported that FSRQs display approximately the same SED as the luminosity increases, with increased relative importance of the high energy peak, which leads to hard X-ray spectra. Regarding BL Lacs, the sequence is still confirmed, since their peak shifts to lower frequencies for higher luminosities. A difference with the original sequence is that BL Lacs present a steeper average γ-ray slope than it was originally found. Also, at high luminosities, a large fraction of FSRQs shows signs of thermal emission from the accretion disk, in the optical-UV.

Another blazar correlation, discovered in Fermi-LAT data, constitutes an additional division between FSRQs and BL Lac objects. Examining the γ-ray spectral index α_γ, measured in the range of $0.1 - 100$ GeV and plotted as a function of γ-ray luminosity (Figure 6), shows that

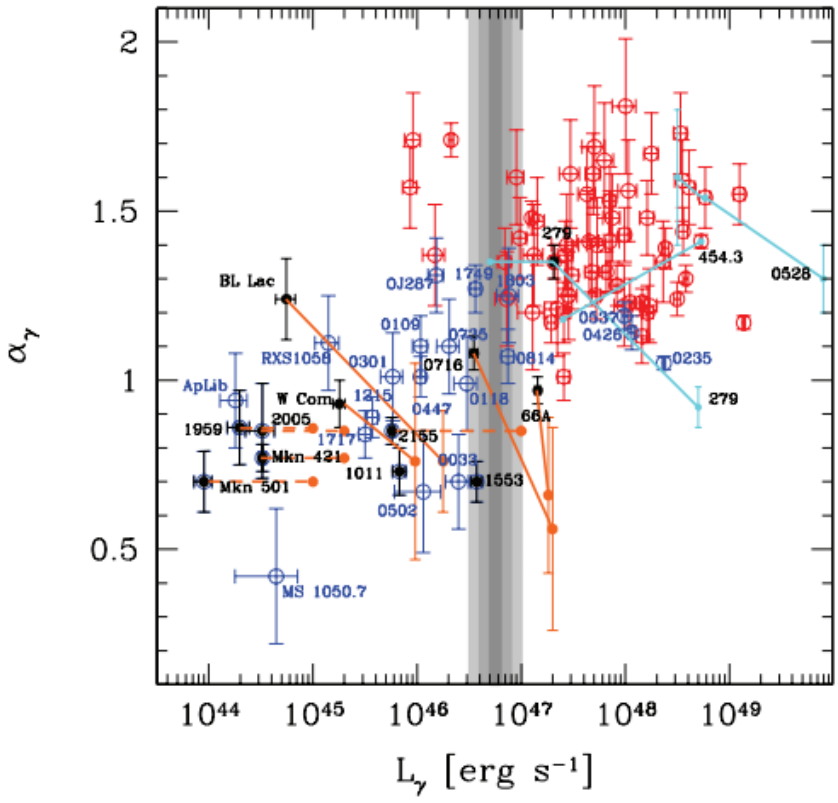

Figure 6: Energy spectral index versus γ-ray luminosity for blazars in the list of Abdo et al. (2009). Blue and red points are BL Lacs and FSRQs, respectively. The grey stripes at about $L_\gamma = 10^{47}$ erg/s mark the divide between BL Lac objects and FSRQs. Taken from ([26])

most FSRQs have $\alpha_\gamma \geq 1.2$ and $L_\gamma \geq 10^{46}$ erg/s, while the reverse values correspond to BL Lacs. This separation is known as the blazar divide.

1.4 Unification model

As we already described, there is a lot of diversity in AGN. However, there are some similarities among them, which led to attempts of unifying AGN types. the most widely adopted unification scheme is the one proposed by Urry and Padovani (1995) ([78]) and according to it, one can determine any AGN type, based on the intrinsic strength of its radio emission and the angle that the observer sees an object like this (Fig.7).

Starting with the radio-quiet AGN, it is already mentioned that in this case, jets cannot be observed, so the types that belong in this category can only be Seyfert galaxies and QSOs. Regarding Seyferts, if our line of sight is close to the rotational axis of the accretion disk, then we will observe broad and narrow emission lines, that correspond to the case of Seyfert 1. On the other hand. if the observations are close to the equatorial plane, then the torus will absorb BLR radiation, which will result to observing only narrow emission lines, as it happens in Seyfert 2 AGN. Lastly, QSOs have similar emission features as Seyferts 1, but are much brighter.

Blazars and radio galaxies are included in radio-loud AGN. In this case, the unification scheme can be performed again by examining the observing angles. Regarding radio galaxies, if our line of sight is perpendicular to the jet, then only narrow emission lines will be observed. However, if we get closer to observing the jet emission axis, there will be observed broad emission lines, too. On the other hand, in blazars, jets are observed within small angles in respect to the line of sight. Also, based on their low luminosity and similar radio emission, one can correlate BL-Lac objects with FRI radio galaxies (and in the same manner FRII with FSRQs).

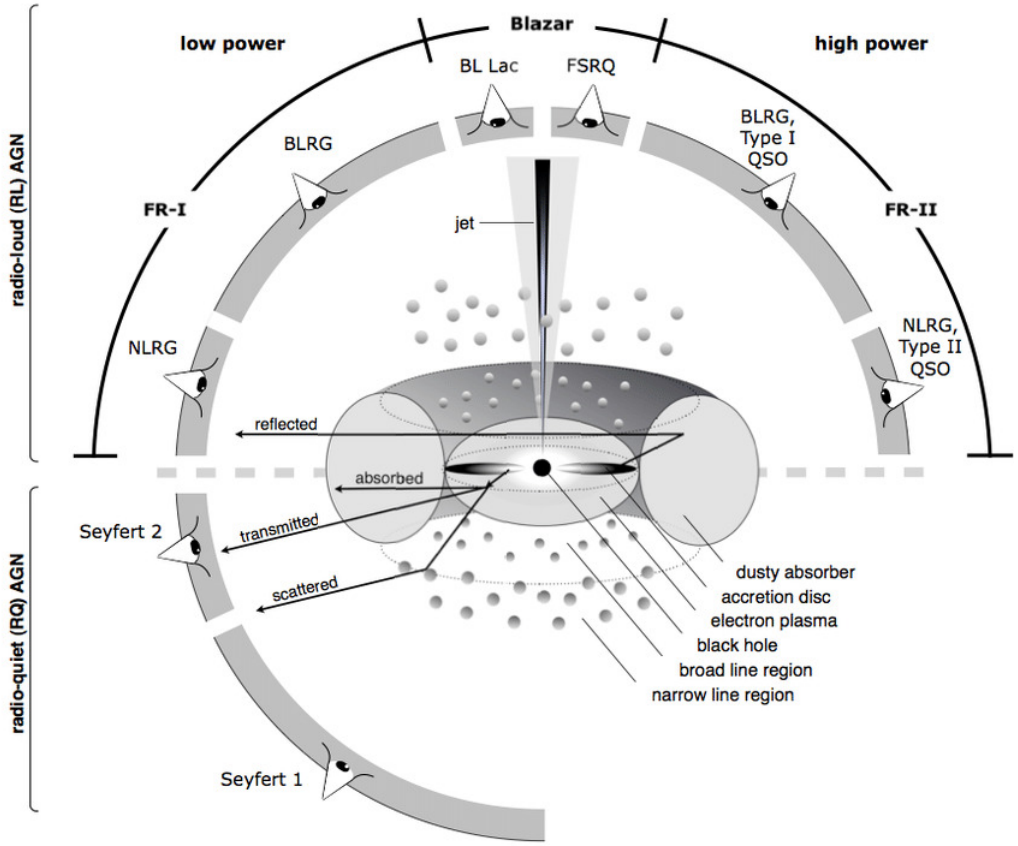

Figure 7: The unified model of Active Galactic Nuclei (AGN) (Taken from [4])

1.5 Neutrino emission from AGN

Neutrinos are elementary particles with spin of $1/2$, and they interact only via weak interaction and gravity. Neutrinos can be found in three leptonic flavours; electron (ν_e), muon (ν_μ) and tau (ν_τ), and are created by weak interactions. Their rest mass is much smaller than other fundamental particles, that it was initially believed that were massless. The first attempts to determine the mass of the neutrino have been based on the conservation of energy and momentum but results have only provided upper limits on the mass. Evidence on their mass was found by examining a quantum mechanical process known as neutrino oscillations. A neutrino oscillation means that one type of neutrino gradually transforms into another as it moves. If neutrinos do have mass, it might be expected that each type of neutrino should have a different mass and a different mass eigenstate. However, theories of neutrino mass predict that the three types of

neutrinos are well defined mixtures of several mass eigenstates. As time passes or the neutrino moves, the relative phases of the different components in this mixture change. Consequently, an initial type gradually transforms into another type of neutrino. Neutrino oscillations therefore result from the mass of the neutrino. The latest measurement of its mass is $\leq 0.8eV/c^2$ ([38]).

Neutrinos are created by various radioactive decays such as β-decay of atomic nuclei or hadrons. In astrophysical sources such as young supernova residues, binary black hole systems, and the interactions of the produced protons with targets X in the interstellar medium yield pions, which the charged ones decay into neutrinos. Neutrinos are also created in the nuclear reactions that power the core of stars, by the proton- proton chain.

AGN could be sites of which, neutrinos are produced, if the following conditions are satisfied:

- There needs to be acceleration of ions (protons/nuclei) to high energies. Acceleration mechanisms could be shock acceleration, magnetic reconnection and stochastic acceleration in plasma turbulence.
- The acceleration rate must overcome the energy loss rates (see Chapter 2).
- Existence of targets of significant density(matter and/or radiation).

TXS 0506+056

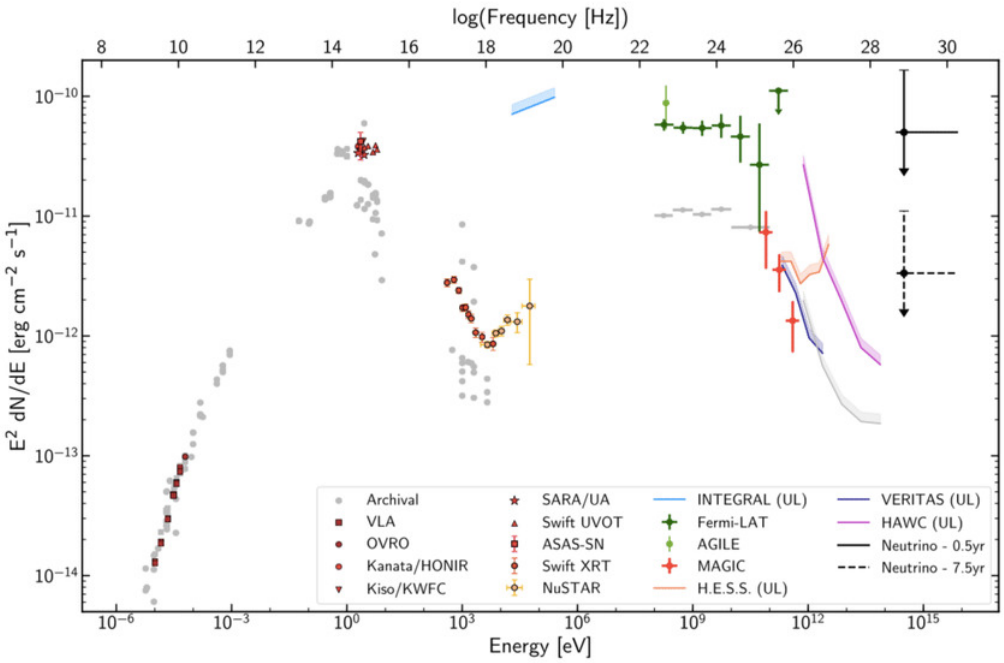

Figure 8: Spectral energy distribution for the blazar TXS 0506+056, based on observations obtained within 14 days of IceCube-170922A. Taken from [35])

In 2017, a high-energy neutrino event with energy of $E_\nu \sim 0.3$ PeV, was detected by IceCube. With the help of Fermi-LAT, its γ-ray counterpart was identified, which was the blazar, TXS 0506+0656 at $z = 0.336$. This blazar was also observed as a flaring blazar ([1]) by NuSTAR ($3-79$keV), MAGIC (50GeV-30TeV) and other radio facilities. In the subsequent analysis, the IceCube Collaboration searched for neutrino emission in the archival data of TXS 0506+056, and they found a $\sim 3.5\sigma$ excess, corresponding to 13 ± 5 excess events, in the $2014-2015$ period. However, any flaring activity was not found in both X-ray and γ-ray data, so the 2014-2015 flare is regarded as an orphan neutrino flare. Thanks to dedicated observational campaigns in 2017, the multiwavelength SED of TXS 0506+056 at this epoch were measured quite well, which are shown in Fig.8.

1.6 Motivation of thesis

Most models for blazar emission, like TXS 0506+056 ([14],[67]), are phenomenological with many free parameters. In fact, models that include hadrons make the parameter space even larger, where these parameters are related with the emitting region (Doppler factor (δ), magnetic field (B) and its radius (R)) and the primary population of particles (indices of power-law , minimum and maximum Lorentz factors and their normalization, regarding both particle species). The goal of these models is to maximize the neutrino output of a given source.

Here, we follow a different approach. Inspired by Rueda-Becerril et al. (2020) [65] we construct a physically motivated model for the jet emission. The ingredients of our model are bulk jet quantities, such as the magnetization and the bulk Lorentz factor which are motivated by ideal MHD models for jets and are tied to the accretion rate, and that particle acceleration is thought to occur via reconnection. This mechanism leads to particle properties that are benchmarked to results of PIC simulations. Ultimately, following this approach, we reduce the heavy dependence on free parameters, since we reduce them to two, as we will show in ch.3.

2 Theoretical considerations

In this chapter, we will start by explaining the acceleration mechanism of particles which will, then, result to non-thermal signatures. Following this, we will describe the radiative processes that take place in blazars, including proton-photon interactions, which are relevant when relativistic protons are present in jets. Consequently, neutrino emission is also taken into account.

2.1 Energy dissipation and particle acceleration

In the magnetohydrodynamic (MHD) jet paradigm ([7]), the jet from a blazar object, is expected to emerge from the central engine in the form of a Poynting flux dominated flow ([80]). If the configuration of the magnetic field is appropriate, then reconnection can efficiently dissipate magnetic energy in the plasma flow.

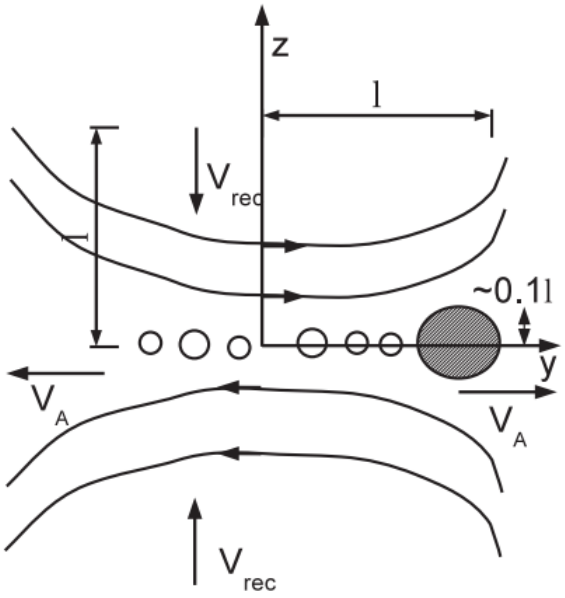

Figure 9: A sketch of the magnetic reconnection region. Magnetic field lines of opposite polarity annihilate at the x−y plane with a speed, v_{rec}. Taken from ([31])

More specifically, reconnection is a process that can occur during a topological rearrangement of the magnetic field lines (Fig.(9). So, if the field lines are of opposite polarity and are coming together, they will annihilate, liberating magnetic energy that heats the plasma and accelerates particles.

In our analysis, we focus on reconnection in the relativistic regime, meaning that the magnetic energy before the fields reconnect is greater than then particle rest mass energy. This condition can be quantified through a dimensionless parameter, known as plasma magnetization:

$$\sigma = \frac{B'}{4\pi\rho' c^2} \tag{2.1}$$

where B' and ρ' are the magnetic field and mass density of the plasma, outside the reconnecting layer, and measured in the frame of the jet fluid.

It is believed that in astrophysical sites like jets from AGN, the acceleration mechanism could be mainly attributed to shocks or magnetic reconnection. Jet observations can constrain the dissipation mechanism responsible for its emission.([75], [71]) It is found that these constraints (large radiative efficiency, production of non-thermal particle distribution and equipartition of energy density between radiating electrons and magnetic field) are satisfied when the magnetization is in the range of $\sigma \approx 0.01 - 0.1$, and even then, shocks should be subluminal for Fermi acceleration to be efficient. On the other hand, in cases where the jet is magnetically dominated $\sigma \geq 1$, relativistic reconnection is a process that can explain the observations, as numerous simulations have shown ([32],[81],[3],[81],[49]).

2.1.1 Steady reconnection models: Sweet-Parker & Petschek

Getting into a more detailed view of magnetic reconnection, whenever magnetic field lines of opposite polarity come together, Maxwell's equations imply the formation of a current sheet between them. In this layer, field lines can diffuse across the plasma to reconnect to one or more X-shaped lines. During this process, if we assume that the plasma that approaches this region has an inflow velocity, v_{in} (known as reconnection velocity), then after it passes the X-line, it will obtain outflow velocity, symbolized as v_{out}, which will be close to the Alfvén velocity $v_A = c\sqrt{\frac{\sigma}{1+\sigma}}$, that will be about $\approx c$ for high σ. From these quantities, one can also define the dimensionless reconnection rate:

$$r_{rec} = \frac{v_{in}}{v_{out}} \tag{2.2}$$

Outside the current sheet, non-ideal effects are negligible and one can use the Ohm's law, which leads to:

$$\mathbf{E} + \frac{1}{c}\langle \mathbf{v} \rangle \times \mathbf{B} = 0 \tag{2.3}$$

where $\mathbf{E}$ is the electric field and $\langle \mathbf{v} \rangle$ is the mean particle velocity. In a steady state configuration, one can calculate the electric field in the reconnection region by:

$$\mathbf{E} = -\frac{1}{c}\mathbf{v_{in}} \times \mathbf{B_o} \tag{2.4}$$

where $\mathbf{B_o}$ is the reversing magnetic field outside the current sheet.

If we define the thickness and the length of the current sheet by δ and L, respectively, then from the conservation of mass one can find:

$$\frac{\delta}{L} = r_{rec} = \frac{v_{in}}{v_{out}} \tag{2.5}$$

The most widely known and used model for magnetic reconnection is the Sweet-Parker (SP) model ([57],[76]). In the SP model, L is taken to be the macroscopic length of the magnetic field, while δ is the width of the layer which is determined by the dissipation rate and can be sustained by the resistivity. The degree of importance, regarding the resistivity, can be

determined by the Lundquist number: $S \equiv \frac{Lv_a}{\eta}$, where η is the magnetic diffusivity, produced by resistivity. For SP resistive reconnection, the rate is:

$$r_{rec} = \frac{\delta}{L} \approx \frac{1}{\sqrt{S}} \tag{2.6}$$

But, since S is a very large number in astrophysical plasmas ($S \approx 10^8$ in solar flares), SP reconnection is extremely slow, which means that the magnetic energy is released to the plasma on greater timescales than needed to explain certain transient/explosive phenomena. Since resistivity is too small in this case, kinetic effects, due to individual particle motion, are likely to be more important. Plasma oscillation frequency corresponds to these motions and is given by:

$$\omega_p = \sqrt{\frac{4\pi n q^2}{m}} \tag{2.7}$$

where n is the plasma number density, m is the mass of plasma and q is its charge. The characteristic length that these effects take place is known as skin depth and can be calculated by $\frac{c}{\omega_p}$, which is small compared to L, in astrophysical systems.

The most basic model to resolve the problem of slow reconnection in the SP case, was suggested by Petschek ([62]). His model requires the presence of two waves (slow mode shock) around a central X-point that they effectively limit the length of the reconnection region. Specifically, the L length in this analysis is determined by the ratio of inflow to outflow velocities. For greater values of inflow velocity, L can become comparable with δ, leading to greater reconnection rates (Eq. 2.6), compared to SP model. However, Petschek's model is not favourable, since there has not been a study that managed to simulate it numerically.

Tearing instability

A lot of studies ([68],[5],[46]) have investigated the effects of instabilities in the current layer in the case of fast reconnection. An important finding is the rise of the tearing instability, which is responsible for the production of magnetic islands after the break of the sheet into X-points, which lowers the ratio $\frac{L}{\delta}$ and leads to fast reconnection rates.

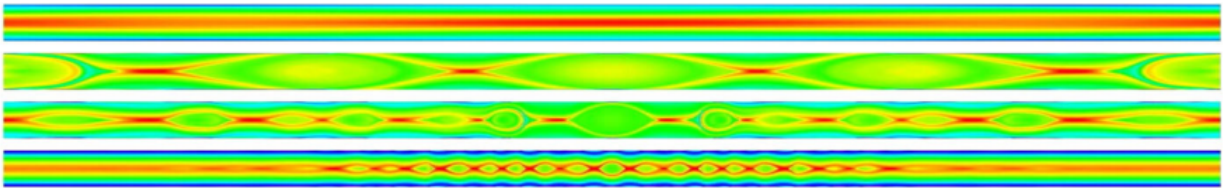

Figure 10: Contour plots of the current density showing the structure of an SP current sheet for $S = 10^4$, $S = 10^5$, $S = 10^6$ and $S = 10^7$, from top to bottom. Adapted from [68]

Specifically, in the case where the S number exceeds the value of $\sim 10^4$, numerical studies have observed the plasmoid formation due to the tearing instability. In Fig.(10), we show the spatial structure of the plasmoid chain for different S values, as calculated numerically by Loureiro et al.(2009). It is shown that the number of plasmoids observed is increased with S number, and actually in the same work is found that plasmoid number scales with S as $\sim S^{\frac{3}{8}}$.

2.2 Simulations

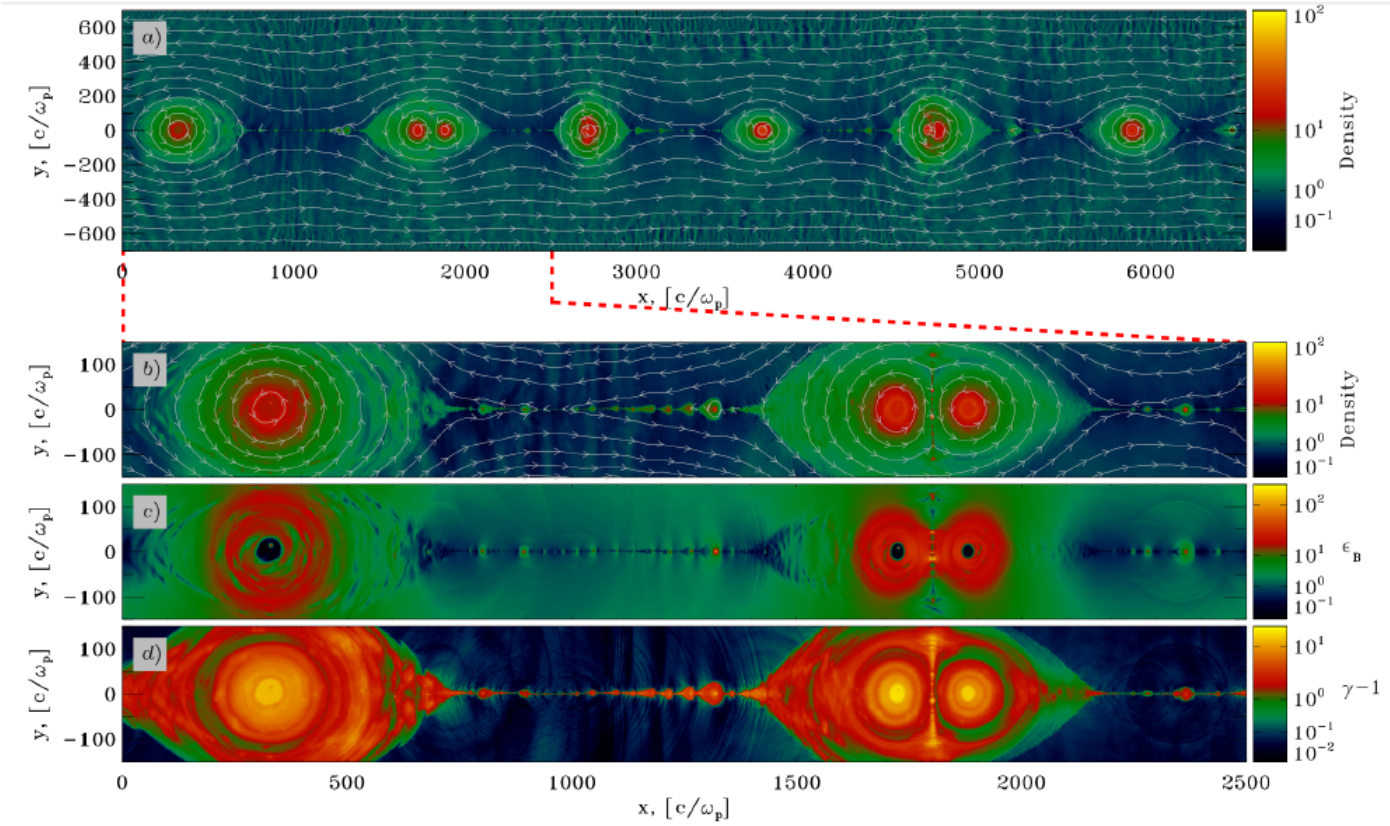

Figure 11: Structure of the reconnection layer at $\omega_p t = 3000$ from a 2D simulation of $\sigma = 10$ reconnection, regarding pair plasmas. There are presented (a) particle density, in units of the density far from the sheet (with overplotted magnetic field lines) , (b) same as (a) but in a zoomed region that contains two primary plasmoids (c) magnetic energy fraction $\epsilon_B = \frac{B^2}{8\pi mnc^2}$ and (d) mean kinetic energy per particle. Taken from [73]

The most common and widely used method to study the flow dynamics in reconnection from first principles is the kinetic particle-in-cell (PIC) simulations. There have been performed numerous studies, both in two-dimensions (2D) and three-dimensions (3D) ([74],[32],[81],[3], [81],[49],[16],[72]) involving pair plasmas or ion-electron plasmas.

PIC codes can model astrophysical plasmas as a collection of charged macro-particles that are moved by integration of the Lorentz force. Currents associated with the macroparticles are deposited on a grid where the Maxwell's equations are taking effect, which advances the appearance of electromagnetic fields. Finally, the fields are extrapolated to the location of the particles in order the Lorentz force to be computed, there. PIC simulations need to be performed in a large domain, compared to the microscopic plasma scales and in a timescale much smaller than the one corresponding to plasma oscillations ($\omega_p{}^{-1}$).

Moving on, we will describe the results of the PIC study by Sironi & Spitkovsky (2015) (hereafter SS15), in order to explain the resulting non-thermal particle distribution, that is going to be used in our work.

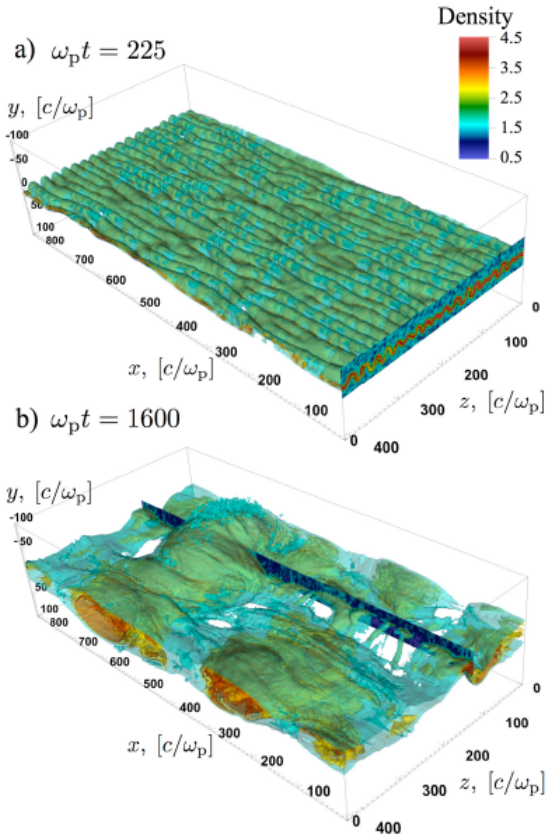

Figure 12: Structure of particle density at (a) $\omega_p t = 250$ and (b)$\omega_p t = 1600$, from a 3D simulation of $\sigma = 10$ reconnection without guide field. The 2D slices in the top and bottom panels (at $x = 820c/\omega_p$ and $z = 130c/\omega_p$, respectively) show the particle density. Taken from [73]

Initially, as found in most of PIC studies, Harris current sheet ([33]) is used as the starting equilibrium that is generally characterized by a magnetic field profile, like:

$$\mathbf{B} = B_0 \tanh \frac{2\pi y}{\delta}\hat{\mathbf{x}} + \kappa B_0 \hat{\mathbf{z}} \tag{2.8}$$

where δ is in the order of $\sim \frac{c}{\omega_p}$ ($20\frac{c}{\omega_p}$ in SS15) and the quantity κ ($\kappa = 0$ in SS15) sets the strength of a uniform guide field (perpendicular to the reconnection plane). From this expression of the magnetic field, we see that in $y = 0$ the field lines will be reversed.

Additionally, the particles, within the current sheet, have thermal distribution whose pressure balances the magnetic pressure outside the current sheet, in order to satisfy the pressure equilibrium.

The results of SS15, regarding the structure of the reconnection layer, in 2D simulations, are shown in Fig.(11). It is observed that the reconnection layer will break in a series of magnetic islands, separated by thin X-lines. Additionally, in the lower panels of Fig.(11), one can observe further fragmentation into smaller islands, as a result of secondary tearing mode ([79]). These sites are overdense, filled with hot particles and confined by strong fields. On the other hand, primary islands have cores with negligible magnetic content and are supported by the pressure of the hot particles, initially present in the current sheet. The field strength peaks in a ring surrounding the hot core. Both primary and secondary islands are moving along the layer,

pushed by the pressure of the reconnection outflow, and become larger as they coalesce with their neighboring ones.

3D simulations (12) yield similar results with 2D ones, at late times. In early phases, the reconnection layer is influenced by the drift-kink instability (DKI). DKI is a long-wavelength electromagnetic mode, which is driven by the fast drifting plasma in a thin current sheet and it quickly grows in relativistic pair plasmas, in which the mass ratio is unity. In Fig.(12), DKI forced the current sheet to form folds in the z direction. However, as we mentioned, at later times the tearing instability is dominant again. Further studies ([82],[15]) of the DK mode did not capture the late time evolution on the reconnection layer, that leads to particle acceleration, since DKI decays.

Non-thermal particle distribution

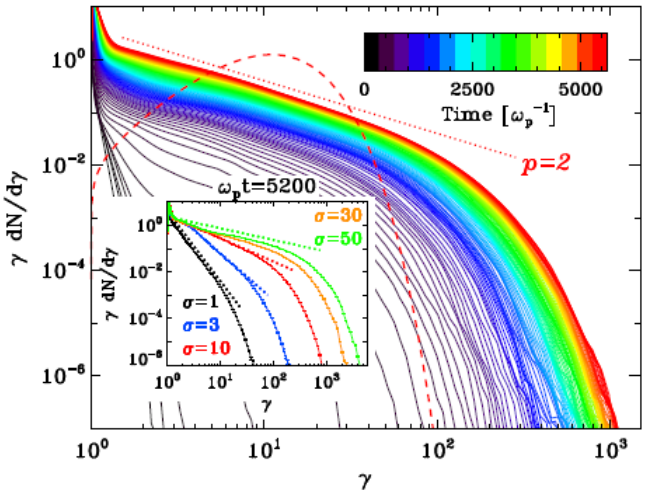

Figure 13: Temporal evolution of particle energy spectrum, from a 2D simulation of $\sigma = 10$ reconnection, regarding pair plasmas. The spectrum at late times resembles a power-law with slope $p = 2$ (dotted red line), and it clearly departs from a Maxwellian with mean energy $(\sigma + 1)mc^2$ (dashed red line, assuming complete field dissipation). In the inset, dependence of the spectrum on the magnetization, as indicated in the legend. The dotted lines refer to power-law slopes of -4,-3, -2 and -1.5 (from black to green). Taken from [73]

A product of relativistic reconnection is the generation of a broad non-thermal spectrum, extending to ultra-relativistic energies, as shown in Fig.(13). We see that for $\sigma = 10$, the spectrum (for $\gamma \geq 1.5$) can be fitted with a power-law of slope $p = -\frac{dlogN}{dlog\gamma} \sim 2$. This power law shape is established as the particles get accelerated in the X points by the reconnecting electric field. It is also observed that the power law slope depends on the flow magnetization, getting increasingly harder for higher σ. These results hold for later times of the simulation, since at early times, can be seen that the spectrum is quasi-thermal.

In other, most recent, studies [3],[32],[81],[61]), the production of high energy non-thermal particles for ion-electron plasmas was examined. More specifically, in the work of Guo et. al. (2016), simulations for magnetization in the range of $\sim 1 - 100$ showed that the reconnection

quickly establishes (within $2-3$ light crossing times) power-law energy distributions for both particle species, with slopes in the range of $1-2$. Furthermore, these results showed that the ion energy gain is comparable with the electron energy gain. Comparing the spectra between the two particle species, the slopes are identical.

Another study (Petropoulou et al. 2019 [61]) examined the case of magnetic reconnection in pair-proton plasmas, performing 2D simulations, for magnetizations in the range of $\sim 1-10$ and pair multiplicities, κ, (lepton-to-proton number ratio) in the range of $1-199$. They found that the pair energy distribution in the reconnection region can be modeled with a power-law of slope p, which is mainly controlled by magnetization (harder power-law for higher σ). Pair multiplicity also plays a role in determining the slope, as the power-law gets steeper as κ decreases (from a few to unity). Regarding protons, a late time appearance of the power-law was found, which is explained by the structure of the reconnection layer. Particularly, X-points are typically smaller than the proton Larmor radius, so acceleration by the reconnecting electric field is not very efficient. As a result, efficient acceleration occurs when protons reach a big structure in the layer. The power-law is well-shaped only in cases of low pair multiplicity ($\kappa \leq 19$).

Similar scaling of the slope with magnetization, as presented in these works, is also found in Ball et al. (2018), for cases of low ratio of proton thermal pressure to magnetic pressure.

2.3 Non-thermal radiative processes

For the remaining part of this section, we will focus on the radiative processes that take place in blazar jets, providing fundamental information on each mechanism examined.

2.3.1 Synchrotron radiation

Synchrotron radiation is one of the most well known and studied mechanisms of non-thermal emission in astrophysics. It is produced by relativistically moving, charged particles, when they move in the presence of a magnetic field.

Generally, a Lorentz force will be acted upon the charged particle. In the absence of electric field , the particle will follow a spiral trajectory, with orbital radius known as Larmor radius, defined as:

$$r_L = \frac{p_\perp c}{qB} \approx \frac{E}{qB} \tag{2.9}$$

for a relativistic particle moving perpendicular to B, where E, q, B are the energy of the particle, its charge and the magnetic field strength, respectively.

The frequency of its rotation is $\omega_B = \frac{qB}{\gamma m_i c}$, where γ is the Lorentz factor of the particle and m_i, its mass.

However, the typical frequency of synchrotron radiation does not correspond to $\nu_B =$

$\omega_B/(2\pi)$. The reason for this is that the relativistic motion of particles changes the emission profile in the observer's frame. Specifically, the emission is focused on a cone of opening angle $\theta = 2/\gamma$. Considering that radiation will be emitted in the observer's direction for a very short time window, and the Doppler effect, as well, we are led to a frequency boosted by a factor γ^3:

$$\nu_s = \gamma^3 \nu_B \tag{2.10}$$

The total power emitted by an accelerated charged particle is known as the Larmor formula:

$$P = \frac{2q^2}{3c^3}\gamma^4({a_\perp}^2 + \gamma^2 {a_\parallel}^2) \tag{2.11}$$

where $a_\perp$ and $a_\parallel$ are the perpendicular and parallel components of acceleration to the velocity vector.

If we make the assumption that the acceleration is perpendicular to velocity, with magnitute $a_\perp = \omega_B u_\perp$, then eq.(2.11) becomes:

$$P = \frac{2q^4}{3{m_i}^2 c^3} B^2 \gamma^2 \beta^2 \sin^2 a \tag{2.12}$$

where a is the angle that is formed by the magnetic field and the particle velocity vector (pitch angle) and $\beta = \frac{v}{c}$.

For an isotropic distribution of particles, one can calculate the factor $\sin^2 a$, averaged over all pitch angles:

$$\left\langle \sin^2 \alpha \right\rangle = \frac{\int \sin^2 \alpha d\Omega}{\int d\Omega} = \frac{2}{3} \tag{2.13}$$

We can write eq.(2.12), in terms of Thomson cross section which in the case where particles are electrons, is written as:

$$\sigma_{T,e} = \frac{8\pi}{3}\left(\frac{e^2}{m_e c^2}\right)^2 \tag{2.14}$$

For a particle of charge $q = Ze$ and mass m_i, the Thomson cross section reads:

$$\sigma_{T,i} = \sigma_{T,e} Z^4 \mu^2 \tag{2.15}$$

where $\mu = \frac{m_e}{m_i}$. Then, eq.(2.12) is written as:

$$P = \frac{4}{3}\sigma_{T,i} c U_B Z^4 \mu^2 \gamma^2 \beta^2 \tag{2.16}$$

where $U_B = \frac{B^2}{8\pi}$ is the the magnetic field energy density. In the case of relativistic particles ($\gamma \gg 1$), the factor (β^2) is close to unity and can be neglected.

Furthermore, since the particles that are going to be investigated in our work are protons and electrons, one can compute the ratio of total synchrotron power emitted by particles with the same γ:

$$\frac{P_e}{P_p} = \left(\frac{m_p}{m_e}\right)^2 \sim 10^6 \tag{2.17}$$

In this case, synchrotron emission is far more prominent when powered by electrons, so from now on, we will assume electrons as the main particles for our calculations.

Furthermore, there is a quantity that reveals the time that needs to pass for a particle to lose half of its initial energy by emitting synchrotron photons. This quantity is known as cooling timescale:

$$t_{syn} = \frac{E}{P_{tot}} = \frac{6\pi c m_e}{\sigma_{T,e} Z^4 \mu^3 B^2 \gamma} \tag{2.18}$$

For an electron-positron plasma, the ratio of timescales between these particles will be:

$$\frac{t_{syn,p}}{t_{syn,e}} = \left(\frac{m_p}{m_e}\right)^3 \simeq 10^9 sec \tag{2.19}$$

This result shows again why protons are less efficient synchrotron emitters than electrons, regarding synchrotron emission.

Advanced calculations of synchrotron radiation, regarding the emission from a single particle (or a population of same Z, μ, γ particles), lead to the equation for the synchrotron emissivity in units of $[\frac{erg}{sHz}]$:

$$j_s(\nu) = \frac{\sqrt{3} q^3 B \sin\alpha}{m_e c^2} F\left(\frac{\nu}{\nu_c}\right) \tag{2.20}$$

where ν_c is the so-called critical frequency and is given by $\nu_c = \frac{3}{2}\nu_s \sin a$.

Function $F(x)$ (see Fig.14) is defined as $F(x) = x\int_x^\infty K_{5/3}(\xi)d\xi$, where $K_{5/3}$ is the modified Bessel equation of the second kind and of order $5/3$.

The behaviour of function $F(x)$ can be approximately calculated in an easier manner by its asymptotic forms:

$$F(x) = \begin{cases} \frac{4\pi}{\sqrt{3}\Gamma(1/3)2^{1/3}} x^{1/3} & , x \ll 1 \\ \frac{\pi}{2}^{1/2} x^{1/2} exp(-x) & , x \gg 1 \end{cases} \tag{2.21}$$

Realistically, when we examine the emission from an astrophysical object, we expect the radiating particles to have a distribution of energies (or Lorentz factors).The most commonly used distribution is the power law, with low and high energy cutoffs, namely:

$$n(\gamma)d\gamma = n_o \gamma^{-p} d\gamma \quad for \quad \gamma_{\text{min}} \leq \gamma \leq \gamma_{\text{max}} \qquad [cm^{-3}] \tag{2.22}$$

In order to calculate the emission in this case, we need to take into account the emission coming from every part of the particle distribution. This can be done by performing the following integration:

$$I_{syn(\nu)} = \int_{\gamma_{\text{min}}}^{\gamma_{\text{max}}} d\gamma\, Q(\gamma) j_s(\nu) \tag{2.23}$$

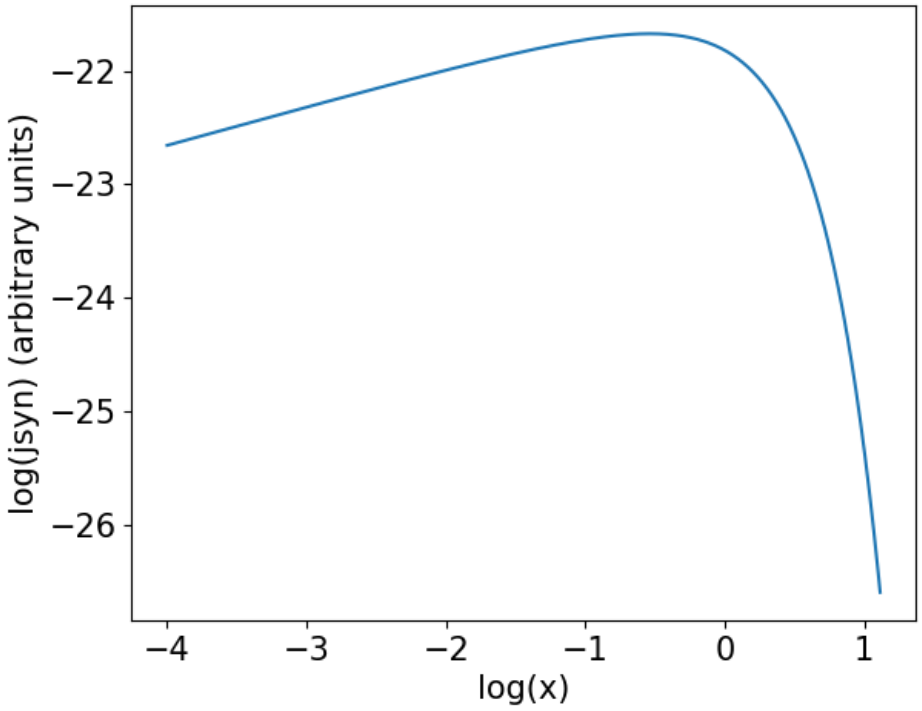

Figure 14: Recreation of synchrotron spectrum, produced by electrons of same energy, using the definition of function $F(x)$ where $x = \frac{\nu}{\nu_c}$ and $\nu_c = \frac{3}{2} \sin \alpha \nu_s$

Calculating eq.(2.23), one can obtain the following result (which is also displayed in Fig.15)[2]

$$I_{syn(\nu)} \propto B^{\frac{p+1}{2}} \nu^{-\frac{p-1}{2}}, \quad \nu_{\text{min}} \leq \nu \leq \nu_{\text{max}} \tag{2.25}$$

2.3.2 Synchrotron Self-Absorption

Synchrotron emission is accompanied by absorption in which a photon is absorbed by an electron in the presence of a magnetic field. This process is called synchrotron self-absorption (SSA).

For a power-law distribution of particles (eq.(2.20), the absorption coefficient is shown to

[2]The detailed version of this calculation can be found in Blumenthal & Gould (1970) [9]:

$$I_{syn}(\nu) = \frac{4\pi k e^3 B^{(p+1)/2}}{mc^2} \left(\frac{3e}{4\pi mc} \right)^{(p-1)/2} a(p) \nu^{-(p-1)/2} \tag{2.24}$$

where

$$a(p) = \frac{2^{(p-1)/2} \sqrt{3} \Gamma[(3p-1)/12] \Gamma[(3p+19)/12] \Gamma[(p+5)/4]}{8\pi^{1/2}(p+1)\Gamma[(p+7)/4]}$$

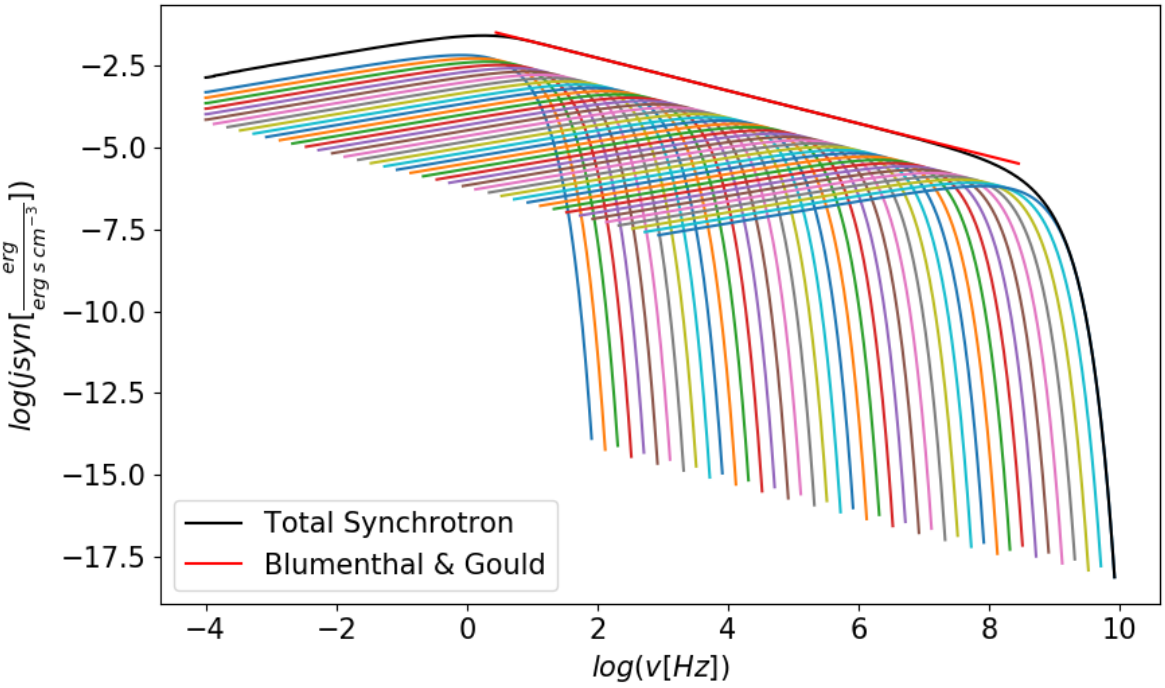

Figure 15: Synchrotron emission from a power-law distribution of electrons with slope $p = 2$, minimum and maximum Lorentz factors $\gamma_{\text{min}} = 1$ and $\gamma_{\text{max}} = 10^4$, respectively, and assuming magnetic field strength of $B = 1\mu G$. Each color line represents the emission produced by electrons of a specific Lorentz factor. The sum of the resulting emission is compared with the analytical expression of Blumenthal & Gould [9].

be [3]:

$$\alpha_\nu = \frac{\sqrt{3}q^3}{8\pi m}\left(\frac{3q}{2\pi m^3 c^5}\right)^{p/2} Q_o (B\sin\alpha)^{(p+2)/2}\Gamma\left(\frac{3p+2}{12}\right)\Gamma\left(\frac{3p+22}{12}\right)\nu^{-(p+4)/2} \tag{2.26}$$

There is a specific value of frequency, known as ν_{SSA}, that for lower frequencies, one can see the contribution of the SSA process in the spectral energy distribution (SED) diagram. In fact, if the optical depth of the source, defined as $\tau_\nu = \int a_\nu dr$, is greater than unity (optically thick), then the emission will be absorbed, in these frequencies, to some degree. On the other hand, if the source is optically thin ($\tau_\nu \ll 1$) in other frequency bands, then the radiation can escape from the source without being absorbed. So, ν_{SSA}, actually, signals the frequency where the source is getting optically thin from optically thick ($\tau_{\nu_{SSA}} = 1$).

Finally, from the emission coefficient (eq.(2.18) and the absorption coefficient (eq.(2.26), one can calculate the source function: $S_\nu = \frac{j_\nu}{a_\nu}$. If the source is optically thick, then the emission can be approximated by the source function, giving the following result:

$$J_\nu = S_\nu \propto \nu^{\frac{5}{2}} \tag{2.27}$$

[3] Rybicki & Lightman (1985) Chapter 6.8 [66]

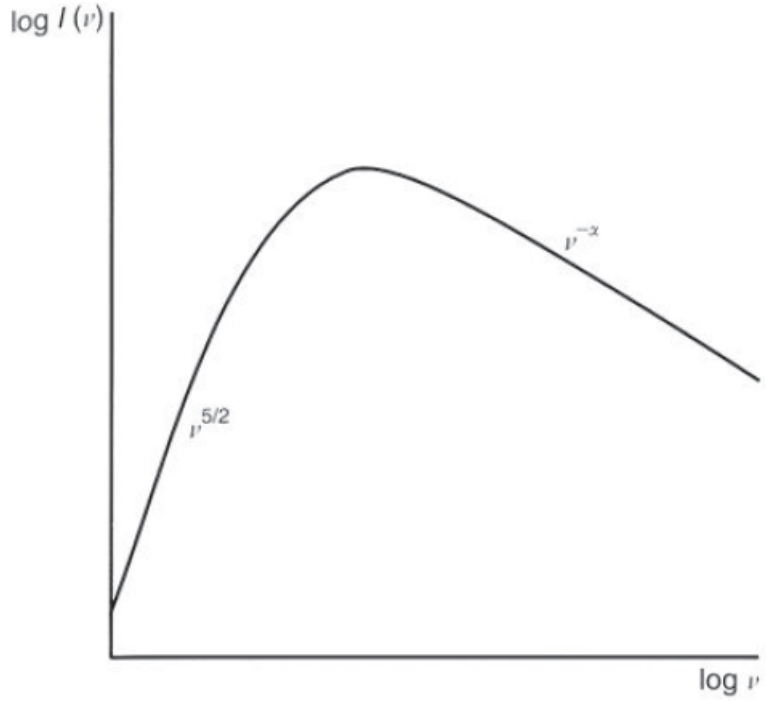

Figure 16: The spectrum of a source of synchrotron radiation which exhibits the phenomenon of synchrotron self-absorption. Adapted from [45]

So, that means that the component of SSA emission from a source, will not have any dependence from the slope of the particle energy distribution (Fig.(16)).

2.3.3 Inverse Compton scattering (ICS)

Inverse Compton scattering (ICS) is a high-energy photon production process; low energy photon are being scattered by high energy electrons. The term ”inverse” is used because during this process, charged particles are losing energy, as they transfer it to photons, which is the inverse exchange of regular Compton scattering.

We can start by naming S our laboratory frame and S’, the frame of the electron (Fig.17). Using Lorentz transformations one may write the equations that relate the photon energies in S and S’:

$$\epsilon' = \gamma\epsilon(1 - \beta\cos\theta) \tag{2.28}$$

$$\epsilon = \gamma\epsilon'(1 + \beta\cos\theta') \tag{2.29}$$

where the primes are used for quantities measured in S’ and θ is the angle that is formed by the electron-photon directions.

The ICS process can occur in the Thomson or Klein-Nishina (K-N) regime. The condition that determines the transition between the two regimes is the value of photon energy as seen in the electron rest frame. If its value is lower than $m_e c^2$, then we can make calculations in

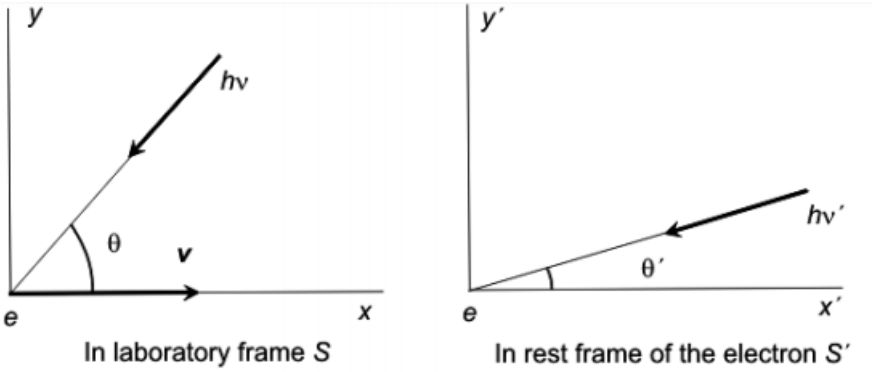

Figure 17: Geometry of ICS in S and S' frames. [45])

the Thomson limit, but if the opposite is the case, then one should make the corrections that demands the K-N regime. The difference bewtween the two, is that in the K-N limit, particles lose almost all their energy in one scattering, whereas in the Thomson limit interactions are roughly elastic. However, in the K-N limit scatterings rarely occur, due to the rapid decrease of the cross section. In the following, we will focus on the Thomson limit case.

In this regime, the photon energy remains the same after the scattering in the electron frame. In the laboratory frame, calculations lead to the following equation, regarding the energy of scattered photons:

$$\epsilon_1 = \epsilon \frac{1 - \beta \cos\theta}{1 - \beta \cos\theta_1} \tag{2.30}$$

where the subscript "1" denotes the quantities after the scattering.

From eq.(2.30), one can calculate the maximum energy that photons can take (setting $\theta = \pi$ and $\theta_1 = 0$):

$$\epsilon_{1,\text{max}} = 4\gamma^2 \epsilon \tag{2.31}$$

The emission from ICS can be calculated in the same manner as described in the case of synchrotron radiation. The single-particle emissivity can be found by Blumenthal & Gould (1970):

$$j_{ics}\left(\epsilon_1\right) = \int \frac{3\sigma_T c}{16\gamma^4} \frac{n(\epsilon)}{\epsilon^2} \nu_1 \left[2\epsilon_1 \ln\left(\frac{\epsilon_1}{4\gamma^2\epsilon}\right) + \epsilon_1 + 4\gamma^2\nu - \frac{\epsilon_1^2}{2\gamma^2\epsilon} \right] d\epsilon \tag{2.32}$$

where $n(\epsilon)$ stands for the differential number density of the radiation field in units $[\text{erg}^{-1}\text{cm}^{-3}]$.

Assuming again, a power law energy distribution for particles, (eq.(2.20), we perform the same kind of calculations, as we did in the synchrotron case:

$$I_{ics}(\epsilon) = \int_{\gamma_{\text{min}}}^{\gamma_{\text{max}}} d\gamma Q(\gamma) j_{ics}(\epsilon) \tag{2.33}$$

This will result (Fig. 18) to[4]

$$I_{ics}(\epsilon) \propto {\epsilon_1}^{-\frac{p-1}{2}} \quad \text{for } \epsilon_{1,\text{min}}\epsilon\nu_1 \leq \epsilon_{1,\text{max}} \tag{2.35}$$

[4]Assuming that $n(\epsilon)$ is the differential number density of blackbody radiation, Blumenthal and Gould provide

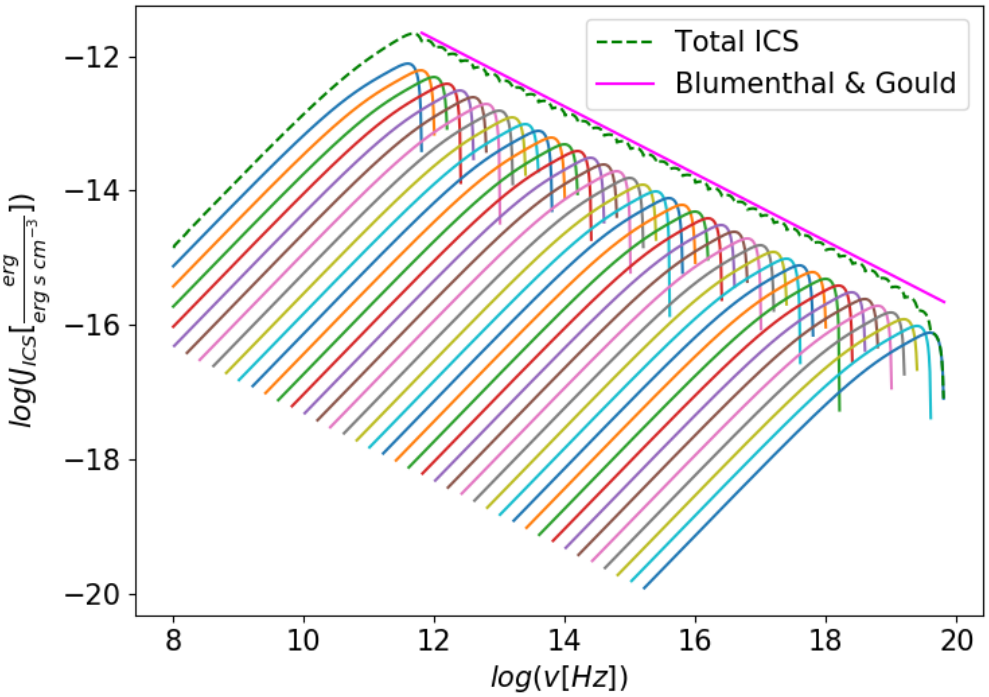

Figure 18: ICS emission from a power-law distribution of electrons of slope $p = 2$, minimum and maximum Lorentz factors $\gamma_{\text{min}} = 1$ and $\gamma_{\text{max}} = 10^4$, respectively, and monoenergetic seed photons with $\epsilon \approx 10^{-3}$ eV. Each color line represents the emission produced by electrons of a specific Lorentz factor. The sum of the resulting emission is compared with the analytical expression of Blumenthal & Gould.[9]

The mean energy of the scattering particles is very close to the maximum from eq.(2.31): $\langle \epsilon_1 \rangle = \frac{1}{3}\epsilon_{1,\text{max}}$. So, the limits in eq.(2.35) will be: $\nu_{1,\text{min / max}} = \frac{4}{3}{\gamma_{\text{min / max}}}^2 \nu$

The significance of the result in eq.(2.35) is obvious, since one can easily notice that this process produces a photon spectrum with the same slope with synchrotron emission.

Lastly, we mention the total emitted power and the timescale for ICS, in the Thomson regime:

$$P_{ICS} = \frac{4}{3}\sigma_T c U_\phi \gamma^2 \beta^2 \tag{2.36}$$

where $U_\phi = \int_{\epsilon_{\text{min}}}^{\frac{3\gamma\epsilon m_e * c^2}{4}} \epsilon n(\epsilon) d\epsilon$ is the energy density of the radiation field. Comparing the ratio

---

the following result:

$$I_{ics}(\epsilon) = \pi^{-1}\left(r_0^2/\hbar^3 c^2\right) Q_o (kT)^{(p+5)/2} F(p) \epsilon_1^{-(p+1)/2} \tag{2.34}$$

where the parameter F(p) is calculated as: $F(p) = 2^{p+3}\left[\left(p^2+4p+11\right)/(p+3)^2(p+1)(p+5)\right]$ $\times \Gamma\left[\frac{1}{2}(p+5)\right]\zeta\left[\frac{1}{2}(p+5)\right]$ and ζ is known as Riemann function:

$$\zeta(s) = \sum_{n=1}^{\infty} \frac{1}{n^s} = \frac{1}{\Gamma(s)} \int_0^\infty \frac{x^{s-1}}{e^x - 1}\, \text{d}x$$

of total power radiated by electrons and protons, we will be led to the same result as found for synchrotron emission (eq.(2.17). This is why ICS emission, similar to synchrotron, is thought to be originated mainly by electrons.

Consequently, the cooling timescale is calculated as:

$$t_{ICS} = \frac{6\pi m_e c}{\sigma_T U_\phi \gamma} \tag{2.37}$$

2.3.4 Synchrotron Self-Compton (SSC)

The SSC process refers to the mechanism where non-thermal electrons up-scatter their own synchrotron photons. In order to describe this process, we will make some simplifications to calculations. If we assume the synchrotron emission coefficient can be approximated by a δ-function, then we would write eq.(2.18) as:

$$j_s(\epsilon) = A\epsilon\delta(\epsilon - \epsilon_s) \tag{2.38}$$

Assuming that the particles are monoenergetic, namely:

$$Q(\gamma) = Q_o\delta(\gamma - \gamma_o) \tag{2.39}$$

Then, the emitting power per unit energy will be calculated by:

$$I_{syn}(\epsilon) = \int d\gamma Q(\gamma) j_s(\epsilon) \propto \epsilon\delta(\epsilon - b{\gamma_o}^2 m_e c^2) \tag{2.40}$$

where $b = \frac{B}{B_{cr}}$ and $B_{cr} = \frac{{m_e}^2 c^3}{eh}$

The number density of synchrotron photons will be:

$$n_{syn}(\epsilon) = \frac{1}{3}\frac{RI_{syn}(\epsilon)}{c\epsilon} = \frac{1}{3\pi}\frac{N_{\text{tot}}}{R^2}\sigma_\tau \frac{BB_{cr}}{8\pi m_e c^2}\delta\left(\epsilon - b\gamma_0 m_e c^2\right) \tag{2.41}$$

where R is the radius of the source. Next, ICS (SSC) will occur, so we need to take into account the respective emission coefficient. In the same manner, making a δ-function approximation, eq.(2.32) will be written as:

$$j_{ics}(\epsilon) = C\epsilon\delta(\epsilon - < \epsilon_{ics} >) \tag{2.42}$$

where $\langle\epsilon_{ics}\rangle$ is the mean scattered energy of synchrotron photons, so it is: $\langle\epsilon_{ics}\rangle = \frac{4}{3}{\gamma_o}^2\epsilon_s = \frac{4}{3}b{\gamma_o}^2 m_e c^2$.

Finally, this will lead to the total intensity per unit energy of the SSC emission:

$$I_{ICS}(\epsilon) = \int d\gamma Q(\gamma) j_{ICS}(\epsilon) \propto \epsilon\delta(\epsilon - b{\gamma_o}^4 m_e c^2) \tag{2.43}$$

And the number density of SSC photons will be:

$$n_{SSC} = \frac{1}{9\pi}\frac{R}{c\epsilon}\frac{N_{\text{tot}}^2}{R^5}\sigma_\tau^2 c\frac{BB_{cr}}{8\pi m_e c^2}\epsilon\delta\left(\epsilon - b\gamma_0^4 m_e c^2\right) \tag{2.44}$$

Here, we can see that these results reveal the non-linearity of SSC emission, which show the dependence of the emission from the number of particles and the radius of the source, that they determine how dominant the process can be.

2.3.5 $\gamma\gamma$ absorption

One of the most common mechanism in high energy astrophysics is the photon-photon interaction which leads to the production of an electron-positron pair: $\gamma\gamma \rightarrow e^+e^-$

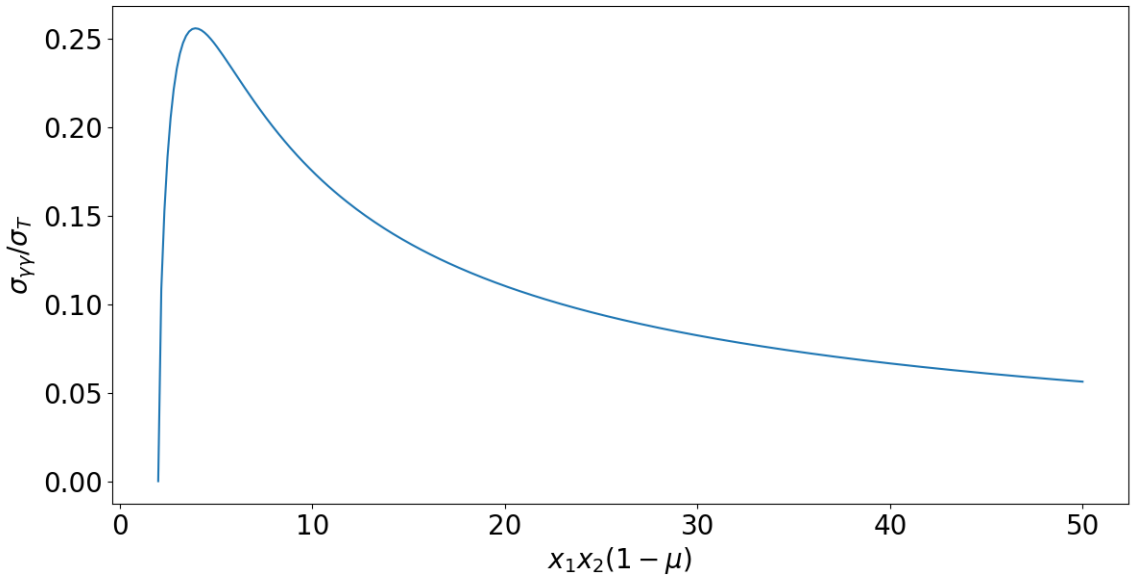

Figure 19: Cross section of $\gamma\gamma$ absorption divided by Thomson cross section, as a function of the interacting photon energies.x_1 and x_2 are the dimensionless photon energies, normalized to the electron rest mass energy.

In order for this process to take place, the following condition has to be met:

$$\epsilon_2 \geq \frac{2{m_e}^2c^4}{\epsilon_1(1-\cos\theta)} \tag{2.45}$$

where ϵ_1 and ϵ_2 are the energies of the interacting photons and θ is the angle that is formed by their velocity vectors.

In our work, γ-rays will be emitted in the very high energy regime, and we expect their absorption by lower energy photons. In order to determine, the degree of this absorption, we must examine the opacity of the source.

In this process, the cross section is symbolized as $\sigma_{\gamma\gamma}$. More specifically, the pair production cross section, $\sigma_{\gamma\gamma}$, is computed in Quantum Electrodynamics and is found to be:

$$\sigma_{\gamma\gamma}(s) = \frac{1}{2}\pi r_e^2\left(1-\beta_{\text{cm}}^2\right)\left[\left(3-\beta_{\text{cm}}^4\right)\ln\left(\frac{1+\beta_{\text{cm}}}{1-\beta_{\text{cm}}}\right) - 2\beta_{\text{cm}}\left(2-\beta_{\text{cm}}^2\right)\right] \tag{2.46}$$

where $s = \frac{\epsilon_1 \epsilon_2 (1-\mu)}{2}$, $\mu = \cos\theta$, $r_e = \frac{e^2}{m_e c^2}$ is the classical electron radius and $\beta_{cm} = (\frac{s-1}{s})^{1/2}$ is the dimensionless velocity of the center-of-momentum frame of the produced electron and positron.

Despite its complicated expression, the pair production can be well approximated by a simpler form, assuming a step function estimation:

$$\sigma_{\gamma\gamma} = \sigma_T \frac{\Theta\left[\epsilon_1 \epsilon_2 (1-\mu) - 2\right]}{\epsilon_1 \epsilon_2 (1-\mu)} \tag{2.47}$$

From Fig.(19) we can see that $\gamma\gamma$ interactions are more probable to happen near the threshold of eq.(2.45). Concluding, knowing the cross section one can compute the optical depth doing:

$$\tau_{\gamma\gamma} = \int_0^R dr \int_{\epsilon_{\min}}^{\epsilon_{\max}} n(\epsilon) d\epsilon \int \sigma_{\gamma\gamma}(s)(1 - \cos(\theta)) d\Omega \tag{2.48}$$

2.3.6 Hadronic interactions

Protons are particles with electric charge, so that means that they will be subject to the same radiation mechanisms, such as electrons. Namely, we already described how less efficient protons are, compared to electrons, in synchrotron and ICS emission. However, the hadronic nature of protons allows them to take part into additional processes such as proton-proton (p-p) and photohadronic (p-γ) interactions.

► p-p interactions

Inelastic collisions of energetic protons with ambient matter (cold protons) can result to the production of pions (and Kaons, much rarer).

The main interactions are:

1. $p + p \rightarrow p + p + \pi^0$
2. $p + p \rightarrow p + n + \pi^+$
3. $p + p \rightarrow p + p + \pi^+ + \pi^-$

Pions are produced but they decay very quickly ($\sim 10^{-8}$ sec) into lighter particles as shown below:

1. $\pi^0 \rightarrow 2\gamma$
2. $\pi^+ \rightarrow \mu^+ + \nu_\mu$ and $\mu^+ \rightarrow e^+ + \overline{\nu_\mu} + \nu_e$

3. $\pi^- \rightarrow \mu^- + \overline{\nu_\mu}$ and $\mu^- \rightarrow e^- + \nu_\mu + \overline{\nu_e}$

Contrary to the synchrotron process, hadronic interactions are basically inelastic collisions leading to the production of secondary particles. As a result, there is a minimum energy needed for the interaction to occur, known as threshold energy. The calculation of this quantity can be found in the Appendix B. Since, the incoming particles, are thought to be a high energy proton and a cold proton, we will assume that the latter will be $\sim$ at rest. This leads to:

$$\gamma_p \geqslant 1 + m_\pi^0 \left(\frac{2}{m_p} + \frac{m_{\pi^0}}{2m_p^2} \right) \tag{2.49}$$

and is estimated to be $\gamma_{p,th} \simeq 1.298$, meaning that the threshold proton energy will be about $E_{p,th} = \gamma_{p,th} m_p c^2 \simeq 1.22$ GeV.

The cross section of p-p collisions is approximated by Kelner & Aharonian (2006) (Fig.(20), in an analytical form:

$$\sigma_{inel}\left(E_p\right) = \left(34.3 + 0.88L + 0.25L^2\right) \times \left[1 - \left(\frac{E_{th}}{E_p}\right)^4\right]^2 \tag{2.50}$$

where L is defined as: $L = \ln\left(\frac{E_p}{1TeV}\right)$.

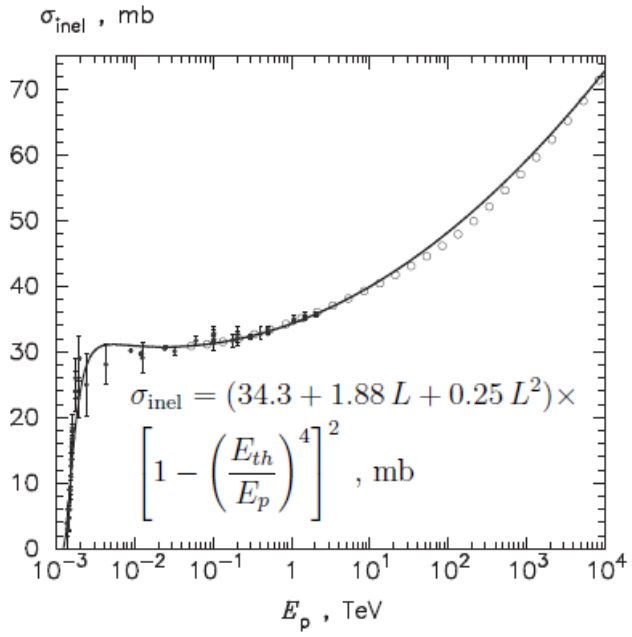

Figure 20: Inelastic cross section of p-p interactions as apprximated by Kelner & Aharonian [40]

The differential interaction rate of this process is:

$$\dot{n}\left(E_\pi, \Omega_\pi\right) = cn_2 \oint d\Omega_1 \int dE_1 n_1\left(E_1\right) \beta_1 (1 - \beta_1 \mu_1) \frac{d\sigma(E_1, \Omega_1)}{dE_\pi d\Omega_\pi} \tag{2.51}$$

where the quantities marked with the number 1 correspond to the high energy protons, while number 2 is referring to the cold protons and the letter π corresponds to the secondary particles. $\frac{d\sigma(E_1,\Omega_1)}{dE_\pi d\Omega_\pi}$ is the differential cross section, regarding the production of particles with energy E_π within solid angle Ω_π. Assuming that the high energy protons are isotropically distributed:

$$n_1(E_1,\Omega_1) = \frac{n_1(E_1)}{4\pi} \tag{2.52}$$

and defining the integrated over the solid angle, interaction rate as:

$$\dot{n}\left(E_\pi\right) \equiv \frac{dN_{sc}}{dVdtdE_\pi} = \oint d\Omega_\pi \dot{n}\left(E_\pi,\Omega_\pi\right) \tag{2.53}$$

Finally, one can make the following approximation for the differential factor of the cross section:

$$\frac{d\sigma_{pp}(E_p)}{dE_\pi} = \sigma_{pp}(E_p)\xi_\pi(E_p)\delta(E_\pi - < E_\pi >) \tag{2.54}$$

where ξ_π is the pion multiplicity, which shows the number of pions produced in an interaction, $< E_\pi >= \frac{k_{pp}}{\xi_\pi}[E_p - m_p cc]$ is the characteristic pion energy, and k_{pp} ($\simeq 0.17$) is the inelasticity.

Following the eq. (2.52),(2.53) and (2.54) we can write the differential interaction rate as:

$$\dot{n}_\pi = \frac{dN_\pi}{dtdVdE_\pi} \simeq cn_1n_2\xi_\pi\delta(E_\pi - \langle E_\pi\rangle\sigma_{pp}(E_\pi) \tag{2.55}$$

Subsequently, the proton energy loss rate can be approximated by:

$$P(E_p) = \frac{dE_p}{dt} = \frac{E_\pi\dot{n}_\pi}{n_1} \simeq E_\pi cn_2\xi_\pi\delta(E_\pi - \langle E_\pi\rangle)\sigma_{pp}(E_\pi) \tag{2.56}$$

However, the above result is valid for the production of one pion. Integrating over all pion energies, will lead to the total energy loss rate:

$$P(E_p) = \int dE_\pi P(E_\pi) \simeq cn_2k_{pp}\sigma_{pp}(E_p - m_pc^2) \quad , E_p \geq 1.22GeV \tag{2.57}$$

Using eq.(2.57), we can calculate the energy loss timescale of p-p process:

$$t_{pp} = \frac{E_p}{cn_2k_{pp}\sigma_{pp}(E_p - m_pc^2)} \approx [cn_2k_{pp}\sigma_{pp}]^{-1} \tag{2.58}$$

Knowing the timescale, we can define another quantity, the efficiency of the interaction:

$$f_{pp} = \frac{1}{1+\frac{t_{pp}}{t_{dyn}}} \tag{2.59}$$

where t_{dyn} is the dynamical time, often estimated by R/c, where R is the radius of the source.

Efficiency is a quantity that indicates how many protons lost their energy to produce secondary particles, before they leave the system. If $f_{pp} \to 1$, then the source we examine, will be efficient regarding p-p collisions.

► **Photopion process**

Photopion (or photomeson) production is one of the fundamental photohadronic processes: $p + \gamma \rightarrow N + \pi^{\pm/o}$

The charged or neutral pions that will be produced will then decay, in the same way as described in p-p collisions.

We can compute the energy threshold for this process (see Appendix B), which will lead to the following result:

$$\epsilon_r \geq c^2 \left(m_{\pi^o} + \frac{{m_{\pi^o}}^2}{2m_p} \right) \simeq 145\,\mathrm{MeV} \tag{2.60}$$

where $\epsilon_r = \epsilon\gamma_p(1 - \beta_p\mu)$ and is the interaction energy, meaning the energy of a photon as seen in the rest frame of the proton. If we assume that the interaction is head-on ($\mu = -1$), then the threshold condition reads:

$$2\gamma_p\epsilon \geq 145MeV \tag{2.61}$$

This means that an appropriate combination of energies of protons and target photons is needed, for them to interact.

Moving on to the interaction rate of the process, in the case of ultrarelativistic protons in a radiation field $n_{ph}(\epsilon, \Omega)$, it would be:

$$\dot{N}_{\mathrm{sc}}\left(\gamma_p\right) = c \oint d\Omega \int_0^\infty d\epsilon \left(1 - \beta_p\mu\right) n_{\mathrm{ph}}(\epsilon, \Omega)\sigma_{\gamma p}\left(\epsilon_r\right) \tag{2.62}$$

In an inelastic collision, the high energy proton loses a fraction $K(\epsilon_r)$ of its initial energy, known as the inelasticity. The timescale ($t = [dotN_{\mathrm{sc}}]^{-1}$) of this process, in the case of an isotropic radiation field could also be calculated by:

$$t_{\mathrm{p}\pi}^{-1}\left(\gamma_{\mathrm{p}}\right) = \frac{c}{2\gamma_{\mathrm{p}}^2} \int_{\bar{\epsilon}_{\mathrm{th}}}^\infty d\bar{\epsilon}\sigma_{p\pi}(\bar{\epsilon})\kappa_{\mathrm{p}}(\bar{\epsilon})\bar{\epsilon} \int_{\bar{\epsilon}/2\gamma_{\mathrm{p}}}^\infty d\epsilon' \frac{n\left(\epsilon'\right)}{\epsilon'^2} \tag{2.63}$$

In order to make specific calculation for eq.(2.63), we need to describe the photopion cross section first. The cross section depends only on the invariant energy of the interaction, ϵ_r and it contains several contributions, but it can be approximated by the sum of two main channels. One where the main contribution comes from $\Delta^+(1232)$ resonance, where only neutral pions are produced (single pion channel), and one where the initial proton energy is roughly equally divided into $\pi^o, \pi^\pm$ particles (multipion channel).

A common estimation for the photopion cross section is the two-step approximation, given by:

$$\sigma_{p\pi}\left(\epsilon_r\right) = \begin{cases} 340\mu\mathrm{b}, & \epsilon_{\mathrm{thr}} = 390 \leq \epsilon_r \leq 980 \\ 120\mu\mathrm{b}, & \epsilon_r \leq 980 \end{cases} \tag{2.64}$$

$$K_{p\pi}\left(\epsilon_r\right) = \begin{cases} 0.2, & 390 \leq \epsilon_r \leq 980 \\ 0.6, & \epsilon_r \leq 980 \end{cases} \tag{2.65}$$

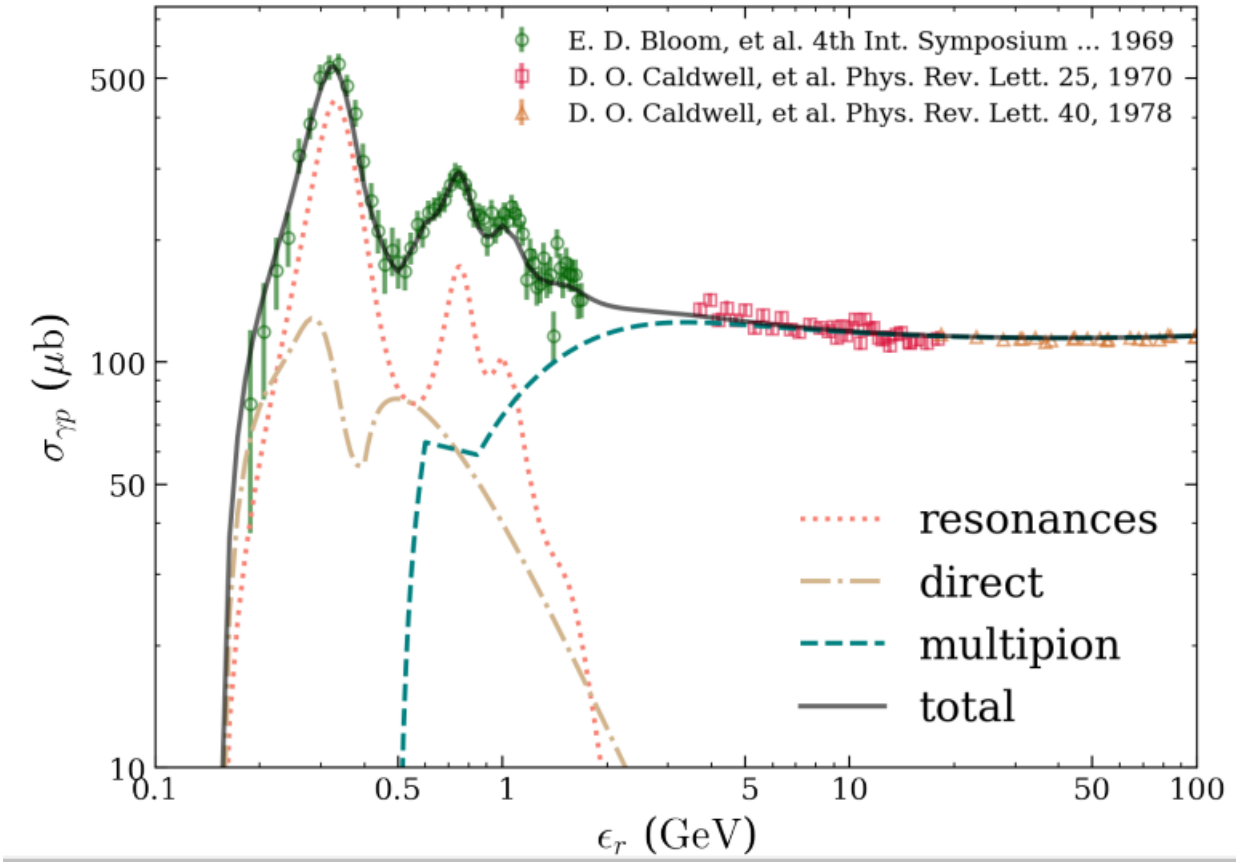

Figure 21: Cross section of photopion as a function of photon energy in the proton rest frame. The curves correspond to the theoretical estimates of different processes. The measurements of the total cross section are from D. O. Caldwell et al.(1970,1978) [12],[11] and E. D. Bloom et al.(1969) ([8]). Adapted from [50]

This approximation results to the same effective cross section for both of the limits of interaction energies: $\hat{\sigma}_{p\pi} \equiv \sigma_{p\pi}(\epsilon_r) K_{p\pi}(\epsilon_r) \equiv \sigma_0 K_0 H(\epsilon_r - 390) \cong 70 H(\epsilon_r - 390)\,\mu$b

► Bethe Heitler

Another interaction that is a part of the photohadronic processes is Bethe Heitler, where a high energy proton collides with a photon, to produce an electron-positron pair: $p + \gamma \rightarrow p + e^+ + e^-$

The threshold of this interaction can be calculated again from eq.(B.5) is:

$$\gamma_p \epsilon \geq 2 m_e c^2 (1 + \frac{m_e}{m_p}) \simeq 2 m_e c^2 \tag{2.66}$$

Regarding the cross section of B-H (Fig.(22), $\sigma_{\phi\epsilon}$, we use the following approximation[5]:

$$\sigma_{\phi e}\left(\epsilon_r\right) \approx \frac{7}{6\pi}\alpha_f \sigma_{\mathrm{T}} \ln\left(\frac{\epsilon_r}{k_{\phi e}}\right) \tag{2.67}$$

where α_f is the fine structure constant and $k_{\phi e}$ is an adjustable constant $2 \leq k_{\phi e} \leq 6.7$.

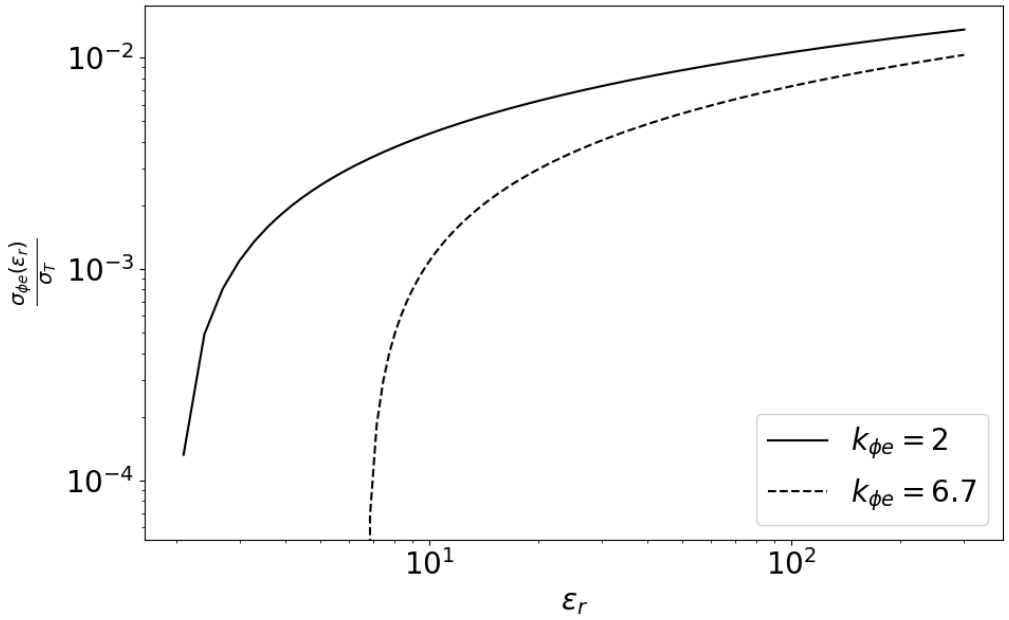

Figure 22: Cross section of B-H process, normalized to the Thomson cross section, as a function of the interaction energy normalized to the electron rest mass energy. The solid curve corresponds to the lower limit of $k_{\phi e}$, whereas the dashed curve stands for its upper limit.

The energy loss rate of a proton due to photopair production is:

$$\begin{aligned}\Gamma_{\phi e}\left(\gamma_p\right) &\cong c\int_0^\infty d\epsilon \oint d\Omega n_{\mathrm{ph}}(\epsilon,\Omega)\left(1-\beta_p\mu\right)\sigma_{\phi e}\left(\epsilon_r\right)\cdot 2m_e c^2\langle\gamma\rangle \\ &\cong \frac{m_e c^3}{\gamma_p}\int_{\gamma_p^{-1}}^\infty d\epsilon \frac{n_{\mathrm{ph}}(\epsilon)}{\epsilon^2}\int_2^{2\gamma_p\epsilon} d\epsilon_r \epsilon_r \frac{\sigma_{\phi e}\left(\epsilon_r\right)}{\sqrt{1+2\epsilon_r}}\end{aligned} \tag{2.68}$$

where $\langle\gamma\rangle = \frac{\gamma_p}{\sqrt{1+2\epsilon_r}}$ is the mean Lorentz factor of the produced pair.

Lastly, substituting eq.(2.67) into eq.(2.44) and assuming $\epsilon_r \gg 1$, we obtain the inverse of the timescale energy loss:

$$\begin{aligned}t_{\phi e}^{-1}\left(\gamma_p\right) = \left(\frac{\Gamma_{\phi e}\left(\gamma_p\right)}{m_p c^2 \gamma_p}\right) &\cong \frac{7 m_e \alpha_f c \sigma_{\mathrm{T}}}{9\sqrt{2}\pi m_p \gamma_p^2}\int_{\gamma_p^{-1}}^\infty d\epsilon \frac{n_{\mathrm{ph}}(\epsilon)}{\epsilon^2} \\ &\times\left\{\left(2\gamma_p\epsilon\right)^{3/2}\left[\ln\left(\frac{2\gamma_p\epsilon}{k_{\phi e}}\right)-\frac{2}{3}\right]+\frac{2}{3}k_{\phi e}^{3/2}\right\}\end{aligned} \tag{2.69}$$

[5]The equations 2.67,2.68 and2.69 can be found in Dermer & Menon (2009) [20]

2.4 Neutrino emission

As we described in the cases of p-p and p-γ (photopion) interactions, they lead to production of pions, which generate flux of neutrinos, via decay processes. The neutrino energy is related to the proton energy as:

$$\epsilon_\nu \simeq 0.05\epsilon_p \tag{2.70}$$

The neutrino luminosity can also be related to proton luminosity by:

$$\varepsilon_\nu L_{\varepsilon_\nu} \approx \frac{3K}{4(1+K)} f_{pp/p\gamma}\, \varepsilon_p L_{\varepsilon_p} \tag{2.71}$$

This K factor shows the averaged ratio of charged to neutral pions produced. For pp processes, $K = 2$, but for photopion interaction, $K = 1$. Additionally, the factor $\frac{3}{4}$ accounts for the production of electron-positron pairs in the decay chain of pions and muons.

Lastly, when we calculate these quantities into the observer's frame, we need to make the Doppler beaming corrections (see Appendix A):
$\epsilon_\nu = \delta\epsilon_\nu{}'$
$\varepsilon_\nu L_{\varepsilon_\nu} = \delta^4 \varepsilon_\nu{}' L_{\varepsilon_\nu}{}'$

3 A physically motivated AGN model

In this section, we will describe our model for the multi-messenger emission from blazar jets. We will discuss the jet composition and assumptions, regarding the external radiation field in the vicinity of the jet. Based on this analysis, we will obtain expressions for the main model quantities as a function of basic parameters, such as the magnetization of the plasma flow and the accretion rate of the blazar.

3.1 Model

We will construct an emission model for blazar jets, assuming that particles are accelerated via magnetic reconnection in a proton-electron plasma. In particular, we assume that the emission comes from a plasmoid inside the jet, which will be referred as blob.

3.1.1 Main parameters

We describe next the main parameters, that most of the quantities of the model would be dependent by them.

Firstly, μ, which is defined as the total energy flux per unit rest mass energy flux, is one of the quantities that remains constant in an ideal magnetohydrodynamic outflow ([41],[77]), and it is calculated for a cold outflow, as:

$$\mu = \Gamma(1+\sigma) \tag{3.1}$$

where Γ and σ are the flow bulk Lorentz factor and magnetization (defined in eq.(2.1)), respectively.

Since μ, Γ and σ are connected, we can express the other model quantities as a function of two of these parameters.

Moving on, we also need to address the role of accretion rate in this model. The dimensionless accretion rate, normalized to the Eddington rate, can be defined as:

$$\dot{m} = \frac{\dot{M}}{\dot{M}_{\rm Edd}} \tag{3.2}$$

where $\dot{M}$ is the accretion rate into the black hole and $\dot{M}_{\rm Edd}$ is the Eddington mass rate and it is defined as follows:

$$\dot{M}_{\rm Edd} \equiv \frac{L_{\rm Edd}}{\eta_{\rm d} c^2} \tag{3.3}$$

where $\eta_{\rm d}$ is the radiative efficiency of the disk, which a typically used value for it is $\eta_{\rm d} = 0.1$. The radiative efficiency may vary from values of 6% to 42% ([42]) in different accreting regimes (for low values ($\dot{m} \leq 0.03$), the disk is radiatively inefficient). $L_{\rm Edd}$ is the Eddington luminosity

of a spherically accreting compact object that its value can be found if the mass of the black hole is known:

$$L_{\text{Edd}} = 1.26 \times 10^{38} \frac{M}{M_{\odot}} erg/s \tag{3.4}$$

In our model, we assume that $\dot{m}$ and Γ are related to each other. This choice is motivated by observational findings. More specifically, Lister (2009) [43] shown in his work on "Monitoring Of Jets in Active galactic nuclei with VLBA Experiments" (MOJAVE), that there is a strong correlation between apparent jet speed and apparent radio luminosity of a big sample of AGN that were observed. Other works [17] investigated the correlation between the intrinsic jet luminosity and the Lorentz factor by performing Monte-Carlo simulations , pointing to a positive correlation. Following these results, we use:

$$\frac{\dot{m}}{\dot{m}_{\text{o}}} = \left(\frac{\Gamma}{\Gamma_{\text{o}}} \right)^{s} \tag{3.5}$$

In order to make an estimation of s, [65] performed a series of simulations, selecting eventually $s = 3$, since the results did not vary significantly in the range of $2.4 \leq s \leq 3.5$. Moreover, [44] presented another MOJAVE study of 409 radio-loud AGN, where estimating the distribution of maximum jet speeds, it was found that $\Gamma_{\text{max}} \approx 50$. Consequently, we set $(\Gamma_{\text{o}}, \dot{m}_{\text{o}}) = (40, 1)$, to even cover the extreme case of a super-Eddington accreting AGN (for selected μ and σ).

Using the above arguments, eq.(3.5) is written as:

$$\dot{m} = 1.56 \times 10^{-5} \Gamma^{3} \tag{3.6}$$

3.1.2 External radiation field

For our purposes, another useful parameter is the radiation energy density produced by the emission of the Broad Line Region (BLR). BLR is believed to be reprocessed radiation from the accretion disk, as described in ch.1. Assuming that the emission is isotropic and monochromatic, the energy density of the external BLR is parametrised as ([28]):

$$u_{\text{BLR}} = \eta_{\text{BLR}} \frac{L_{\text{d}}}{4\pi c R_{\text{BLR}}^{2}} \tag{3.7}$$

where we calculate the BLR radius from the equation $R_{\text{BLR}} = 10^{17} L_{\text{d,45}}^{1/2}$ cm [6] ([37], [28]) and η_{BLR} is the covering factor.

[6] The distance of the BLR is assumed to be a function of the disk luminosity, as indicated by observations through the reverberation mapping technique ([10]). This technique swaps spatial resolution for time resolution, allowing black hole mass measurements and the determination of the size scales of emitting regions associated with X-rays, the UV/optical continuum, BLR, and dusty torus. The basic principle of reverberation mapping is to measure the time delay, or lag, between flux variations in an ionizing source, and the flux variations from the surrounding region that is being irradiated.

In the comoving frame of the blob, the energy and energy density of BLR photons will be respectively:

$$\epsilon'_{\rm BLR} \approx \Gamma \epsilon_{\rm BLR} \tag{3.8}$$

$$u'_{\rm BLR} \approx \Gamma^2 (1 + \frac{\beta^2}{3}) u_{\rm BLR} \tag{3.9}$$

where $\beta \equiv \sqrt{1 - \Gamma^{-2}}$ is the bulk speed of the flow in units of the speed of light.

3.1.3 Emission region

We take the emission region is to be at the outer edge of the BLR, regardless of the choice of μ and σ , and is approximated by a spherical blob in the comoving frame of the fluid:

$$R_{\rm em} = 0.9 R_{\rm BLR} \tag{3.10}$$

As found in Padovani et al. (2019) ([53]), where the emission of TXS0506+056 was studied, γ-γ opacity constraints allow the emitting region to be at the outer edge of the BLR, since stronger absorption of γ rays would have been expected, if the emission region were closer to the central engine. In Fig.(23), we demonstrate how the location of the emission region is related to Γ.

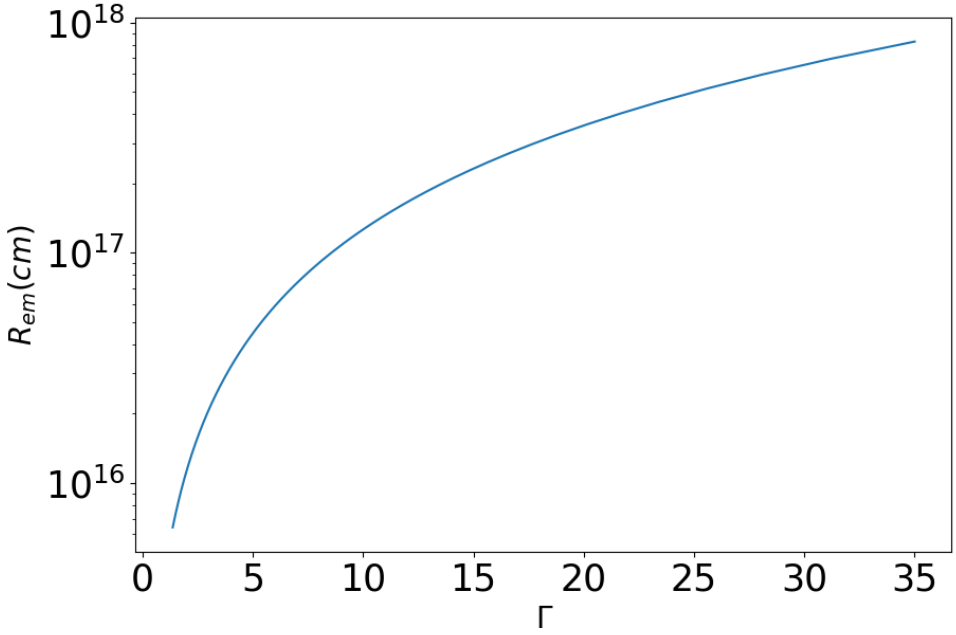

Figure 23: Emission region, $R_{\rm em}$, as a function of the bulk Lorentz factor, Γ of the jet, for selected values of $\mu = 70$ and $\sigma = 1 - 50$

.

We can estimate the radius of the emitting blob, in the comoving frame of the flow, as follows:

$$R'_{\rm b} = R_{\rm em} \theta_{\rm j} \tag{3.11}$$

where $\theta_{\rm j} = 1/\Gamma$ is the half opening angle of the conical jet.

Using eq.(3.10) one can write $R'_{\rm b}$ as:

$$R'_{\rm b} \sim 4.05 \times 10^{15}\sqrt{\Gamma} \tag{3.12}$$

In order to obtain eq.(3.10), we took into account that the disk luminosity can be written as:

$$L_{\rm d} = \eta_{\rm d}\dot{M}c^2 \tag{3.13}$$

Then, combining eq.(3.13) with eqs.(3.2),(3.6), we find that $L_{\rm d}$ is related with $\dot{m}$ as: $L_{\rm d} \propto \dot{m} \propto \Gamma^3$ which leads to the scaling relation between $R'_{\rm b}$ and Γ, found in eq.(3.12).

Because of the assumed location of the emission region (3.10), FSRQs are expected to be more luminous, due to the IC upscattering of BLR photons. On the contrary, if the emission region was located outside the BLR, it would lead to a significantly fainter IC component.

3.1.4 Jet composition

Starting with the jet luminosity, we consider that it is linked with the accretion rate ([13], keeping in mind the expression of the disk luminosity (eq.(3.13)).

$$L_{\rm j} = \eta_{\rm j}\dot{M}c^2 \tag{3.14}$$

where $\eta_{\rm j}$ is the jet production efficiency (see Table 1)

Consequently, combining eq.(3.14) and (3.3) we find that L_j is depends only on $\dot{m}$ (and the black hole mass):

$$L_{\rm j} = \frac{\eta_{\rm j}}{\eta_{\rm d}} L_{\rm Edd}\dot{m} \tag{3.15}$$

An outflow can be described by two parts of energy fluxes, as found in MHD theory; one that corresponds to matter (kinetic and thermal component, described by enthalpy), and one that is about the electromagnetic field (Poynting flux). The ratio of these parts is called magnetization and it is defined as:

$$\sigma = \frac{L_{\rm B}}{L_{\rm kin}} = \frac{L_{\rm B}}{L_{\rm j} - L_{\rm B}} \tag{3.16}$$

where $L_{\rm kin}$ is the kinetic power of the jet and is determined by cold plasma. Using the definition of the power of the magnetic component of the jet, we can calculate the magnetic energy density of the emitting blob, in the comoving frame:

$$u'_{\rm B} = \frac{L_{\rm B}}{2\pi {R'_{\rm b}}^2 c\beta\Gamma^2} \tag{3.17}$$

where $R'_{\rm b}$ is the size of the emission region.

Knowing that the magnetic energy density is given by $u'_{\rm B} = \frac{B^2}{8\pi}$, we can derive an expression for the magnetic field, using eqs.(3.16) and (3.17):

$$B' = \sqrt{\frac{4\sigma L_j}{(1+\sigma){R'_b}^2 c\beta\Gamma^2}} \tag{3.18}$$

Using eqs.(3.6),(3.11) and (3.15), we can express the magnetic field only as a function of the magnetization, assuming $\eta_j = 0.9$:

$$B' \approx 11.6 \left(\frac{1}{\beta}\right)^{1/2} \left(\frac{\sigma}{\sigma+1}\right)^{1/2} \ \text{G} \tag{3.19}$$

Obviously, one can see how B' changes as a function of μ and Γ, by applying eq.(3.1) above:

$$B' \approx 11.6 \left(\frac{1}{\beta}\right)^{1/2} \left(\frac{\mu-\Gamma}{\mu}\right)^{1/2} \ \text{G} \tag{3.20}$$

After the derivation of eq.(3.19) and (3.20), we show the dependence of the magnetic field strength on σ, μ and Γ, in Fig.(24). As expected from eq.(3.19),the magnetic field is stronger when the magnetization takes higher values. Conversely, for higher values of the bulk Lorentz factor, magnetic field is decreased. For a constant value of σ, as μ increases, then Γ will take higher values and that is why the magnetic field will be decreased. Now if we observe the magnetic field, for constant magnetization, it will be only dependent on the $\frac{1}{\beta}$ term, that also depends on μ as shown below:

$$\frac{1}{\beta} = \left(1 - \frac{1}{\left(\frac{\mu}{1+\sigma}\right)^2}\right)^{-1/2} \tag{3.21}$$

It is understandable that this term will be important when $\beta \to 0$. This happens when $\frac{\mu}{1+\sigma} \to 1$. In the case of constant σ, this is valid when μ takes the lowest possible value, according to eq.(3.1). Thus, the magnetic field at the start of each line in Fig.24 has its maximum, and then it converges in a constant lower value.

The derivation of a magnetic field of an almost constant magnitude is a result of the selection of the location of the emission region in respect to the BLR. We can see from eq.(3.18) that the magnetic field is $\propto {R'_b}^{-1}$. This means, that if we have selected the emission region to be at a closer distance to the black hole, e.g. $\sim 0.1 R_{BLR}$, it would lead to magnetic field strengths close to 100G.

Since, we have made a calculation for the magnetic field strength, we, then, derive the cold particle density of the electron-proton jet. Using the definition of magnetization, from eq.(2.1), we reach to the following result:

$$\begin{aligned} &B'^2 = 4\pi\rho' c^2 \sigma \\ &\Rightarrow n'_p = \tfrac{B'^2}{4\pi m_p c^2 \sigma} = \tfrac{148.2}{4\pi m_p c^2} \tfrac{1}{1+\sigma} \tfrac{1}{\beta} \\ &\Rightarrow n'_p = \tfrac{7.8\times 10^3}{(1+\sigma)\beta} \ \ \text{cm}^{-3} \end{aligned} \tag{3.22}$$

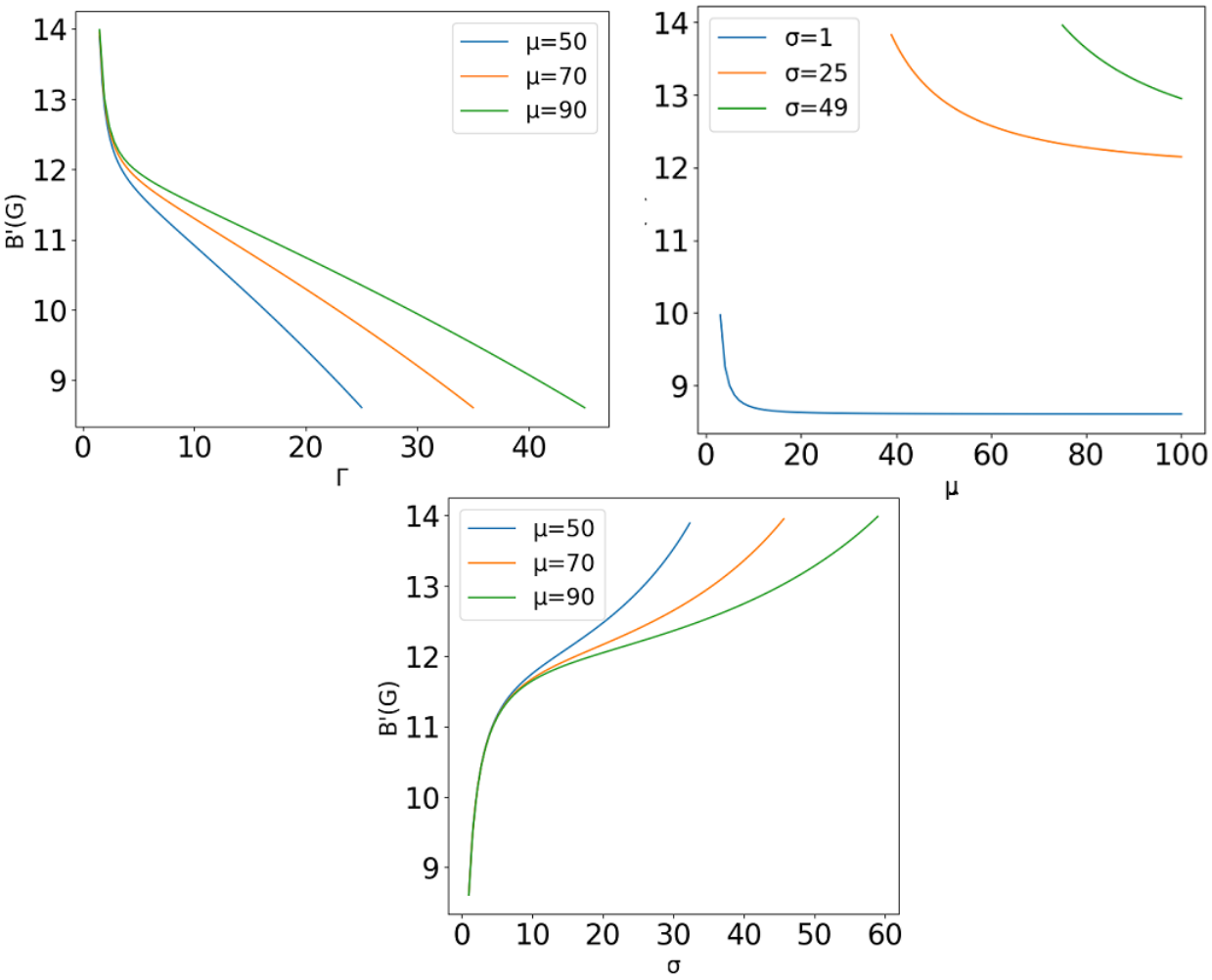

Figure 24: Magnetic field in the frame of the jet fluid, as a function of the main parameters; Γ (left panel), μ (right panel) and σ (bottom panel). In every panel, there are 3 different coloured curves of σ or μ, for comparison. In the top left panel, the values of σ are ranging from 1 to 49, while in the top right panel, Γ is ranging from 1.05 to 50. In the bottom panel, Γ is ranging from 1.5 to 45.

In eq.(3.22, we have assumed quasi neutrality on fluid scales, meaning:

- number density: $n_p = n_e = n$
- mass density: $\rho = n_p m_p + n_e m_e \sim n_p m_p$

An equivalent way of calculating the same quantity is by using the expression of the kinetic component of jet luminosity, where the cold protons are the ones that mainly contribute this part. So, using eq.(3.16), we get an expression that leads to the same result found above:

$$\left.\begin{array}{l} L_{kin} = L_j - L_B = \frac{n_j \dot{M} c^2}{1+\sigma} \\ L_{kin} = 2\pi R_b'^2 \beta \Gamma^2 n_p' m_p c^3 \end{array}\right\} \Rightarrow n_p' = \frac{\eta_j \dot{M}_{edd} \dot{m}}{(1+\sigma) 2\pi R_b'^2 \beta \Gamma^2 m_p c} \sim \frac{7 \times 10^3}{(1+\sigma)\beta} \ \text{cm}^{-3} \qquad (3.23)$$

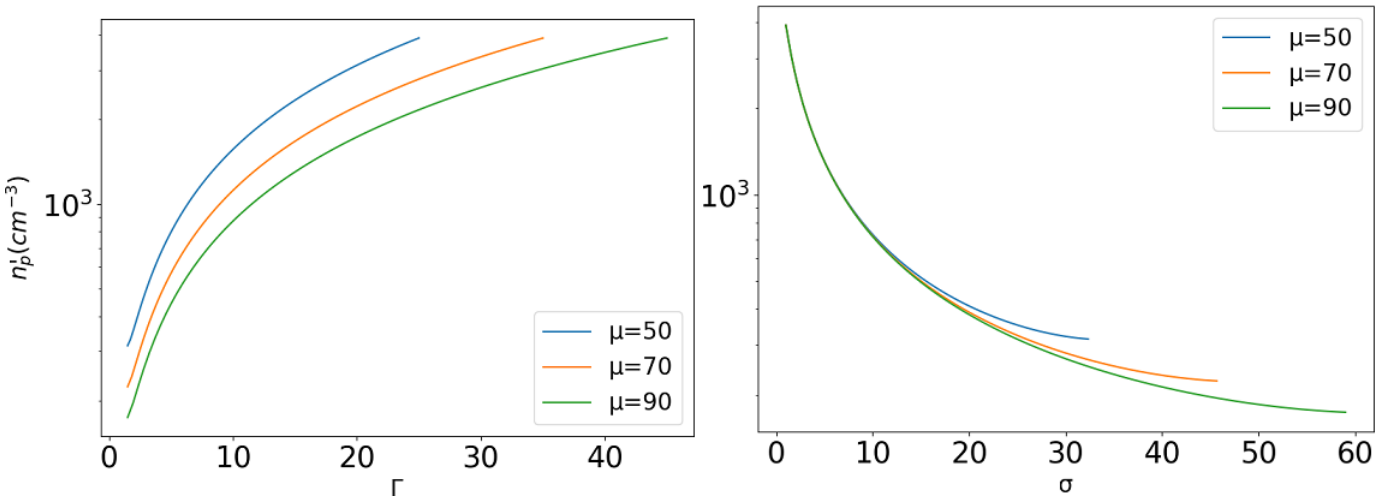

Figure 25: Cold proton density in the frame of the jet fluid, as a function of the main parameters; Γ (left panel), σ (right panel). In every panel, there are 3 different coloured curves of σ or μ, for comparison. To be exact, in the left panel, σ is ranging from 1 to 60, while in the right panel, Γ is ranging from 1.5 to 45.

In both panels in Fig.(25), we show the number density of cold protons in the blob, for constant μ in each coloured line. This behaviour is explained by eq.(3.22), where it is shown that n'_p is inversely proportional to $1+\sigma$. For a fixed value of magnetization (or Γ), there is a small difference of the value of n'_p for different cases of μ. This is because of the term $\frac{1}{\beta}$ in eq.(3.22).

Now, based on the results of magnetic reconnection, as stated in ch. (2.2), we know that particles are being accelerated to relativistic energies due to magnetic energy dissipation. Using eq.(3.17) we can find that the luminosity of the relativistic particles, in the comoving frame of the blob, is:

$$L'_{\mathrm{e(p)}} = f_{\mathrm{rec,e(p)}} \frac{2L_{\mathrm{B}}}{3\beta\Gamma^2} \tag{3.24}$$

where f_{rec} is the fraction of the dissipated magnetic energy that is distributed to particles. This quantity has been estimated by Sironi et. al (2015) ([71]) who computed the ratio of the kinetic energy of the emitting electrons (regarding all the plasmoids in the reconnection layer) to the respective net energy (particle and magnetic energy). In the work of Sironi et al. (2015) this quantity was estimated, regarding emitting electrons, as:

$$f_{\mathrm{rec,e}} \equiv \frac{\sum_i \int_{V'_i} U'_{\mathrm{e}} \mathrm{d}V'_i}{\sum_i \int_{V'_i} (e + \rho c^2 + U'_{\mathrm{B}})\, \mathrm{d}V'_i} \tag{3.25}$$

where V'_i is the volume of each plasmoid, that was produced in the simulation of this study, while e is the overall electron energy density but does not include the rest mass energy density . Also, there was applied a threshold condition of selecting particles with mean Lorentz factors above $\gamma \geq 1.1$ in order for the reconnection downstream region to be identified more efficiently.

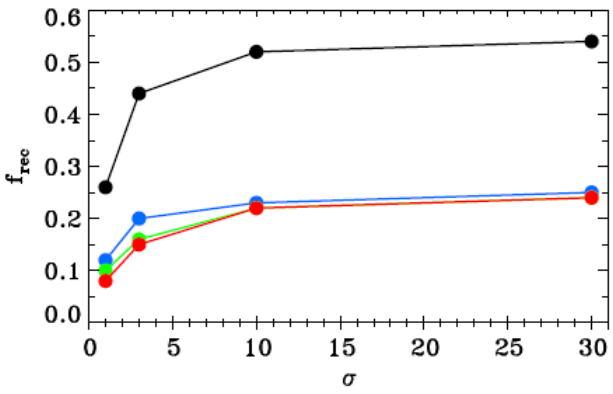

Figure 26: Plot of the dissipative efficiency (top panel) as a function of the flow magnetization for relativistic reconnection in electron-ion plasmas, from a series of 2D simulations. The dependence on the numerical choice of the mass ratio m_p/m_e is illustrated by the colored curves. $m_p/m_e = 1, 6.25, 25, 100$ are shown with black, blue, green and red colour, respectively. Taken from ([71])

Assuming that half of the magnetic energy is converted into internal energy, one can approach $f_{\rm rec}$ using the expression: $f_{\rm rec} \approx 0.5\xi_{\rm e}\sigma/(\sigma+2)$. where $\xi_{\rm e}$ is a fraction of energy that electrons pick up in magnetic dissipation and it is ~ 0.5, regarding electron-proton plasma. Again, in the case of electron-proton plasma, since only the electrons contribute in the numerator of eq.(3.26), f_{rec} is decreased. But, as it is shown in Fig.(26), the value of f_{rec} does not change significantly after $\sigma \sim 10$. Below this value, f_{rec} takes lower values, due to the contribution of the rest mass energy to the denominator. Based on the above, in our model we select f_{rec} to be constant and about ~ 0.15.

Now, coming back to eq.(3.24), assuming $\beta \sim 1$, the particle luminosity can be written as:

$$L'_{\rm i} = 1.77 \times 10^{42} \Gamma \frac{\sigma}{1+\sigma} \ \ {\rm erg/s} \tag{3.26}$$

As we can see from eq.(3.26), the particle luminosity in the jet frame, is mainly dependent on Γ, since the fraction $\frac{\sigma}{1+\sigma}$ does not change a lot, for any value of $\sigma \gtrsim 2$. As shown in Fig.(27) the particle luminosity increases with Γ as we expected. For a constant value of Γ, the luminosity is increased in the case of a higher μ value. Higher μ values, also imply that σ is slightly larger, as known from eq.(3.1). In this case, the fraction $\frac{\sigma}{1+\sigma}$ will be closer to unity, which will lead to greater values of L'_i. Given these, we expect FSRQs to be more luminous objects than BL Lacs assuming that the radiative efficiency is the same and since their bulk Lorentz factor is higher. Taking into account, that luminosity will be boosted in the observer's frame due to relativistic beaming, we expect an even bigger difference.

3.1.5 Particle Distribution

PIC simulations of relativistic magnetic reconnection have demonstrated the generation of non-thermal power laws (see Ch.2.2). Based on that we model the injection rate of relativistic

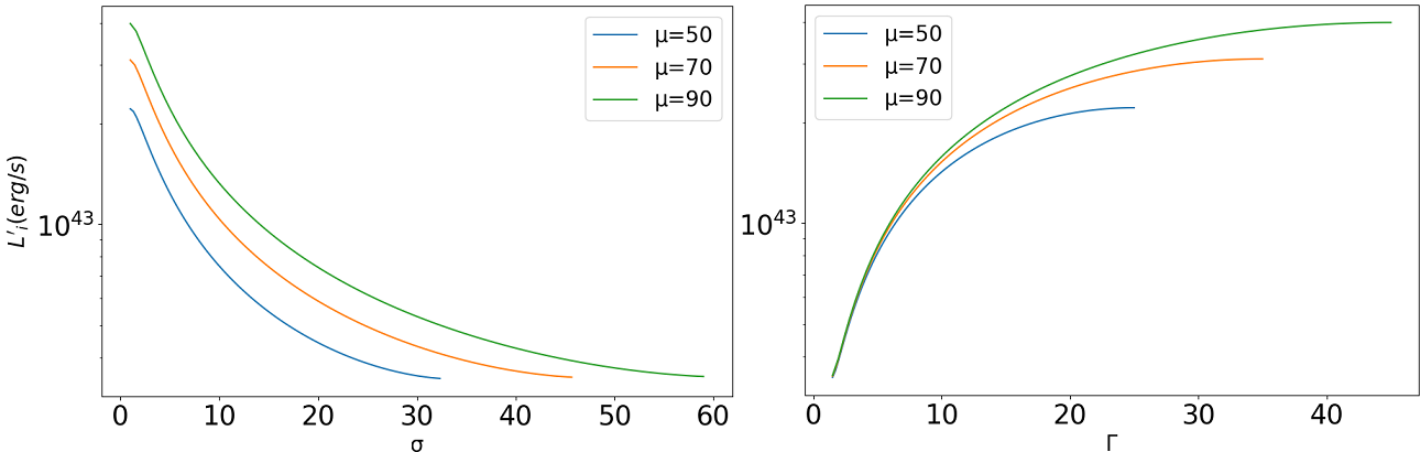

Figure 27: Plot of the particle luminosity as a function of the flow magnetization (left panel) and the bulk Lorentz factor (right panel). Colored lines stand for selected values of μ.

particles as:

$$Q'(\gamma') = Q_o \gamma'^{-p} \quad for\ \gamma'_{\text{min}} < \gamma' < \gamma'_{\text{max}} \tag{3.27}$$

where γ'_{min} and γ'_{max} are the minimum and maximum values of the Lorentz factor, respectively, and Q_o is a normalization parameter in units of $\frac{1}{sec\ cm^3}$

The normalization factor can be obtained by calculating the power of particles, using eqs.(3.26),(3.27):

$$\begin{aligned} L_i{}' &= V' \int_{\gamma'_{\text{min},i}}^{\gamma'_{\text{max},i}} d\gamma' \left(\gamma' m_i c^2\right) Q'\left(\gamma'\right) \\ &= V' Q_0 m_i c^2 \int_{\gamma'_{\text{min},i}}^{\gamma'_{\text{max},i}} d\gamma' \cdot \gamma'^{1-p} \end{aligned} \tag{3.28}$$

where V' is the volume of the emission region $V' = \frac{4}{3}\pi {R_b}'^3$.

Solving for Q_o we find:

$$Q_o = \frac{4 L_B f_{rec}}{3\beta\Gamma^2 V' m_i c^2 I} \tag{3.29}$$

where I is given by:

$$I = \begin{cases} \frac{\gamma'^{2-p}_{\text{max}} - \gamma'^{2-p}_{\text{min}}}{2-p} & , p \neq 2 \\ \ln\left(\frac{\gamma'_{\text{max}}}{\gamma'_{\text{min}}}\right) & , p = 2 \end{cases} \tag{3.30}$$

3.1.6 Minimum and Maximum Lorentz Factors

In the reconnection region, the magnetic energy available per particle in an electron - proton jet is $\sim \sigma m_p c^2$. After the reconnection takes place the average energy per particle will be $\sim$

$f_{rec}\sigma m_p c^2$. Therefore, the electron mean Lorentz factor is:

$$\langle \gamma'_e \rangle \sim f_{rec}\sigma \frac{m_p}{m_e} \tag{3.31}$$

In the same manner, for protons, the mean Lorentz factor will is:

$$\langle \gamma'_p \rangle \sim f_{rec}\sigma \tag{3.32}$$

Using the definition of mean value for the Lorentz factor, we get:

$$\langle \gamma' \rangle = \frac{\int_{\gamma'_{\rm min}}^{\gamma'_{\rm max}} d\gamma' \gamma'^{-p+1}}{\int_{\gamma'_{\rm min}}^{\gamma'_{\rm max}} d\gamma' \gamma'^{-p}} = \frac{\gamma'^{-p+2}\Big|_{\gamma'_{\rm min}}^{\gamma'_{\rm max}}}{\gamma'^{-p+1}\Big|_{\gamma'_{\rm min}}^{\gamma'_{\rm max}}} \frac{1-p}{2-p} = \frac{1-p}{2-p} \frac{{\gamma'_{\rm max}}^{2-p} - {\gamma'_{\rm min}}^{2-p}}{{\gamma'_{\rm max}}^{1-p} - {\gamma'_{\rm min}}^{1-p}} \tag{3.33}$$

For the case of $p > 2$ and assuming that $\gamma'_{\rm max} \gg \gamma'_{\rm min}$, eq.(3.33) becomes:

$$\begin{aligned} \langle \gamma' \rangle &= \frac{{\gamma'_{\rm min}}^{2-p}}{{\gamma'_{\rm min}}^{1-p}} \left(\frac{1-p}{2-p}\right) \\ \Rightarrow \langle \gamma' \rangle &= \gamma'_{\rm min} \left(\frac{1-p}{2-p}\right) \\ \Rightarrow \quad \gamma'_{\rm min} &= \langle \gamma' \rangle \, \frac{2-p}{1-p} \end{aligned} \tag{3.34}$$

From eqs.(3.31),(3.32) we find that the minimum Lorentz factor for electrons and protons, respectively, is:

$$\begin{aligned} \gamma'_{{\rm min},e} &= \left(\frac{2-p}{1-p}\right) f_{rec}\sigma \cdot \frac{m_p}{m_e} \\ \gamma'_{{\rm min},p} &= \left(\frac{2-p}{1-p}\right) f_{rec}\sigma \end{aligned} \tag{3.35}$$

In the case where the slope p takes values of $1 < p < 2$ and assuming $\gamma'_{\rm max} \gg \gamma'_{\rm min}$, we find:

$$\begin{aligned} \langle \gamma' \rangle &= -\left(\frac{1-p}{2-p}\right) \frac{{\gamma'_{\rm max}}^{2-p}}{{\gamma'_{\rm min}}^{1-p}} \\ \Rightarrow \gamma'_{\rm max} &= \left[\frac{2-p}{p-1} {\gamma'_{\rm min}}^{1-p} \langle \gamma' \rangle\right]^{1/(2-p)} \end{aligned} \tag{3.36}$$

Taking into account that the mean energy per particle can not exceed $(\sigma+1)m_p c^2$, then eq.3.36 will be for electrons and protons, respectively:

$$\gamma'_{{\rm max},e} = \left[\frac{2-p}{p-1} \, {\rm f_{rec}} (\sigma+1) \frac{m_p}{m_e}\right]^{1/(2-p)} \quad {\gamma'_{\rm min}}^{(1-p)/(2-p)} \tag{3.37}$$

$$\gamma'_{{\rm max},p} = \left[\frac{2-p}{p-1} \, {\rm f_{rec}} (\sigma+1)\right]^{1/(2-p)} \quad {\gamma'_{\rm min}}^{(1-p)/(2-p)} \tag{3.38}$$

where we have assumed that $\gamma_{\text{min},p} \sim 1$ and $\gamma_{\text{min},e} \sim 10^3$, following roughly eqs.(3.31), (3.32).

We also need to make an estimation for the maximum Lorentz factor that particles can reach, in the case of $p > 2$, where we have low magnetization. For both electrons and protons, we need to take into account the cooling timescales of the mechanisms that occur in each species. Then, we equate the total cooling timescale with the acceleration timescale ([64],[83]), which is estimated like this:

$$t_{acc} = \frac{\eta_{acc} r_g}{c} \tag{3.39}$$

where r_g is the gyroradius of the particle and η_{acc} is the number of gyrations the electron experiences before it is injected to the system.

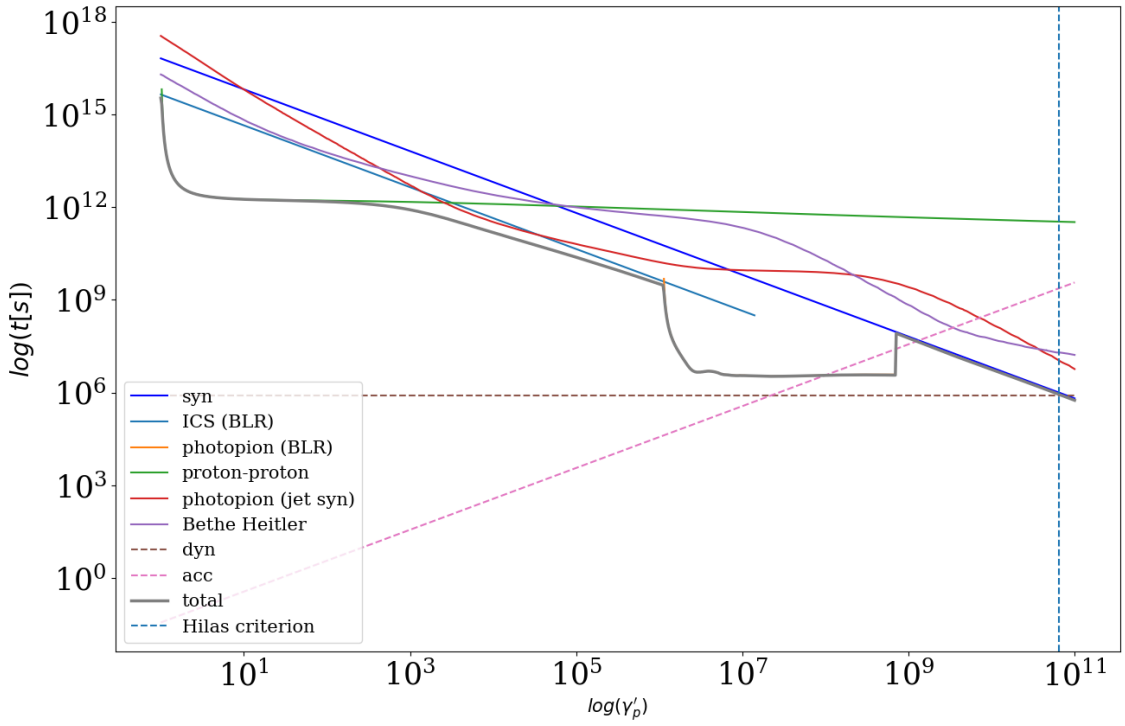

Figure 28: The timescales of proton radiative mechanisms as a function of the proton Lorentz factor in the case of $(\sigma, \mu) = (1, 70)$. Dynamical and acceleration timescales are shown in purple and brown dashed lines, respectively. Hillas criterion[8] is also shown with the vertical dashed blue line.

As mentioned, in order to constrain the maximum Lorentz factor of protons, we need to equate the radiative cooling timescales with the acceleration timescale. As it is shown in eq.(3.39), this is dependent on η_{acc} which is a free parameter. In the work of Rueda Becerril et al. (2020) ([65]) this parameter is taken to be $\approx 10^6$. However, other studies consider this parameter really low, closer to 1. In our work, we selected η_{acc} to be closer to 10^3, which leads $\gamma'_{\text{max},p}$ to be about 10^8 in all cases. However, even if we had selected η_{acc} to be closer to unity, then we would have been led to similar results, due to the steepness of the power law spectra,

Parameter	Value
θ_{obs}	2°
M_{BH}	$10^9 M_{\odot}$
η_d	0.1
η_j	0.9
η_{BLR}	0.1
Γ_o	40
s	3.0
ϵ_{BLR}	2 eV
μ	$50, 70, 90$
(σ, p)	$(1, 3.0), (3, 2.5), (10, 2.2), (15, 2.0), (30, 1.5), (50, 1.2)$
$\gamma_{\text{min},p}(p \geq 2)$	1
$\gamma_{\text{min},e}(p \geq 2)$	10^3

Table 1: Parameter values

for $\sigma \leq 15$ (see blue dashed line in Fig.(33). As for $\sigma \geq 15$, in spite of the fact that the energy is carried by the highest energy particles(Fig.(33)), the acceleration of particles is limited from eq.(3.35), which actually leads to low values of Lorentz factors. This problem is taken into account in the study of Petropoulou & Sironi (2018) ([60]).[9] The comparison of all timescales can be shown in Fig.(28 and 29) where we show two extreme cases of magnetization; one where $\sigma = 1$ and one where $\sigma \approx 50$. The Hillas criterion was also taken into account, although it does not constrain our final results. The main conclusions regarding these two extreme cases are the following; in the case of low magnetization, the acceleration is limited by the photopion losses due to interaction with BLR photons, whereas for high magnetizations acceleration is limited by photopion losses, attributed to jet photons. Moreover, even if it does not contribute to the spectra, we see that moving to higher magnetization, the synchrotron losses become more important compared with the corresponding losses of ICS, due to the fainter BLR in these cases. This indicates that the same result will hold for electrons, where in their case, they contribute to the photon spectra. Lastly, we see that p-p interactions are not considered in our results, since in all cases the efficiency of this process is significantly low compared to pγ interactions.

We see in Figs.(30 and 31) that a major difference comparing the pγ interactions with BLR and synchrotron photons, is that in the latter case the threshold condition for these interactions is satisfied even when $\gamma'_p = 1$ because there are still internal (ICS) photons in suitable energies. On the other hand, proton interactions with BLR start to happen in $\gamma'_p \approx 10^6$. This is because BLR is taken to be monochromatic with energy $\epsilon'_{BLR} = \Gamma \epsilon_{BLR} = 2\Gamma$eV. Using the threshold condition, we see that $\gamma'_{p,th} \propto 1/\Gamma$. This is why these interactions in the case of $(\sigma, \mu) = (50, 70)$ take place for a higher proton Lorentz factor value.

[9] In this study, is shown , in spite of earlier studies which imply that the particle high energy spetral cutoff saturates at $\gamma \sim 4\sigma$, that actually in later times of simulations, the cutoff Lorentz factor still grows, and actually it scales with time as $\gamma_{cut} \propto \sqrt{t}$. Moreover, it was shown that particles could be further energized if they enter into acceleration/compression cycles. This can happen in the case where two plasmoids are merging. Then, particles could experience a large energy increase within a short time interval by the anti-reconnection electric field at the interface between the two merging plasmoids. However, this is a suggestive solution for a case of a series of plasmoids that interact with each other. This is not a case in our model where we take into account the emission of a sole plasmoid.

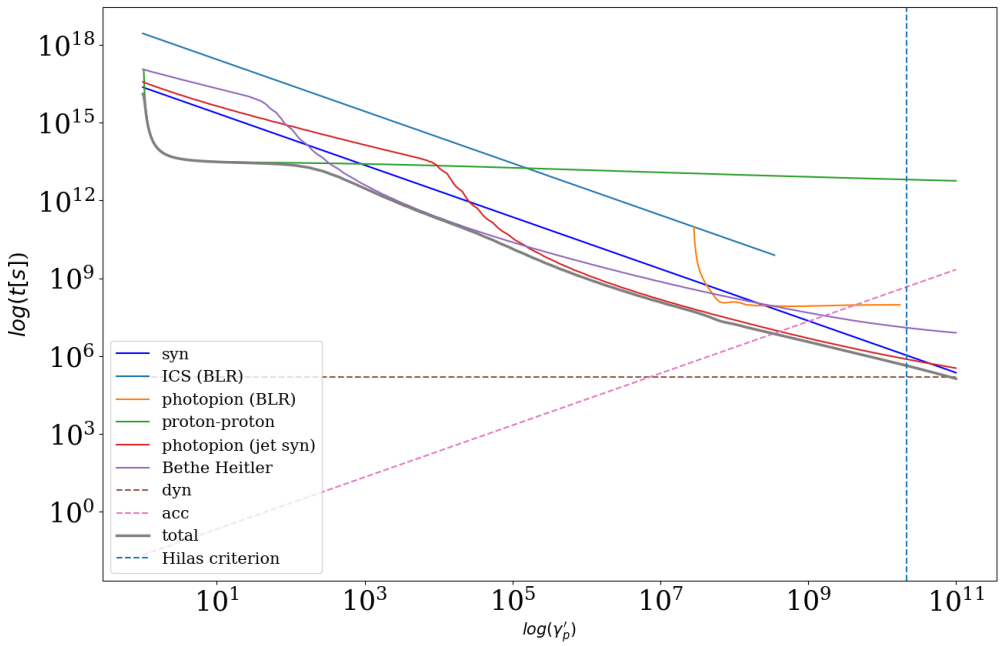

Figure 29: The timescales of proton radiative mechanisms as a function of the proton Lorentz factor in the case of $(\sigma, \mu) = (50, 70)$. Dynamical and acceleration timescales are shown in purple and brown dashed lines, respectively. Hillas criterion is also shown with the vertical dashed blue line.

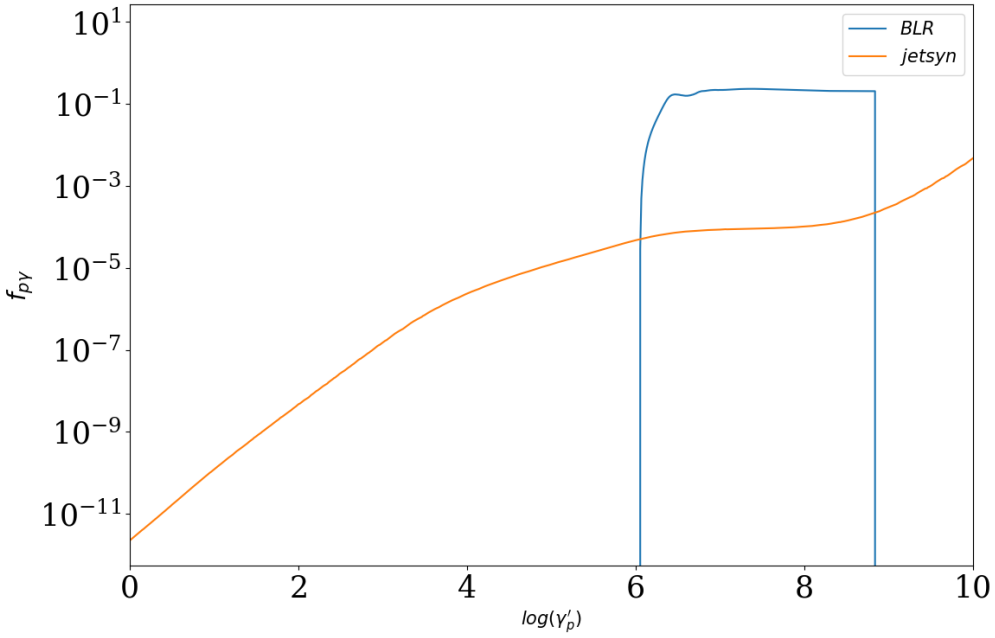

Figure 30: The efficiency of proton interactions that lead to neutrinos as a function of the proton Lorentz factor in the case of $(\sigma, \mu) = (1, 70)$. pγ interactions with BLR and jet photons are shown in blue, orange, respectively.

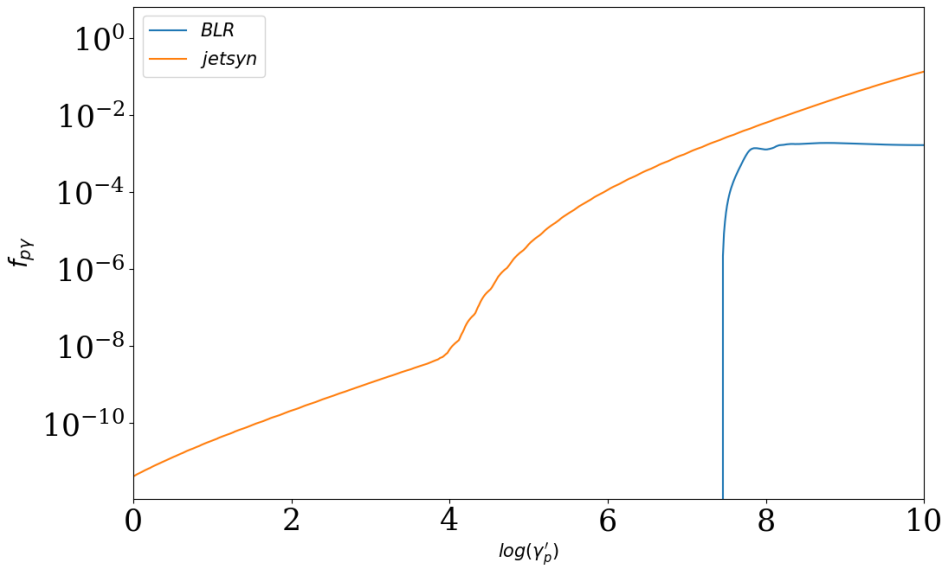

Figure 31: The efficiency of proton interactions that lead to neutrinos as a function of the proton Lorentz factor in the case of $(\sigma, \mu) = (50, 70)$. pγ interactions with BLR and jet photons are shown in blue, orange, respectively.

4 Numerical investigation

In this chapter, we will present the multi-wavelength photon spectra and high-energy neutrino spectra expected in our model for different blazar subclasses.

We present first (Ch. 4.1) the code we used for solving the kinetic equations for each particle distribution, calculating the contribution for each radiative process that should be taken into account. Following this, we present the results we gathered for all the cases of μ and σ, considered.

4.1 Numerical code

The most efficient way of studying and reproducing the spectra of time-variable astrophysical sources is by solving the kinetic equations for the evolution of the radiating particles. Starting, we can select to inject, in a source of radius R, protons and/or electrons with a chosen distribution profile. While these particles radiate through the described processes, they are cooling. Additionally, particles and emitting photons can escape from the source or be absorbed through $\gamma\gamma$ absorption. Following the above, kinetic equations describe how the energy and number density of particles will change in respect to time, inside the source, while they radiate, escape and being further produced.

Generally, we can write the kinetic equations for a homogeneous region containing relativistic hadrons and leptons in the compact form:

$$\frac{\partial n_i}{\partial t} + \frac{n_i}{t_{esc}} + S_i + Q_i = 0 \tag{4.1}$$

where index i refers to protons (hereafter denoted by p), electrons/positrons (e), photons (γ), neutrons (n) and neutrinos (ν). Also, n_i is the particle number density, Q_i is the injection rate of particles in the source, S_i is a term regarding the particle losses and $t_{esc} \sim R/c$, is the time that particles need to cross the radius of the source, if the source is assumed to be spherical.

We compute steady state photon and neutrino spectra for blazars by solving the equations until a state of equilibrium[10] between the particle injection and their cooling due to radiative losses and their escape from the sources, is reached.

In this work, we considered a leptohadronic model for blazars where both protons and electrons are accelerated to relativistic energies via reconnection. Protons can lose energy by interactions with photons, like Bethe-Heitler and photopion production. Photopion leads to the production of unstable secondary particles, like neutral or charged pions and muons, and their decay into electrons, positrons, neutrons and neutrinos. Some secondary particles like electrons, positrons will produce synchrotron emission, as well. Taking all these into account, the kinetic equation for stable particle species are shown in Fig.(4.1).

[10]This equilibrium is usually referred as steady state. In a steady state problem, the solution does not longer

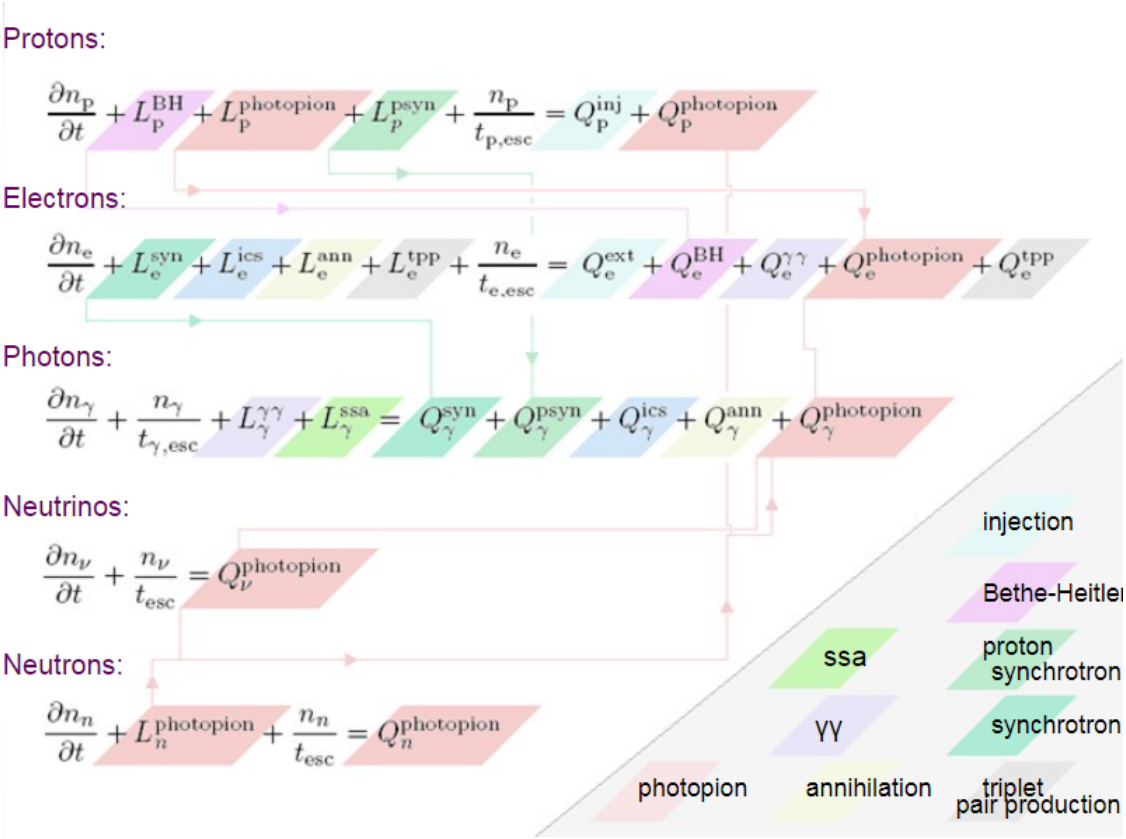

Figure 32: The kinetic equations that are solved for each particle species. Adapted from [22]

In this study, in order to compute the blazar electromagnetic and neutrino emission we use the numerical code ATHEνA ([47],[48],[22]). The main parameters, used in the numerical code, are characterized in a dimensionless manner and are computed in the frame of the source, such as:

- number density
$$\bar{n'} = n'\sigma_\tau R'_b m_e c^2$$
- time, normalized to the crossing time $\tau = \frac{t}{t_{cross}}$
- compactness, which is a dimensionless measure of luminosity,
$$l'_{e(p)} = \frac{L'_{e(p)}\sigma_T}{4\pi R'_b m_{e(p)} c^3}$$
- energy density of external photon field, in terms of compactness
$$l'_{ext} = \frac{U'_{ext}\sigma_T R'_b}{m_e c^2}$$

Furthermore, for each run, we need to set values to some physical parameters, such as:

depend on the time evolution, since energy gains and losses have been balanced. This, also, implies that the following term would be: $\frac{\partial n_i}{\partial t} \to 0$

- The radius of the source,R_b
- The magnetic field, B
- Minimum and maximum Lorentz factors of electrons and protons
- The slope of the power law of electron and proton distribution
- In the case of an external radiation field, the compactness and temperature of a gray body field.
- The terminal time, where the code will stop performing calculations. Generally, this time is selected in order to correspond to a steady state result.

The code solves the kinetic equations for a time interval, which its ending point is set as a free parameter normalized to the crossing time, t_{cross}. The results of the code are saved in files where information about photon and neutrino luminosity and the particle distributions can be obtained. Particularly, we can derive the SED for photons and neutrinos in the observer's frame, by performing the following, in the dimensionless quantities the code derived.

- photon/neutrino energy $\epsilon_{obs} = \frac{\delta x}{m_e c^2}$
- photon/neutrino luminosity $\epsilon L_{\epsilon,obs} = \frac{x^2 \bar{n}_\gamma(x) m_e c^2 \delta^4}{\sigma_\tau R'_b} 4\pi {R'_b}^2 c$

where x and $x^2\bar{n}_\gamma(x)$ are the dimensionless qualities, calculated in the source frame, obtained by the code.

4.2 Results

After setting up the model in ch.(3), we can present the results we gathered from our calculations and the ATHEνA code, as well. We have selected 18 cases in total, for $\mu = 50, 70, 90$ and $\sigma = 1, 3, 10, 15, 30, 50$.[11] Depending σ, we will often refer to objects as FSRQs (for $\sigma \leq 10 - 15$) or as BL Lacs (for $\sigma \geq 15$).

First, we show Fig.(33) in order to highlight the main differences between two extreme cases of magnetization ($\sigma = 1$ and $\sigma \approx 49$). The main components that are illustrated in these plots are the photon and neutrino spectra, the proton differential luminosity and the BLR emission spectrum. For the photon spectra, we can see the dominance of the high energy component and in the case of low magnetization, as opposed to the case of $\sigma \approx 49$. The emission that forms the bumps is attributed to electrons, while hadronic emission (synchrotron and ICS) either is less luminous, and therefore covered by the leptonic emission, or it is absorbed by lower energy photons, in the case where photons are produced by the decay of neutral pions. Emission from e^+e^- pairs produced by Bethe Heitler is located in the GeV-TeV regime, but is also absorbed

[11] Actually, the value we selected is $\sigma = 48.9$, otherwise it would be impossible to select $\mu = 50$ at the same time.

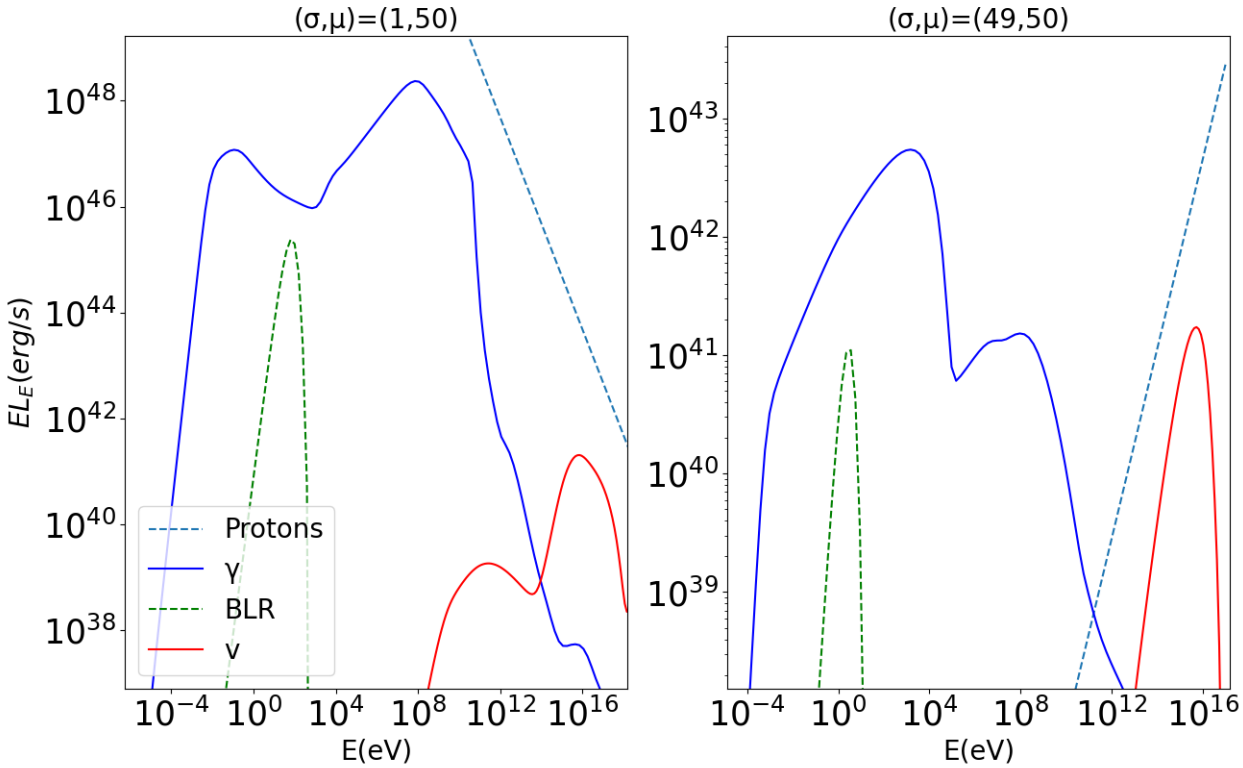

Figure 33: The photon and neutrino spectra in the case of $(\sigma, \mu) = (1, 50)$ (left) and $(\sigma, \mu) = (49, 50)$ (right). BLR and the proton distribution is shown in green dashed line and blue dashed line, respectively.

and therefore suppressed. Moreover, neutrinos are produced and their emission peaks in PeV energies. In the case of low magnetization, two bumps are observed and their luminosity is much lower, compared to that of photons. On the other hand, for $\sigma \approx 49$, neutrino luminosity is comparable with the photon luminosity in the MeV-GeV range. Lastly, the proton spectrum is steep in the case of $\sigma = 1$, but as magnetization increases it gets harder, which leads to the result that is shown in the right panel of Fig.(33). As explained by the results of the simulations for magnetic reconnection, the particle distributions that are produced are strongly related to magnetization. Most of the energy is transferred and carried by low energy protons, in the case of low magnetization, as opposed to high values of σ, where most of the energy is transferred to the most energetic particles of the distribution.

In Figs. (34),(35) and (36) we present the spectra of photons and neutrinos, for $\mu = 50$, $\mu = 70$ and $\mu = 90$, respectively, and all σ considered. We observe similar patterns, for any case of μ examined, that are going to explained below.

Regarding the photon spectra, it is obvious that FSRQs are much brighter than BL Lac objects. Especially, objects with the lowest magnetization are the most luminous, which is due to Doppler boosting, where $\delta \sim 2\Gamma$ for very small observing angles ($\theta_{obs} \to 0$). For all cases, the lower energy hump is attributed to synchrotron radiation from electrons and the higher energy hump is explained by external IC with BLR photons, for $\sigma \leq 15$, while for cases where $\sigma \geq 15$,

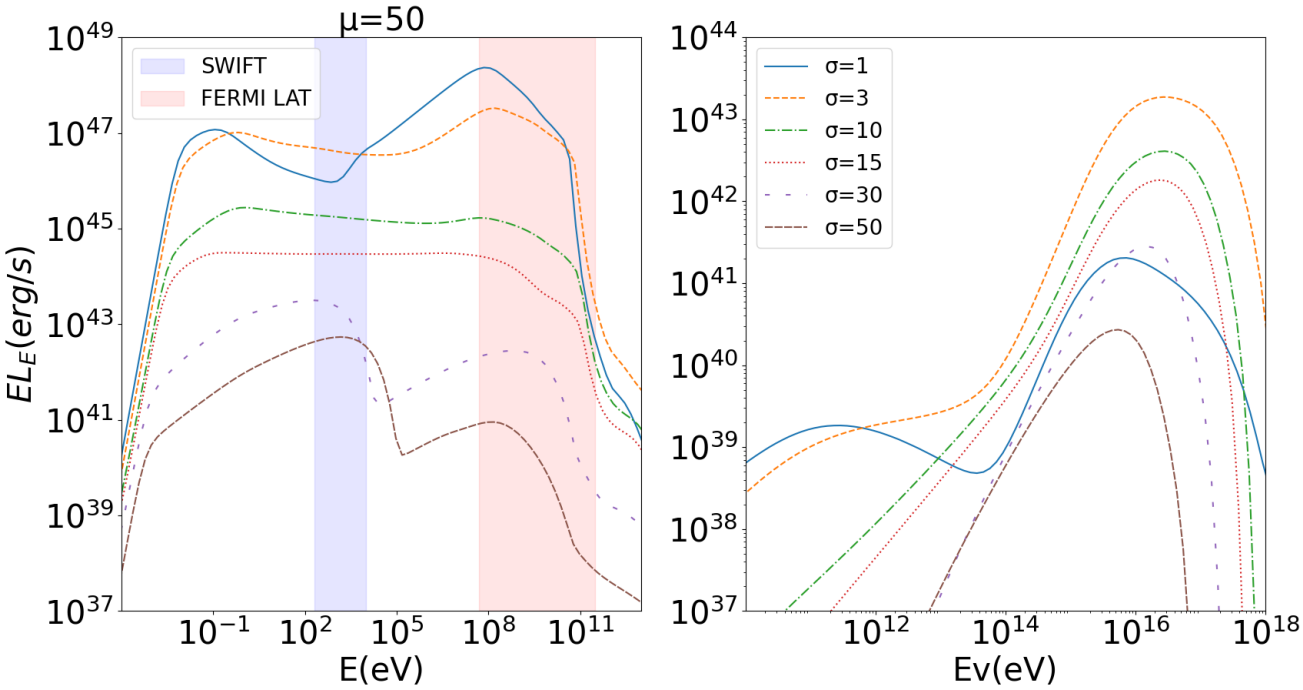

Figure 34: The photon (left panel) and neutrino spectra (right panel) in the case of $\mu = 50$ and different values of σ as indicated in the inset legend.

is attributed to SSC. This is because the internal synchrotron energy density is higher than the corresponding one of the BLR, bearing in mind eq.(3.9).

Additionally, in the cases of $\sigma = 1$ and $\sigma = 3$, moving to higher μ we see that the synchrotron hump of $\sigma = 3$ overcomes the corresponding one of $\sigma = 1$. This is again due to Doppler boosting, because $\delta(\sigma = 3) < \delta(\sigma = 1)$ in the $\mu = 50$ case, but $\delta(\sigma = 3) > \delta(\sigma = 1)$ in the $\mu = 90$ case.

Moving on to neutrinos, we can see more evidently in the cases of $\sigma = 1$ and $\sigma = 3$ that there are 2 bumps. Both are attributed to neutrinos produced from pγ interactions. The lower bump in the cases, where $\sigma \leq 15$ is attributed to proton interactions with synchrotron photons, while the higher one is attributed to interactions with BLR photons. In the case where $\sigma \geq 15$, we see that there is only one bump and the lower energy one disappears. This can be explained by the inspection of Figs.(30 and 31).

Comparing pγ interactions in the cases of $(\sigma, \mu) = (1, 70)$ and $(\sigma, \mu) = (50, 70)$, we see that in the former case one would expect a lower energy bump in the neutrino spectra, since interactions with synchrotron photons are the only process happening until $\gamma'_p \approx 10^6$. Then, the threshold for BLR interactions is satisfied, and immediately this process becomes dominant, which will lead to the high energy hump in the neutrino spectra. On the other hand, in the case of high magnetization, we see that proton interactions with synchrotron photons is a process that remains dominant for any proton energy selected. At $\gamma'_p = 10^4$, we observe a break in the efficiency because of the change of the target photons. At lower energies, interactions occur

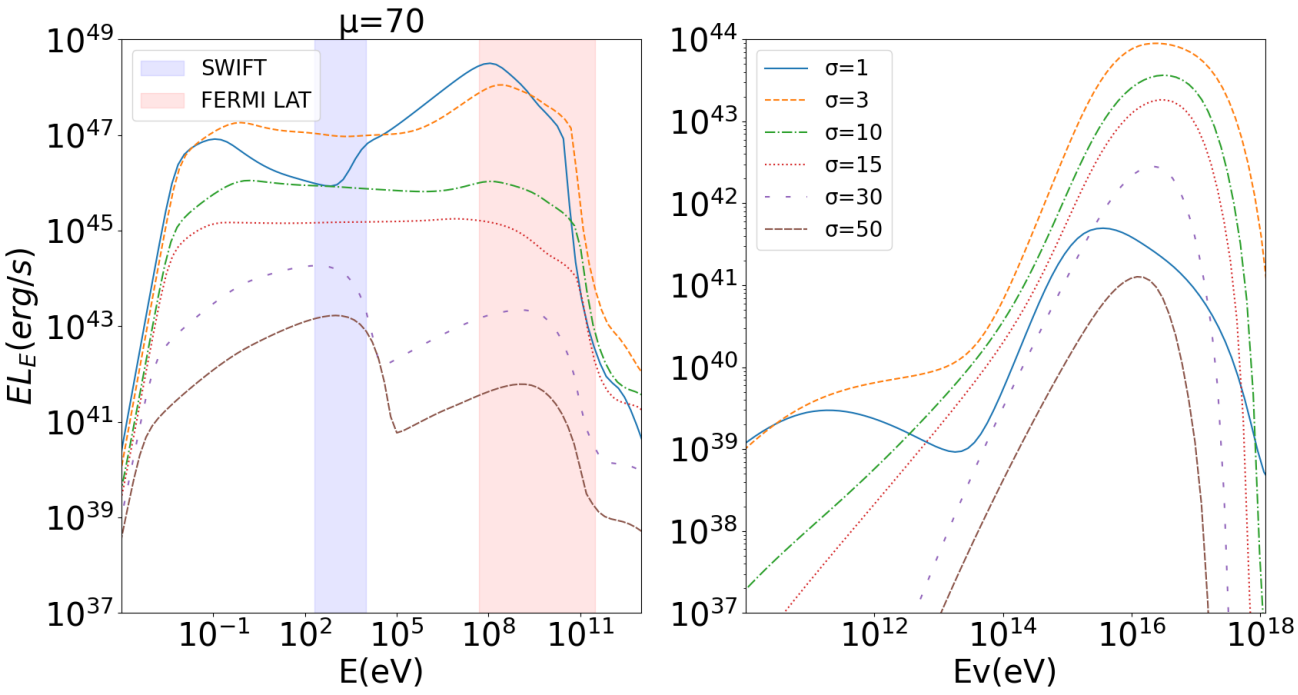

Figure 35: The photon (left panel) and neutrino spectra (right panel) in the case of $\mu = 70$ and different values of σ as indicated in the inset legend.

with ICS photons, while in higher energies occur with synchrotron photons. This break is not observed in the neutrino spectra because it takes place at $\approx 10^{10} - 10^{11}$eV, where the neutrino luminosity is negligible and not shown in Figs.(34),(35) and (36).

Furthermore, a major difference between the photon and neutrino spectra is that in the case of neutrinos, the more luminous case does not correlate with the magnetization, as opposed to the photon spectra. This is because we need to take into account the threshold where the interactions take place and the proton rate from this threshold and above (see Appendix C).

Coming back to our SED results, we can also notice the shape of the photon spectra, regarding magnetization. In order to reach to some conclusions for the slope and the breaks that are observed, by the emission of electrons, we present (Fig.(36)) the steady state electron distributions multiplied by γ'^{p}, for all cases of σ examined. The shape of the emitting particle distribution is associated with the minimum and the maximum energy of the injected electrons and their relation with the cooling energy, with Lorentz factor $\gamma_{c,e}$ which refers to those electrons that can cool in one dynamical timescale. Particles with Lorentz factors greater than γ_c radiatively cool and, as a result, the slope of their distribution changes shape. More specifically, the electron distribution $N(\gamma_e)$ can be described as:

$$\mathrm{N}(\gamma') \propto \begin{cases} \gamma'^{-2}, & \gamma'_{\mathrm{c}} < \gamma' < \gamma'_{\mathrm{min}} \\ \gamma'^{-p-1}, & \gamma' > \gamma'_{\mathrm{min}} \end{cases} \tag{4.2}$$

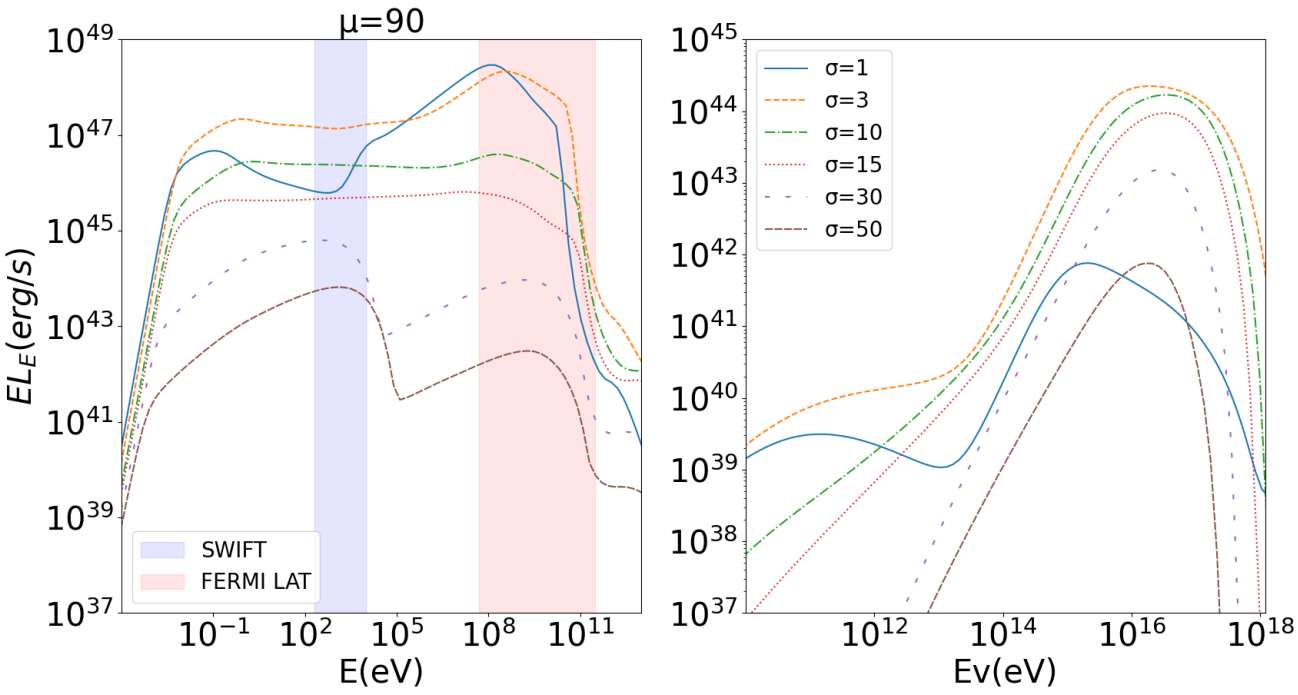

Figure 36: The photon (left panel) and neutrino spectra (right panel) in the case of $\mu = 90$ and different values of σ as indicated in the inset legend.

in the fast cooling regime, meaning when $\gamma'_{\rm min} \geq \gamma'_c$, or

$$N(\gamma') \propto \begin{cases} \gamma'^{-p}, & \gamma'_{\rm min} < \gamma' < \gamma'_{\rm c} \\ \gamma'^{-p-1}, & \gamma' > \gamma'_{\rm c} \end{cases} \tag{4.3}$$

which applies for the slow cooling regime ($\gamma'_c \geq \gamma'_{\rm min}$).

Observing Fig.(37), we can understand that all σ cases belong in the fast cooling regime, since we observe a break at $\gamma'_{\rm min}$ (for the values of the code parameters see Tables 3, 4, 5), and the slopes modify according to the relations described above. The observed SED in this regime follows:

$$L_\nu \propto \begin{cases} \nu^{5/2}, & \nu < \nu_{\rm ssa}, \\ \nu^{-1/2}, & \nu_{\rm ssa} < \nu < \nu_{\rm min}, \\ \nu^{-p/2}, & \nu > \nu_{\rm min}, \end{cases} \tag{4.4}$$

We should mention that eq.(4.4) is written like this, because γ'_c takes such low values, as calculated in Appendix (D), that $\nu_{ssa} \geq \nu_c$. Regarding the SEDs (Figs. (34),(35) and (36), the value of the slopes found in these results are similar with the ones in eq.(4.4), in all cases a break at $\nu_{\rm min}$ is observed. As a result, observing the cases of $\sigma = 10, 15$, there is produced an almost flat spectra, meaning that the slope above the break is close to zero. We, also, need to mention some information about the spectra with $\sigma = 30, 50$. In these cases, while it seems that there is not a break, in reality it is just not easy to be recognized. This happens due to the slight change of the slope. More specifically, in $\sigma = 30$ the break occurs at about ~ 0.65 eV, where the slope changes from ~ 0.5 to ~ 0.25. In $\sigma = 30$, we observe a break at ~ 0.4 eV and the slope changes

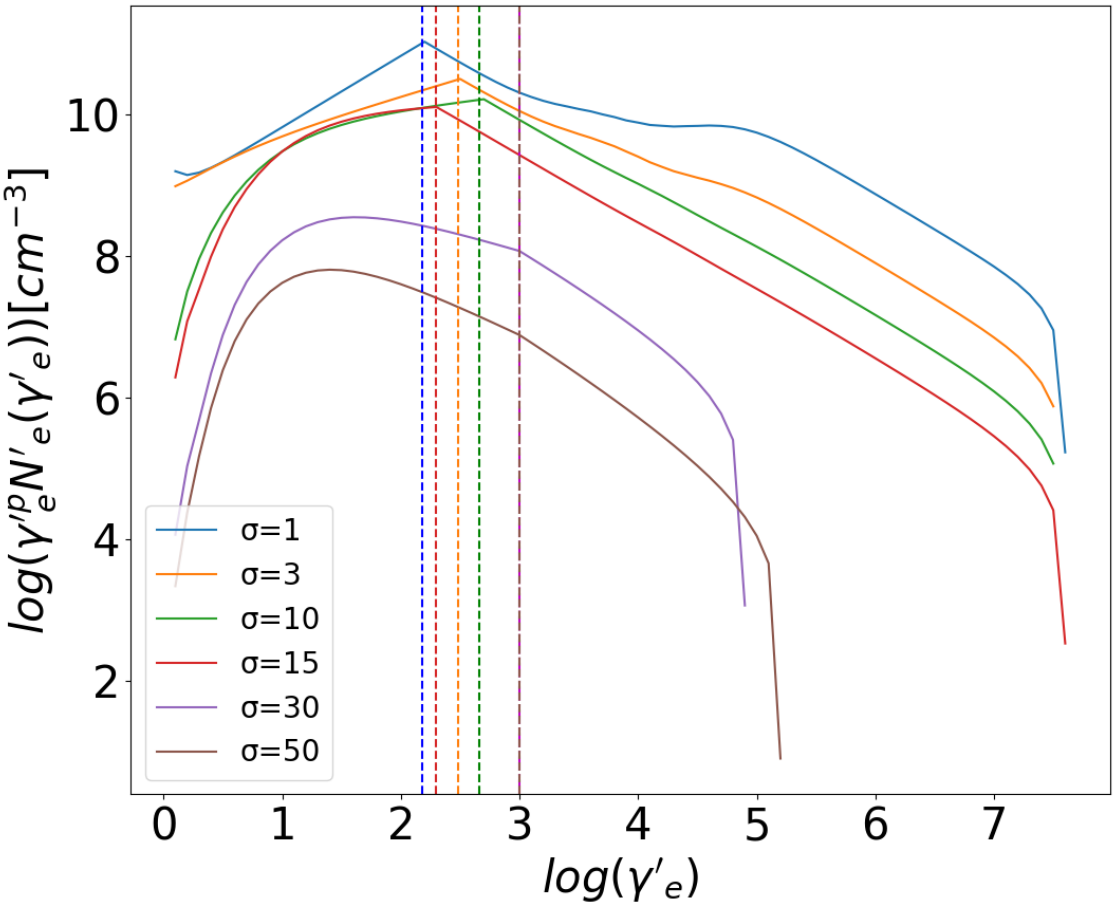

Figure 37: Steady state electron distributions multiplied by γ'^{p}, for each case of σ and for $\mu = 70$. The dashed lines correspond to the minimum electron Lorentz factor for each distribution.

from from ~ 0.5 to ~ 0.4. Such changes in the value of the slope, are difficult to notice just by looking Figs. (34),(35) and (36).

In FSRQs, the slope breaks due to radiative cooling, mainly due to inverse compton scattering with external photons (BLR). In the cases of $\sigma = 10, 15$, losses due to ICS and synchrotron cooling become comparable, while for high magnetizations, synchrotron cooling is dominant. Lastly, we need to consider the case where scatterings in the K-N regime may have an impact to the synchrotron and ICS bump, leading to a slight steepening of the slope. This happens at a frequency that corresponds to radiating electrons with $\gamma'_{KN} = \frac{m_e c^2}{\Gamma \epsilon_{BLR}}$. However, as found in in Appendix (D), this frequency corresponds to the high energy tail of both mechanisms in the SED and therefore its impact is negligible.

Next, we will first calculate how the electron luminosity is written as a function of Γ and σ, and then we will compare this expression with the observed integrated γ-ray luminosity to reach some conclusions about the strength of cooling, regarding each case we studied.

First, following eq.(3.24) electron luminosity can be written as:

$$L'_{\rm e} = f_{\rm rec}\frac{2L_{\rm B}}{3\beta\Gamma^2} = \frac{2f_{rec}\sigma L_j}{3(1+\sigma)\beta\Gamma^2} = \frac{2f_{rec}\eta_j {\Gamma_o}^{-3}\sigma\Gamma}{3(1+\sigma)\beta\eta_d} \Rightarrow L'_{\rm e} = A\frac{\Gamma\sigma}{1+\sigma} \tag{4.5}$$

where $A = \frac{2f_{rec}\eta_j {\Gamma_o}^{-3}}{3\beta\eta_d}$

In the observer's frame, it will be:

$$L_{\rm e,obs} = \delta^4 L'_{\rm e} \tag{4.6}$$

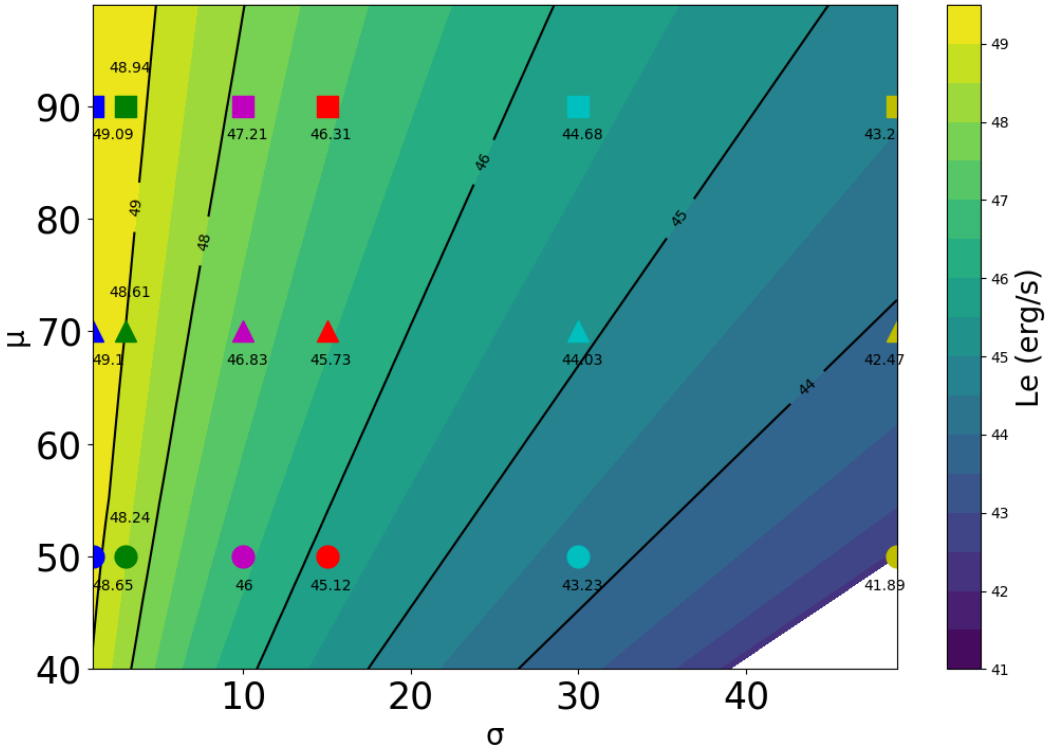

Figure 38: μ - σ plot with color zones where each color represents different values of L_e. Blue, green, purple, red, cyan, yellow points represents the cases of $\sigma = 1, 3, 10, 15, 30, 50$, respectively, while the circles, triangles and squares stand for the cases of $\mu = 50, 70, 90$ respectively. The values below each point stand for the integrated γ-ray luminosity.

Taking this expression into account, we present Fig.(38) where all the cases of μ and σ that we studied are presented. Under each point that represents a (μ, σ) case, there is noted below a value that corresponds to the integrated γ-ray luminosity. Different color zones correspond to different values of $L_{\rm e,obs}$. One can observe that for the cases of $\sigma = 1$ and $\sigma = 3$, electron and γ-ray luminosity are almost equal, meaning that electrons radiate almost all of their energy through ICS, which is why cooling is significant in these cases. Moving to higher magnetizations, the electron luminosity starts getting more greater than γ-ray luminosity, exceeding it almost by one order of magnitude in the mildly magnetized cases ($\sigma = 10, 15$) and by almost two orders

in the highly magnetized cases ($\sigma = 30, 50$), which means that particles give off their energy less and less efficient, as magnetization gets higher.

We next discuss some additional diagnostic diagrams. In Fig.(39 and (40) we present two plots regarding the Compton Dominance (CD), meaning the ratio of peak luminosities of ICS to synchrotron as a function of the synchrotron peak energy and the integrated photon luminosity, for energies above 10 MeV. Generally, we observe that the compton dominance is high in the cases of low magnetization as expected, because as we already mentioned the BLR photon field appears more luminous to the FSRQs objects leading to the dominance of the ICS process over the SSC process. For the same reason, L_γ takes higher values for low σ , and also due to Doppler boosting. Regarding the synchrotron peak, our results show similarities to observations, where FSRQ objects appear to have peak synchrotron frequency lower than 10^{15}Hz, while highly magnetized objects tend to have higher synchrotron peak energies ([25],[24]), which is supported by the blazar sequence. However, we need to state that two of the examined cases, where $\sigma = 10$ and $\sigma = 15$, are problematic due to the ”flat” shape of their spectra, which results to uncertainty of the selection of the peak synchrotron energy. Furthermore, we should also address the issue of the empty upper right region in Fig.(39. As discussed in Padovani's critical review of the blazar sequence (P. Padovani (2007) [54]), the absence of high power - high synchrotron peak blazars is worth of studying. The search of these objects led to finding FSRQs in the HBL range, however these sources were not characterized by high power. A possible explanation to this issue is that non-thermal jet emission is dominant over thermal, which imposes difficulties in determining the redshift of these sources.

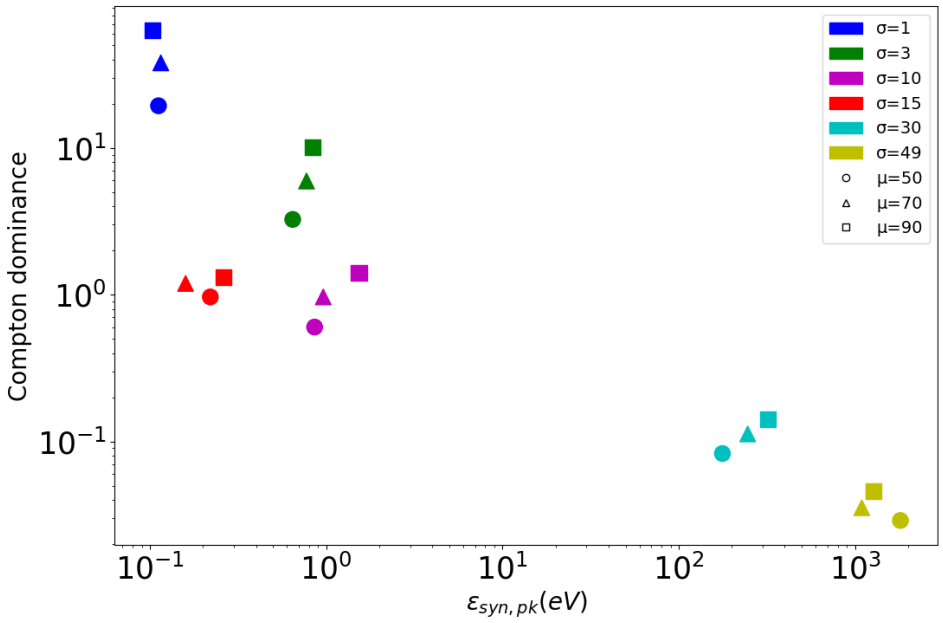

Figure 39: Compton dominance plotted against the synchrotron peak energy for all cases studied.

Additionally, we present Fig.(41,42 and 43) where we have computed the ratio of integrated neutrino luminosity to the integrated γ-ray luminosity for energies above 10MeV. This quantity encloses all the information on the optical depth for photopion interactions and the luminosity of particles. So, this ratio is plotted as a function of the γ-ray luminosity and is shown that as

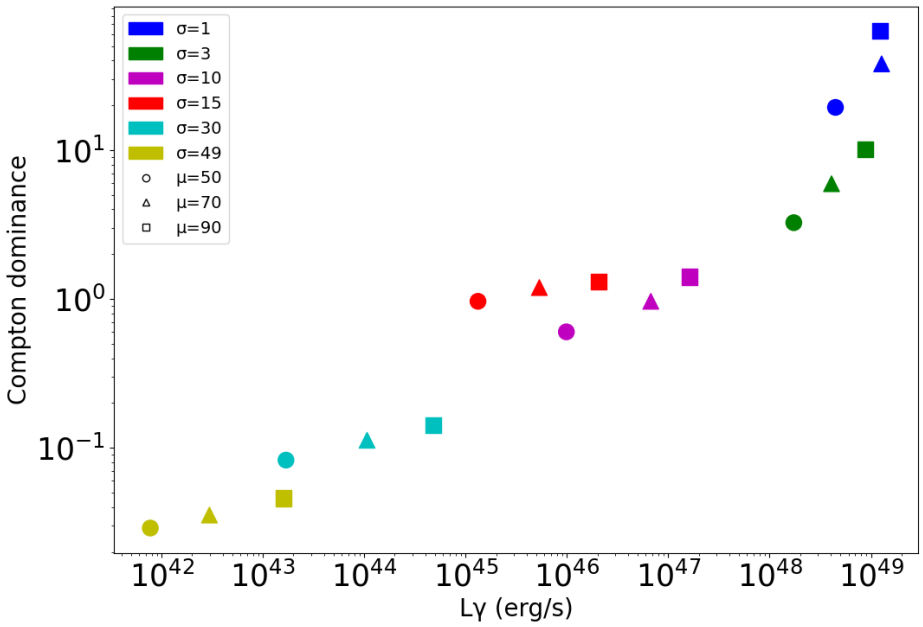

Figure 40: Compton dominance plotted against the photon luminosity for all cases studied, where L_γ is integrated for energies above 10 MeV.

magnetization takes higher values, the ratio is also increasing. In the extreme case of $\sigma = 50$, this ratio is getting close to unity, while L_γ takes low values. The opposite trend is shown when magnetization decreases. This result is mainly attributed to how much more brighter FSRQs are, and less to the variation of L_ν, as σ decreases. Comparing our results with earlier studies ([58],[59],[56]), we observe a similar trend. More specifically, in the work of Petropoulou et al. (2020) [59], where several leptohadronic models are taken into account for modeling the emission of the blazar 3HSP J095507.9+355101, the ratio $Y_{\nu\gamma}$ is calculated. These authors also included results from earlier works like Petropoulou et al. (2015) [58], where six BL Lac objects are examined, and Keivani et al. (2018) [39], which sets maximum values of $Y_{\nu\gamma}$, obtained for TXS 0506+056. In these results, although the models are different to ours, there are assumed two cases of proton and electron injection power law indices; $s = 1 - 1.3$ and $s = 2$. In the former case, which is related to our assumed BL Lac particle distribution, $Y_{\nu\gamma}$ is close to unity, while in the case of a higher power law index, the ratio is slightly decreased. Generally, there is observed a similar trend as in our study, since in these works $Y_{\nu\gamma}$ is decreased with L_γ, as well. Furthermore, in the work of Palladino et al. (2019) [56], there are also obtained similar results, although in their study, they assumed a scenario where the ratio scales with the luminosity. For low-luminosity sources, they found a ratio of about 0.15, where for high luminosity sources the ratio should be lower than 5×10^{-3}. So, once again their assumed anti-correlation between L_γ and $Y_{\nu\gamma}$ is hereby covered.

In Fig.(41), there is plotted the ratio $L_{\nu+\bar{\nu}}/L_\gamma$ as a function of the energy of peak neutrino luminosity. There is not a big difference in the energy peak, although it should be mentioned that for the cases of $\sigma \leq 15$, where the neutrino peak is attributed to proton interactions with BLR photons, we expect the peak to be near the threshold, due to the steepness of the power-law of proton distribution. In the case of highly magnetized objects $\sigma = 30, 50$, the energy is

carried by the protons with maximum energy, with Lorentz factor close to 10^8. This means that the neutrino peak energy is approximated by: $\epsilon'_{\nu,pk} \approx \frac{1}{20}\gamma'_{\max} m_p c^2$ This is why, in the jet fluid frame all cases of μ, for $\sigma = 30, 50$ have similar peak neutrino energy. In the observer's frame, as shown in Fig. (41), there is a bigger variation due to the multiplication of the doppler factor, δ.

Furthermore, in Fig. 42 is also presented $L_{\nu+\bar{\nu}}/L_\gamma$ as a function of σ. As already mentioned, while magnetization is increased, the ratio is also increased, mostly due to the relation of L_γ and σ in BL Lac objects. We, also, made a fit for this result, which is expressed by:

$$L_{\nu+\bar{\nu}}/L_\gamma = 2.5 \times 10^{-6}\sigma^3 \quad \text{for} \quad \sigma \geq 1 \tag{4.7}$$

Lastly,in Fig.(44), jet luminosity is getting higher for low magnetizations, which is expected from eq.3.15, since L_j is proportional to Γ^3. For comparison reasons, a horizontal line which stands for the Eddington luminosity is also plotted in the same figure. In most of the cases, we see that $L_j \leq L_{Edd}$, which is a result that shows that these sources are energetically beneficial. Only in 4 cases the jet luminosity overcomes the Eddington luminosity, which is a result of eq.(3.15), where we can calculate that:

$$L_j \geq L_{Edd} \Rightarrow \dot{m} \geq 0.11 \Rightarrow \Gamma \geq 19.2 \tag{4.8}$$

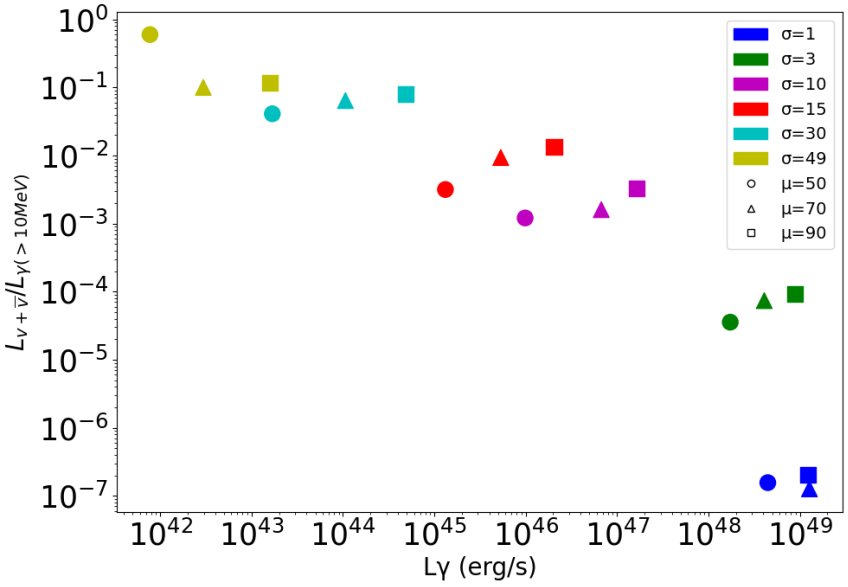

Figure 41: Ratio of neutrino luminosity to photon luminosity plotted against the photon luminosity for all cases studied. Blue, orange and green lines connect the points of $\mu = 50$,$\mu = 70$ and $\mu = 90$, respectively.

4.3 Conclusions

In this study, we examined the multi-messenger emission of blazar jets, assuming that the particles that were injected were accelerated by the magnetic reconnection process. Typically,

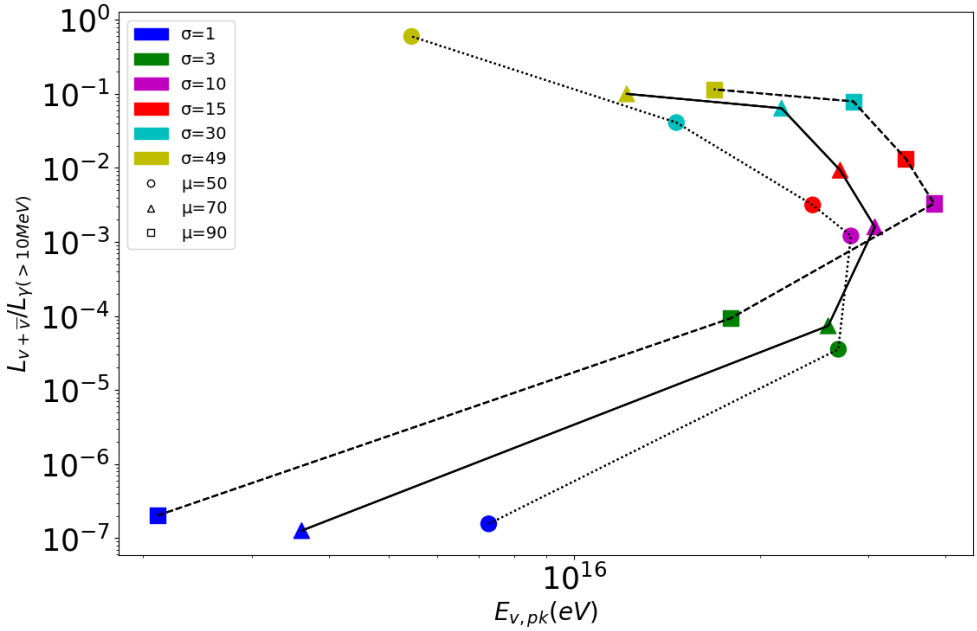

Figure 42: Ratio of neutrino luminosity to photon luminosity plotted against the peak neutrino energy for all cases studied.

we classified objects with low magnetization as FSRQs, and the objects with high magnetization as BL Lacs. According to our results, FSRQs are the most luminous blazars, mainly due to Doppler boosting. They are Compton dominated. Moving from FSRQs to BL Lacs, the compton dominance decreases, while synchrotron peak shifts to higher frequencies.

Besides photons, there is also production of neutrinos, since we study the case of proton-electron plasma. The injection of protons will lead to photohadronic interactions and as a result neutrinos will be produced, due to interactions with BLR or internal (synchrotron photons). The former case is significant when the magnetization takes low values, while the latter case is expected when magnetization is high. Also, according to the neutrino spectra, the most luminous case is dependent on the luminosity calculated from the threshold energy of the interaction, as found in eq.(C.6).

Moreover, we presented some diagnostic diagrams. In one of them we displayed the jet luminosity, plotted against the photon luminosity integrated above energies of 10 MeV. The trend between this quantities, is that when one is increased, so does the other. However, the most important observation is the relation between L_j and L_{Edd}. In most cases, we reach to a result that is not too energetically demanding, since $L_j \leq L_{Edd}$, although in some cases where the accretion rate is high ($\dot{m} \geq 10\%$), L_j is significantly increased and overcomes L_{Edd}.

Finally, we examined the ratio of $L_{\nu+\bar{\nu}}/L_\gamma$ for each case. We showed that blazars with high magnetization have a higher ratio of $L_{\nu+\bar{\nu}}/L_\gamma$ and in extreme cases it can reach a value, very close to 1. On the other hand, low magnetized blazars have shown the opposite trend, meaning really low values of ratios (down to 10^{-7}) and high γ ray luminosity. These results are mainly explained due to how much more brighter low magnetization blazars are, and less to the

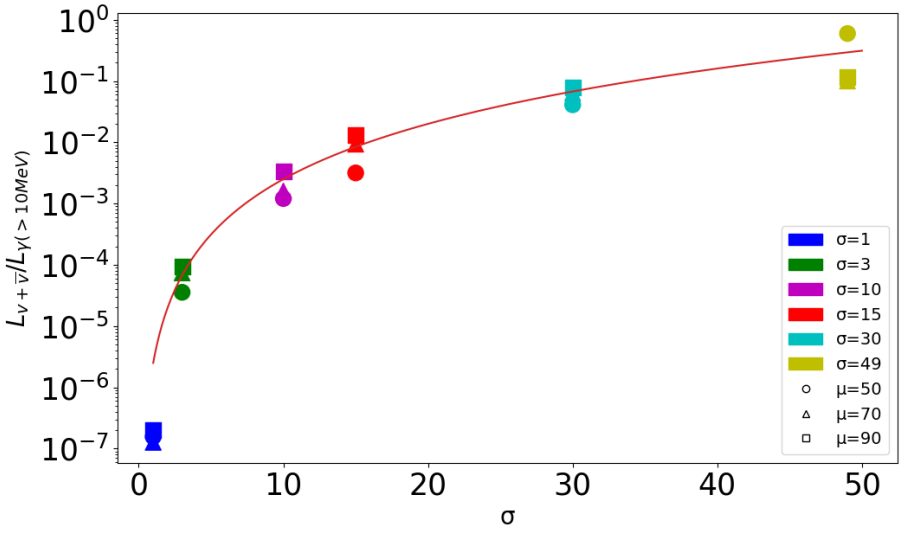

Figure 43: Ratio of neutrino luminosity to photon luminosity plotted against the magnetization for all cases studied.

variation of $L_{\nu+\bar{\nu}}$, and are supported by earlier independent studies, as well.

To conclude, blazar jets are sites where neutrino production is expected. Setting a simple model, where all physical quantities are written as a function of two main parameters, we can produce results that are supported from literature.

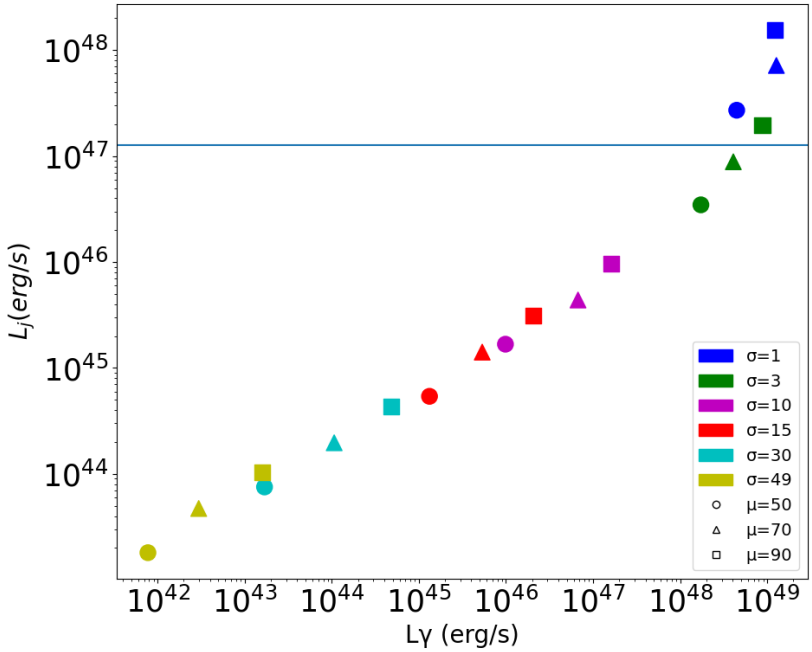

Figure 44: Jet luminosity plotted against the integrated photon luminosity for all cases studied, where L_γ is integrated for energies above 10 MeV. The horizontal line corresponds to the Eddington luminosity for an assumed black hole mass of $10^9 M_\odot$

A. Doppler boosting

Jets from blazars radiate in a small angle with respect to the observer, which leads to the emission into very high energies and the appearance of relativistic effect, as well.

The relativistic motion of the source, consequently leads to the doppler boosting of some emission related values. This is because a stationary observer measures differently some physical values, as opposed to an observer moving with the same velocity with the blazar jet. The difference between the two can be expressed by a factor known as Doppler factor:

$$\delta = \frac{1}{\Gamma(1 - \beta cos\theta)} \tag{A.1}$$

If $\Gamma \gg$ and $\theta \ll$, then by Taylor approximation on $cos\theta$ we are lead to:

$$\delta = \frac{2\Gamma}{(1 + \Gamma^2\theta^2)} \tag{A.2}$$

Analyzing this result for some extreme cases, we find the following:

$$\begin{aligned} \delta &= 2\Gamma \quad , \theta \to 0 \\ \delta &\simeq \Gamma \quad , \theta \leq \frac{1}{\Gamma} \\ \delta &\simeq \frac{1}{\Gamma} \quad , \theta \geq 1 \end{aligned} \tag{A.3}$$

So, in the case of blazar jets, we can approximate the Doppler factor to be proportional to the bulk Lorentz factor of the jet.

Some transformations of useful quantities between the two frames are presented below:

- Frequency $\nu = \delta\nu'$
- Time $t = t'/\delta$
- Differential flux $F_\nu = \delta^3 F'_{\nu'}$
- Luminosity $L = \delta^4 L'$

where primed quantities correspond to the jet frame.

B. Threshold energy of an interaction

As mentioned in ch.2, hadronic interactions lead to the production of secondary particles, meaning that a minimum energy is needed for the interaction happen, known as threshold energy. In order to compute this quantity, let us assume, for all the processes we will describe, that we have two interacting particles; a and b, and their products; c,d, etc. In the laboratory frame, the momentum four-vector will be: $\vec{P}^{\mu}_{a,b} = (\varepsilon_{a,b}, \vec{p}_{a,b})$ where we set $\varepsilon_i \equiv E_i/c = m_i\gamma_i c$

So, the total momentum four-vector is:

$$\vec{P}^{\mu} = (\varepsilon_a + \varepsilon_b, \vec{p}_a + \vec{p}_b) \tag{B.1}$$

Now, in the center of momentum frame of particles a and b, where the total momentum three-vector is zero, the total four-momentum is:

$$\vec{P}^{\mu'} = (\varepsilon'_a + \varepsilon'_b, 0) \tag{B.2}$$

Considering that the squared momentum four-vector is invariant, we get:

$$\begin{aligned} & P^{\mu}P_{\mu} = P^{\mu'}P_{\mu'} \\ & \Rightarrow (\varepsilon'_a + \varepsilon'_b)^2 \equiv \varepsilon'^2 = (\varepsilon_a + \varepsilon_b)^2 - (\overrightarrow{p_a} + \overrightarrow{p_b})^2 \\ & \Rightarrow \varepsilon'^2 = \varepsilon_a^2 + \varepsilon_b^2 + 2\varepsilon_a\varepsilon_b - p_a^2 - p_b^2 - 2\overrightarrow{p_a}\cdot\overrightarrow{p_b} \\ & \Rightarrow \varepsilon'^2 = m_a^2c^2 + m_b^2c^2 + 2\varepsilon_a\varepsilon_b - 2\overrightarrow{p_a}\cdot\overrightarrow{p_b} \end{aligned} \tag{B.3}$$

Since, the threshold energy is defined as the minimum energy of the incoming particles to produce the rest mass energy of the produced particles, then:

$$\varepsilon'_{th} = \frac{m_ac^2 + 4m_bc^2 + \Delta m \cdot c^2}{c} \tag{B.4}$$

where $\Delta m = (m_c + m_d + ...) - (m_a + m_b)$

So, from eq.(B.3) and (B.4) and demanding that $\epsilon' \geq \epsilon'_{th}$, one can obtain the following result:

$$\varepsilon_a\varepsilon_b - \overrightarrow{p_a}\overrightarrow{p_b} \geq m_am_bc^2 + \Delta mc^2\left(m_a + m_b + \frac{\Delta m}{2}\right) \tag{B.5}$$

For interactions, such as p-p, where the interacting particles have mass, one can estimate the threshold proton energy, by setting $m_a = m_b = m_p$ and $\Delta m = m_{\pi^o}$ in eq.(B.5):

$$\gamma_a\gamma_b - \sqrt{(\gamma_a^2 - 1)(\gamma_b^2 - 1)}\cos\theta \geqslant 1 + \Delta m\left(\frac{1}{m_b} + \frac{1}{m_a} + \frac{\Delta m}{2m_am_b}\right) \tag{B.6}$$

In the case of interactions where one of the particles is a photon, such as photopion and Bethe-Heitler, we set using $m_b = 0$ and $p_b = \varepsilon_b$ in eq.(B.5) and we obtain:

$$m_a\gamma_ac\varepsilon_b - m_a\gamma_a\beta_ac\varepsilon_b\cos\theta \geq \Delta mc^2\left(m_a + \frac{\Delta m}{2}\right) \tag{B.7}$$

which eventually leads to:

$$\varepsilon_b \left(\gamma_a - \sqrt{\gamma_a^2 - 1} \, \cos\theta \right) \geqslant \Delta m \, c \left(1 + \frac{\Delta m}{2 m_a} \right) \tag{B.8}$$

C. Analytical estimation of the neutrino luminosity

We can estimate in a semi-analytical manner the differential neutrino luminosity as: $\varepsilon_\nu L_{\varepsilon_\nu} \approx \frac{3}{8} f_{p\gamma}\ \varepsilon_p L_{\varepsilon_p}$.

First, we will calculate the efficiency f_{BLR} in an analytical manner, approximating the BLR radiation field as a δ function:

$$\begin{aligned} & t'^{-1}_{p\gamma,BLR}(\gamma'_p) = \frac{cn'_o\sigma_0 k_0}{2\gamma'^2_p} \int_0^\infty \frac{d\varepsilon'}{\varepsilon'^2} \delta\left(\varepsilon' - \varepsilon'_{BLR}\right) \int_0^{2\gamma'_p\varepsilon'} d\bar{\varepsilon} \cdot \bar{\varepsilon} H\left(\bar{\varepsilon} - \bar{\varepsilon}_{th}\right) \\ & = \frac{cn'_o\sigma_o k_o}{4\gamma'^2_p} \int_0^\infty \frac{d\varepsilon'}{\varepsilon'^2} \delta\left(\varepsilon' - \varepsilon'_{BLR}\right) \left[4\gamma'^2_p\varepsilon'^2 - \bar{\varepsilon}_{th}{}^2\right] \\ & = cn'_o\sigma_o k_o \left[1 - \left(\frac{\bar{\varepsilon}_{th}}{\varepsilon'_{BLR}}\right)^2 \frac{1}{4\gamma'^2_p}\right] \end{aligned} \tag{C.1}$$

where n'_o is the photon number density of BLR and $\sigma_o k_o \approx 70\mu$b is the effective cross section for pγ interactions.

$$f_{p\gamma} = \frac{R'_b}{c} t'^{-1}_{p\gamma,BLR} \tag{C.2}$$

In the case where $\gamma'_p \gg 1$ one can write $f_{p\gamma}$ as:

$$f_{p\gamma} \approx R'_b n'_o \sigma_o k_o \propto \Gamma^{3/2} \tag{C.3}$$

The efficiency of proton-jet photons interaction, can be estimated from eq.(2.63). Using the two step approximation for the cross section (eq.(2.64)) and inelasticity (eq.(2.65)), we can compute the cooling timescale of the process by:

$$t'^{-1}_{p\gamma}\left(\gamma'_p\right) = c\sigma_o k_o \int_{\bar{\epsilon}_{thr}/2\gamma'_p}^\infty d\epsilon' n'_{ph}\left(\epsilon'\right) \left[1 - \left(\frac{\bar{\epsilon}_{thr}}{2\gamma'_p\epsilon'}\right)^2\right] \tag{C.4}$$

It is shown in fig.(45) that the efficiency of proton interactions with BLR and jet photons. The former is dominant in the cases of $\sigma = 1, 3$, while for $\sigma = 30, 50$ this is reversed. In the mildly magnetized cases of $\sigma = 10, 15$ the efficiency of the two types of interactions becomes comparable near the maximum of the proton energies considered, but f_{BLR} is still slightly higher than f_{jet}.

But in order to fully understand the dependence of the neutrino luminosity on σ, we need to check how the proton power, that is relevant for neutrino production, scales with σ.

From eq.(3.28), we can write the differential proton luminosity as:

$$\epsilon'_p L'_p(\epsilon'_p) = V' Q'_o E'^{-p+1}_p \tag{C.5}$$

where $V'Q'_o = \frac{L'_p}{Im_p c^{2(2-p)}}$ for $p \neq 2$

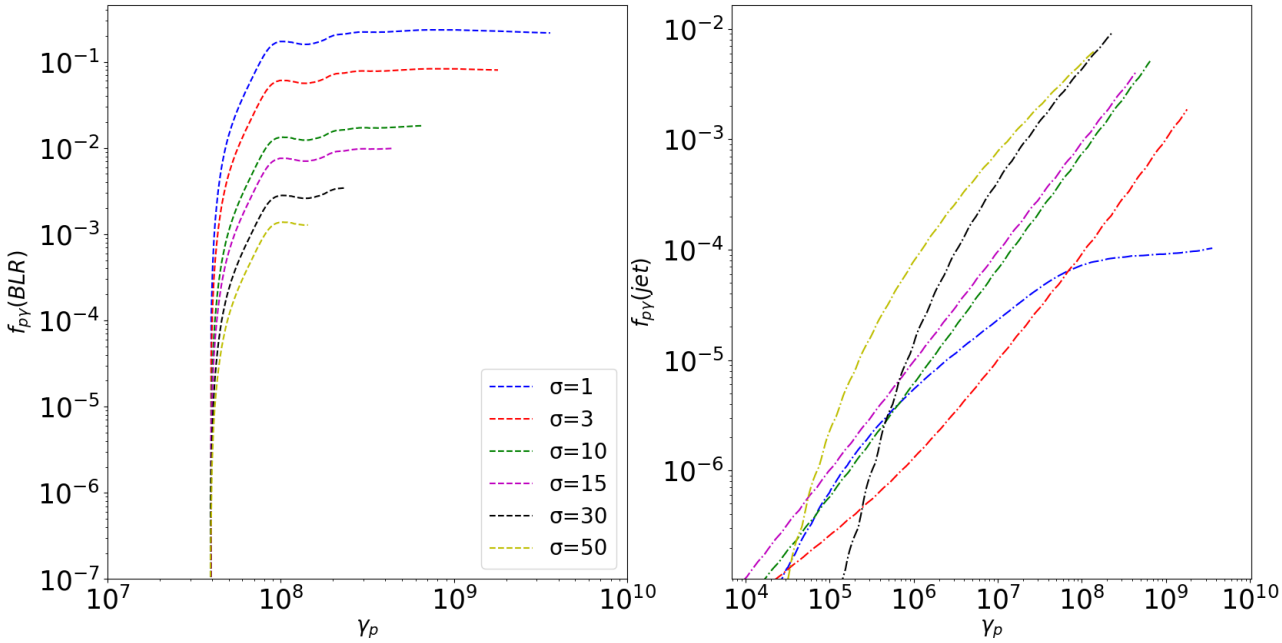

Figure 45: The efficiency of proton interactions with BLR photons (left panel) and with jet photons (right panel) in the cases of $\sigma = 1, 3, 10, 15, 30, 50$ represented with blue, red, green, purple, black and yellow lines, respectively.

In Fig.(46) we present the differential proton luminosity for interactions with both photon distributions, for all magnetization cases. For interactions with BLR, which correspond to energies above threshold (shown in the vertical line), we can notice that the luminosity is significantly higher when magnetization gets higher. Actually, we can make a calculation, regarding the threshold luminosity for proton interaction with BLR photons.

$$L'_{p,thr} = V' Q'_o m_p c^2 \int_{\gamma'_{thr}}^{\gamma'_{\max}} d\gamma' \gamma'^{-(p-1)} = \frac{2 f_{rec} L_B (2-p)}{3\beta\Gamma^2 ({\gamma'_{\max}}^{2-p} - {\gamma'_{\min}}^{2-p})} \frac{{\gamma'_{\max}}^{2-p} - {\gamma'_{thr}}^{2-p}}{2-p} \quad \text{(C.6)}$$

$$= L'_p \frac{{\gamma'_{\max}}^{2-p} - {\gamma'_{thr}}^{2-p}}{{\gamma'_{\max}}^{2-p} - {\gamma'_{\min}}^{2-p}}$$

where one can calculate γ'_{thr} as:

$$2\epsilon'_{BLR} \cdot \gamma'_p \geqslant 145\text{MeV} \overset{\varepsilon_{BLR}=2\text{eV}}{\Rightarrow} \gamma'_{p,th} = \frac{145\text{MeV}}{4\Gamma\text{eV}} \simeq \frac{3.6 \times 10^7}{\Gamma} \Rightarrow E'_{p,th} \simeq \frac{3 \times 10^{16}}{\Gamma} \text{ eV} \quad \text{(C.7)}$$

In the case of proton interactions with jet photons, the threshold condition is always satisfied, since even for the minimum energies of the proton distribution, interactions occur with ICS photons.

So, by calculating the efficiency and luminosity for both cases of pγ interaction, we can reproduce the neutrino spectra, as shown in Fig.(47) based on the expressions above. Here we

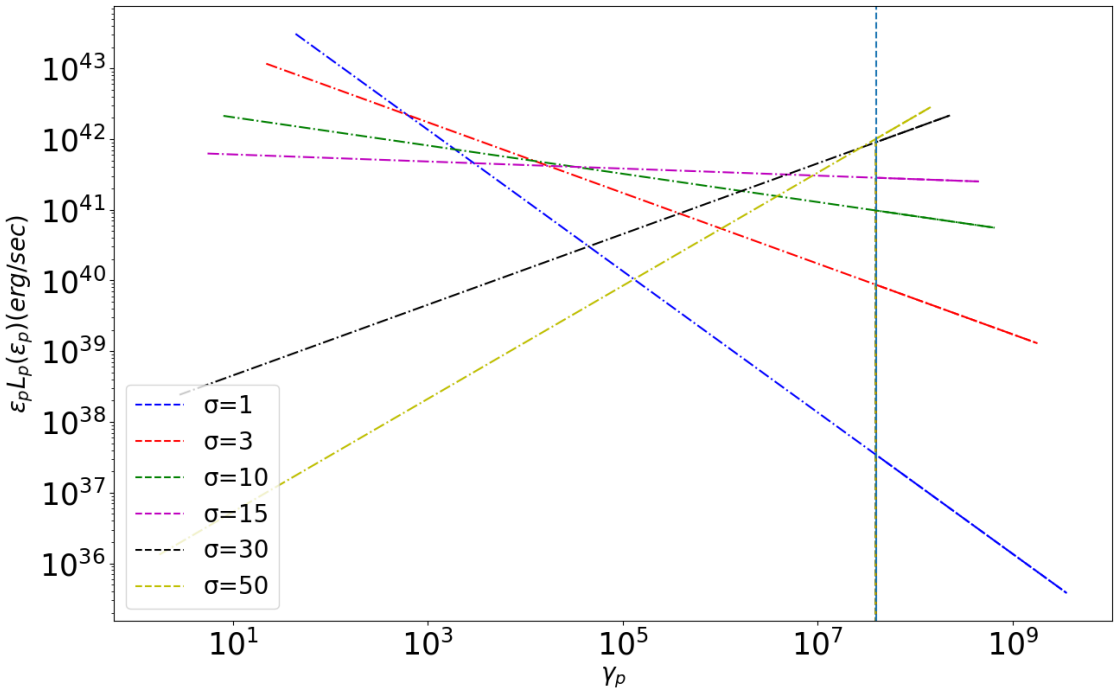

Figure 46: Proton differential luminosity in the cases of $\sigma = 1, 3, 10, 15, 30, 50$ represented with blue, red, green, purple, black and yellow lines, respectively. The vertical line corresponds to the threshold Lorentz factor for BLR interactions, calculated in the observer's frame.

see the behaviour that was demonstrated in the original SEDs. More specifically, the case of $\sigma = 3$ presents the most luminous peak, followed by $\sigma = 10$, $\sigma = 15$, $\sigma = 30$, $\sigma = 1$ and $\sigma = 50$. This behaviour differs from the photon spectra, but after our calculations, it is explained why this is the case. Besides the efficiency, we have to take into account the luminosity considered from the threshold of $p\gamma$ interactions with BLR, mainly in the low magnetization cases, and is the reason why the more luminous case in the neutrino spectra is not corresponding to $\sigma = 1$, in contrary to the photon spectra. Regarding the shape of the spectra, we have to mention that since our analytical calculations take into account only the maximum neutrino energy produced by the proton distribution, we can not account for the exponential cutoff tail like our numerical results, which explains why the spectra is abruptly cut in Fig.(47).

Furthermore, our calculations can also explain our results regarding the peak neutrino energy, shown in Fig.(42). As expected, in low magnetization cases ($\sigma = 1, 3$), the neutrino peak is attributed to protons near the threshold energy of BLR interactions, since lower energy particles carry the most energy. On the other hand, in high magnetization cases ($\sigma = 30, 50$), the neutrino peak is attributed to the highest energy protons of the distribution. In these cases, $\gamma'_p \approx 10^8$, so the neutrino peak can be calculated by: $\epsilon_{\nu,pk} \approx 0.05\delta\gamma'_p m_p c^2 \approx 5\delta$ PeV. In mildly magnetized cases ($\sigma = 10, 15$), as we can see from Fig.(47), the neutrino luminosity is mainly attributed to pγ interactions with BLR. However, in higher energies the contribution from the $p\gamma(jet)$ component, shifts the neutrino peak into higher energies, which explains the behaviour we see in Fig.(42).

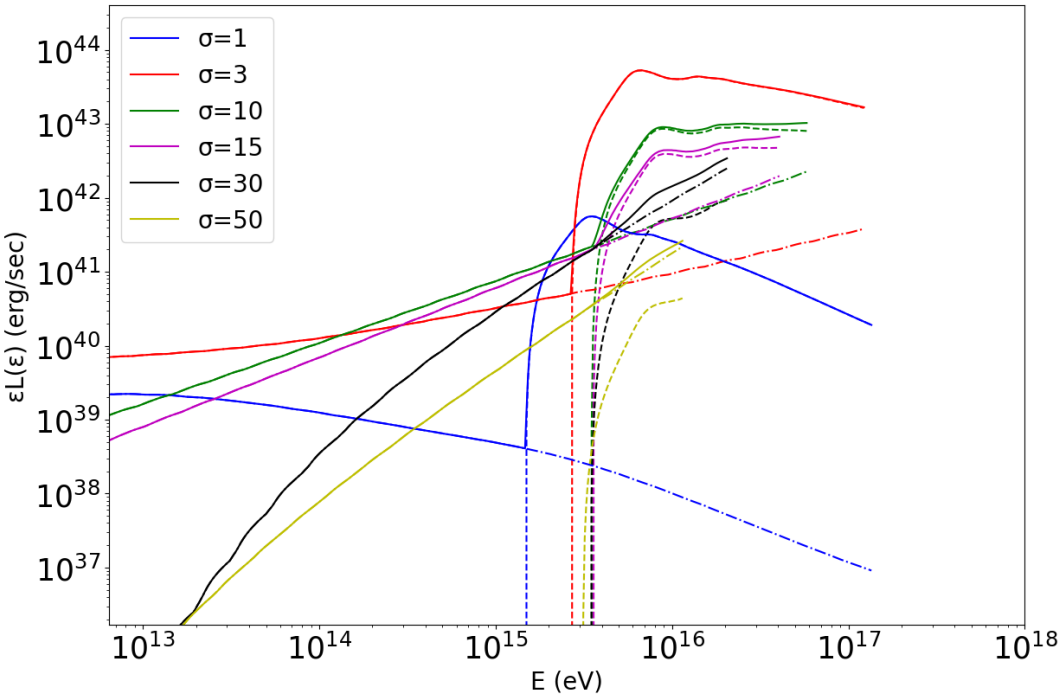

Figure 47: Neutrino luminosity in the cases of $\sigma = 1, 3, 10, 15, 30, 50$ represented with blue, red, green, purple, black and yellow lines, respectively. Dashdot and dashed lines show the contribution of photohadronic interactions with jet and BLR photons, respectively, while the solid lines stand for the sum of the two components.

D. Cooling parameters

The cooling frequency, is the typical frequency of radiation emitted by particles that are cooling on a given timescale (in this case, the dynamical timescale of the system). Electrons with $\gamma > \gamma_c$ are cooled significantly by time t, while lower energy electrons are not.

We can estimate in an analytical manner ${\gamma'}_c$ by equating the total energy losses through synchrotron and ICS with the dynamical timescale.

$$[t'_{dyn}]^{-1} = [t'_{syn}]^{-1} + [t'_{ICS}]^{-1} \Rightarrow [\frac{R'_b}{c}]^{-1} = [\frac{\gamma' m_e c^2}{\frac{4}{3}\sigma_T u'_B \beta_e \gamma'^2}]^{-1} + [\frac{\gamma' m_e c^2}{\frac{4}{3}\sigma_T u'_{BLR} \beta_e \gamma'^2}]^{-1}$$

$$\Rightarrow \gamma'_c = \frac{3\,\mathrm{m_e c^2}}{4\sigma_T \beta_e R'_b \left(u'_B + u'_{BLR}\right)}$$

$$\Rightarrow \gamma'_c = \frac{3 m_e c^2}{4\sigma_T R'_b \left[\frac{148.2}{8\pi}\frac{\sigma}{1+\sigma}\frac{1}{\beta} + \frac{4}{3}\Gamma^2 u_{BLR}\right]} \tag{D.1}$$

Following the above, we can write the cooling Lorentz factor as a function of μ and σ or as a function of μ and Γ:

$$\gamma'_c(\mu, \sigma) = \frac{228.09(1+\sigma)^{3/2}}{[41.72\sigma(\frac{\mu}{50})^{1/2} + \frac{629}{1+\sigma}(\frac{\mu}{50})^{3/2}]} \tag{D.2}$$

$$\gamma'_c(\mu, \Gamma) = \frac{228.09}{\left[5.9\Gamma^{1/2}\left(1 - \frac{\Gamma}{\mu}\right) + 3.54 \times 10^{-2}\Gamma^{5/2}\right]} \tag{D.3}$$

In order to calculate successfully γ'_c, we need to take into account the losses due to SSC. The cooling timescale of this mechanism can be calculated as:

$$\tau_{SSC} = \frac{E'_e}{P'_{SSC}} = \frac{\gamma' m_e c^2}{\frac{4}{3}\sigma_T u'_{Syn} \gamma'^2} \tag{D.4}$$

where we compute the energy density of synchrotron radiation as:

$$u'_{Syn} = \frac{L'_{syn}}{4\pi c {R'_b}^2} \tag{D.5}$$

where L'_{syn} can be calculated by our numerical results in Ch.4.

Our results for the cooling timescale for $\mu = 70$ are shown in Fig.(48). We see that the analytical approximation where SSC losses are not included is in good agreement with the results that correspond to our numerical calculations, for $\sigma \leq 15$. In the cases where $\sigma \geq 15$, SSC radiation becomes more important than external ICS radiation (see Table 2), which explains the difference between the numerical results and our analytical expression.

Moreover, in Ch.(4), we claimed that the SED spectra corresponds to the case of fast cooling regime. In order to confirm that, besides examining the slopes of the produced emission,

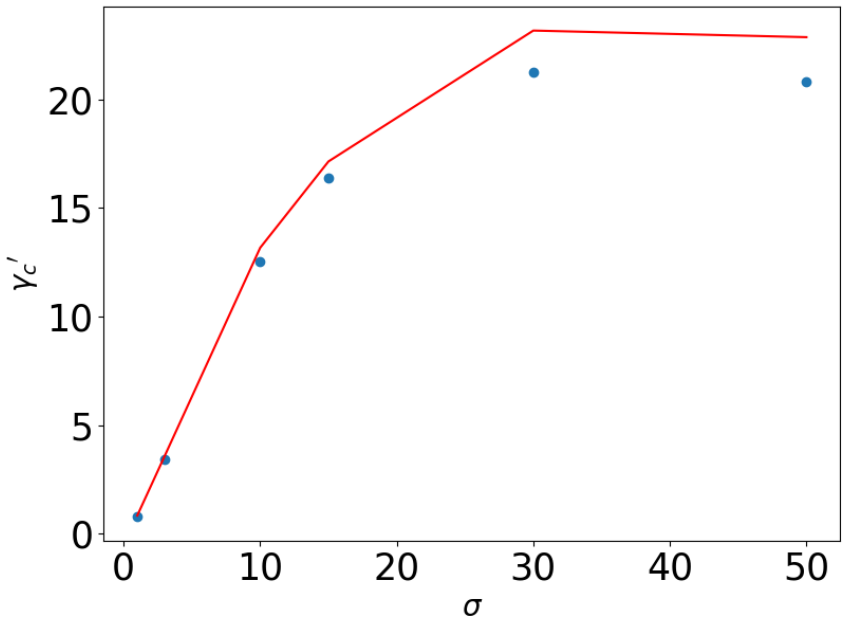

Figure 48: Cooling Lorentz factor plotted against σ. The line stands for for our analytical calculation where only synchrotron and external ICS losses are used, and the points correspond to the results including SSC losses.

as we did in Ch.(4), we can compare γ_c' with $\gamma_{\rm min}'$ of electrons, since we derived the results of γ_c'. As seen in Table 2, in all cases is $\gamma_{\rm min}' \geq \gamma_c'$, and therefore we have also computed the frequency, $\nu_{\rm min}'$, where the break occurs in the SEDs we presented. Furthermore, as we mentioned in Ch.(4), we consider the impact of scatterings in the K-N regime in the shape of synchrotron and ICS emission. To achieve this, we calculate:

$$\epsilon_{KN,Syn} = \Gamma {\gamma'_{KN}}^2 \frac{ehB'}{2\pi m_e c} \tag{D.6}$$

for the synchrotron component and:

$$\epsilon_{KN,ICS} = 4/3\ \Gamma^2 {\gamma'_{KN}}^2 \epsilon_{BLR} \tag{D.7}$$

for the ICS emission, where $\gamma'_{KN} = \frac{m_e c^2}{\Gamma \epsilon_{BLR}} = 2.5 \times 10^5 \Gamma^{-1}$.

These energies, however, correspond to the exponential tail of the synchrotron and ICS emission if we observe the SEDs, so the impact of K-N is not important in our results.

$\mu = 70$						
σ	1	3	10	15	30	48.9
$\frac{U_B}{U_{ext}}$	6.8×10^{-2}	0.4	3.81	8.5	37.1	146.05
$\frac{U_{syn}}{U_{ext}}$	6.2×10^{-5}	3.25×10^{-3}	6.4×10^{-2}	7.1×10^{-2}	1.97	8.77
γ'_c	0.8	3.43	12.53	16.4	21.25	20.8
$\gamma'_{\text{min},e}$	$10^{2.14}$	$10^{2.44}$	$10^{2.66}$	$10^{2.3}$	10^3	10^3
ϵ'_c (eV)	1.8×10^{-6}	3.66×10^{-5}	2.56×10^{-4}	3.64×10^{-4}	2.81×10^{-4}	1.68×10^{-4}
$\epsilon'_{\text{min},e}$ (eV)	5.33×10^{-2}	0.24	0.34	4.65×10^{-2}	0.62	0.39
$\epsilon'_{KN,syn}$ (eV)	1.75×10^5	1.94×10^5	1.02×10^5	7.3×10^4	3.89×10^4	2.43×10^4
$\epsilon'_{KN,ICS}$ (eV)	4.68×10^{12}	4.24×10^{12}	2.01×10^{12}	1.4×10^{12}	7.1×10^{11}	3.85×10^{11}

Table 2: Calculated parameters which are related to radiative cooling for $\mu = 70$.

Tables of code input parameters

We present all the parameters that are used as inputs for the code, regarding the 18 cases of (μ, σ) examined.

$\mu = 50$						
σ	1	3	10	15	30	48.9
Γ	25	12.5	4.55	3.13	1.61	1
$\dot{m}$	0.24	0.03	1.4×10^{-3}	4.7×10^{-4}	6.55×10^{-5}	1.57×10^{-5}
R'_b (cm)	2×10^{16}	1.41×10^{16}	8.51×10^{15}	7.06×10^{15}	5.07×10^{15}	4×10^{15}
B' (G)	8.6	10.6	11.75	12.1	13.52	47.93
p	3	2.5	2.2	2.05	1.5	1.2
$\gamma'_{min,e}$	$10^{2.14}$	$10^{2.44}$	$10^{2.66}$	$10^{2.3}$	10^{3}	10^{3}
$\gamma'_{min,p}$	1.25	1.25	1.25	1.25	1.25	1.25
$\gamma'_{max,e}$	$10^{7.6}$	$10^{7.56}$	$10^{7.53}$	$10^{7.55}$	$10^{4.86}$	$10^{5.18}$
$\gamma'_{max,p}$	10^{8}	10^{8}	10^{8}	10^{8}	10^{8}	10^{8}
l'_e	2.4×10^{-3}	2.54×10^{-3}	1.9×10^{-3}	1.67×10^{-3}	1.5×10^{-3}	1.48×10^{-2}
l'_p	1.3×10^{-6}	1.38×10^{-6}	1.03×10^{-6}	9.1×10^{-7}	8.14×10^{-7}	8.06×10^{-6}
T'_{BLR} (K)	2.15×10^{5}	1.07×10^{5}	3.9×10^{4}	2.69×10^{4}	1.39×10^{4}	8.61×10^{3}
l'_{BLR}	0.36	6.32×10^{-2}	5×10^{-3}	1.92×10^{-3}	3.42×10^{-4}	8.65×10^{-5}

Table 3: Code input parameters used for the cases of $\mu = 50$.

$\mu = 70$						
σ	1	3	10	15	30	48.9
Γ	35	17.5	6.36	4.38	2.26	1.4
$\dot{m}$	0.67	0.083	4×10^{-3}	1.3×10^{-3}	1.8×10^{-4}	4.31×10^{-5}
R'_b (cm)	2.36×10^{16}	1.67×10^{16}	1.07×10^{15}	8.35×10^{15}	6×10^{15}	4.73×10^{15}
B' (G)	8.6	10.6	11.68	11.94	12.64	14.4
p	3	2.5	2.2	2.05	1.5	1.2
$\gamma'_{min,e}$	$10^{2.14}$	$10^{2.44}$	$10^{2.66}$	$10^{2.3}$	10^3	10^3
$\gamma'_{min,p}$	1.25	1.25	1.25	1.25	1.25	1.25
$\gamma'_{max,e}$	$10^{7.6}$	$10^{7.56}$	$10^{7.53}$	$10^{7.55}$	$10^{4.86}$	$10^{5.18}$
$\gamma'_{max,p}$	10^8	10^8	10^8	10^8	10^8	10^8
l'_e	2.82×10^{-3}	3×10^{-3}	2.22×10^{-3}	1.92×10^{-3}	1.55×10^{-3}	1.58×10^{-3}
l'_p	1.53×10^{-6}	1.63×10^{-6}	1.2×10^{-6}	1.05×10^{-6}	8.43×10^{-7}	8.6×10^{-7}
T'_{BLR} (K)	3×10^5	1.5×10^5	5.47×10^4	3.76×10^4	1.94×10^4	1.2×10^4
l'_{BLR}	0.83	0.15	1.16×10^{-2}	4.53×10^{-3}	8.36×10^{-4}	2.33×10^{-4}

Table 4: Code input parameters used for the cases of $\mu = 70$.

$\mu = 90$						
σ	1	3	10	15	30	48.9
Γ	45	22.5	8.18	5.63	2.9	1.8
$\dot{m}$	1.42	0.18	8.55×10^{-3}	2.8×10^{-3}	$3.8 times 10^{-4}$	9.17×10^{-5}
R'_b (cm)	2.68×10^{16}	1.89×10^{16}	1.14×10^{16}	9.47×10^{15}	6.8×10^{15}	5.36×10^{15}
B' (G)	8.6	10.55	11.75	11.88	12.36	13.21
p	3	2.5	2.2	2.05	1.5	1.2
$\gamma'_{min,e}$	$10^{2.14}$	$10^{2.44}$	$10^{2.66}$	$10^{2.3}$	10^3	10^3
$\gamma'_{min,p}$	1.25	1.25	1.25	1.25	1.25	1.25
$\gamma'_{max,e}$	$10^{7.6}$	$10^{7.56}$	$10^{7.53}$	$10^{7.55}$	$10^{4.86}$	$10^{5.18}$
$\gamma'_{max,p}$	10^8	10^8	10^8	10^8	10^8	10^8
l'_e	3.2×10^{-3}	3.4×10^{-3}	2.5×10^{-3}	2.16×10^{-3}	1.68×10^{-3}	1.51×10^{-3}
l'_p	1.74×10^{-6}	1.85×10^{-6}	1.36×10^{-6}	1.17×10^{-6}	9.13×10^{-7}	8.22×10^{-7}
T'_{BLR} (K)	3.86×10^5	1.93×10^5	7.03×10^4	4.83×10^4	2.5×10^4	1.55×10^4
l'_{BLR}	1.55	0.27	2.18×10^{-2}	8.54×10^{-3}	1.6×10^{-3}	4.62×10^{-4}

Table 5: Code input parameters used for the cases of $\mu = 90$.

References

[1] Mark Aartsen, Markus Ackermann, Jenni Adams, and Juan Antonio Aguilar. Multimessenger observations of a flaring blazar coincident with high-energy neutrino IceCube-170922a. *Science*, 361(6398), jul 2018.

[2] S. Abdollahi, F. Acero, M. Ackermann, and M. Ajello. ifermi/i large area telescope fourth source catalog. *The Astrophysical Journal Supplement Series*, 247(1):33, mar 2020.

[3] David Ball, Lorenzo Sironi, and Feryal Özel. Electron and proton acceleration in trans-relativistic magnetic reconnection: Dependence on plasma beta and magnetization. *The Astrophysical Journal*, 862(1):80, jul 2018.

[4] Volker Beckmann and Chris R. Shrader. *Active Galactic Nuclei*. 2012.

[5] A. Bhattacharjee, Yi-Min Huang, H. Yang, and B. Rogers. Fast reconnection in high-lundquist-number plasmas due to the plasmoid instability. *Physics of Plasmas*, 16(11):112102, nov 2009.

[6] Wei-Hao Bian and Yong-Heng Zhao. Accretion Rates and the Accretion Efficiency in AGNs. *Publications of the Astronomical Society of Japan*, 55(3):599–603, 06 2003.

[7] R. D. Blandford and D. G. Payne. Hydromagnetic flows from accretion discs and the production of radio jets. *Monthly Notices of the Royal Astronomical Society*, 199(4):883–903, 08 1982.

[8] Elliott D. Bloom et al. Determination of the total photon - proton cross-section from high-energy inelastic electron scattering. In *4th Int. Symposium on Electron and Photon Interactions at High Energies*, 9 1969.

[9] GEORGE R. BLUMENTHAL and ROBERT J. GOULD. Bremsstrahlung, synchrotron radiation, and compton scattering of high-energy electrons traversing dilute gases. *Rev. Mod. Phys.*, 42:237–270, Apr 1970.

[10] Edward M. Cackett, Misty C. Bentz, and Erin Kara. Reverberation mapping of active galactic nuclei: From x-ray corona to dusty torus. *iScience*, 24(6):102557, jun 2021.

[11] D. O. Caldwell, J. P. Cumalat, A. M. Eisner, A. Lu, R. J. Morrison, F. V. Murphy, S. J. Yellin, P. J. Davis, R. M. Egloff, M. E. B. Franklin, G. J. Luste, J. F. Martin, J. D. Prentice, and T. Nash. Measurements of the photon total cross section on protons from 18 to 185 gev. *Phys. Rev. Lett.*, 40:1222–1225, May 1978.

[12] D. O. Caldwell, V. B. Elings, W. P. Hesse, R. J. Morrison, F. V. Murphy, B. W. Worster, and D. E. Yount. Total hadronic (γ, p) and (γ, d) cross sections from 4 to 18 gev. *Phys. Rev. Lett.*, 25:609–612, Aug 1970.

[13] Annalisa Celotti and Gabriele Ghisellini. The power of blazar jets. *Monthly Notices of the Royal Astronomical Society*, 385(1):283–300, 02 2008.

[14] M Cerruti, A Zech, C Boisson, G Emery, S Inoue, and J-P Lenain. Leptohadronic single-zone models for the electromagnetic and neutrino emission of TXS 0506056. *Monthly Notices of the Royal Astronomical Society: Letters*, 483(1):L12–L16, nov 2018.

[15] B. Cerutti, G. R. Werner, D. A. Uzdensky, and M. C. Begelman. THREE-DIMENSIONAL RELATIVISTIC PAIR PLASMA RECONNECTION WITH RADIATIVE FEEDBACK IN THE CRAB NEBULA. *The Astrophysical Journal*, 782(2):104, feb 2014.

[16] I M Christie, M Petropoulou, L Sironi, and D Giannios. Radiative signatures of plasmoid-dominated reconnection in blazar jets. *Monthly Notices of the Royal Astronomical Society*, 482(1):65–82, oct 2018.

[17] M. H. Cohen, M. L. Lister, D. C. Homan, M. Kadler, K. I. Kellermann, Y. Y. Kovalev, and R. C. Vermeulen. Relativistic beaming and the intrinsic properties of extragalactic radio jets. *The Astrophysical Journal*, 658(1):232–244, mar 2007.

[18] Filippo D'Ammando. Relativistic jets in gamma-ray-emitting narrow-line seyfert 1 galaxies, 2019.

[19] Shane W. Davis and Ari Laor. THE RADIATIVE EFFICIENCY OF ACCRETION FLOWS IN INDIVIDUAL ACTIVE GALACTIC NUCLEI. *The Astrophysical Journal*, 728(2):98, jan 2011.

[20] Charles D. Dermer and Govind Menon. *High Energy Radiation from Black Holes: Gamma Rays, Cosmic Rays, and Neutrinos*. 2009.

[21] Charles Dennison Dermer and Berrie Giebels. Active galactic nuclei at gamma-ray energies. *Comptes Rendus Physique*, 17(6):594–616, jun 2016.

[22] S. Dimitrakoudis, A. Mastichiadis, R. J. Protheroe, and A. Reimer. The time-dependent one-zone hadronic model. *Astronomy &amp Astrophysics*, 546:A120, oct 2012.

[23] B. L. Fanaroff and J. M. Riley. The morphology of extragalactic radio sources of high and low luminosity. , 167:31P–36P, May 1974.

[24] G. Fossati, L. Maraschi, A. Celotti, A. Comastri, and G. Ghisellini. A unifying view of the spectral energy distributions of blazars. *Monthly Notices of the Royal Astronomical Society*, 299(2):433–448, sep 1998.

[25] G. Ghisellini, A. Celotti, G. Fossati, L. Maraschi, and A. Comastri. A theoretical unifying scheme for gamma-ray bright blazars. *Monthly Notices of the Royal Astronomical Society*, 301(2):451–468, dec 1998.

[26] G. Ghisellini, L. Maraschi, and F. Tavecchio. The Fermi blazars' divide. , 396(1):L105–L109, June 2009.

[27] G. Ghisellini, C. Righi, L. Costamante, and F. Tavecchio. The fermi blazar sequence. *Monthly Notices of the Royal Astronomical Society*, 469(1):255–266, apr 2017.

[28] G. Ghisellini and F. Tavecchio. The blazar sequence: a new perspective. *Monthly Notices of the Royal Astronomical Society*, 387(4):1669–1680, jul 2008.

[29] G. Ghisellini and F. Tavecchio. The blazar sequence: a new perspective. *Monthly Notices of the Royal Astronomical Society*, 387(4):1669–1680, 07 2008.

[30] Gabriele Ghisellini. *Radiative Processes in High Energy Astrophysics*. Springer International Publishing, 2013.

[31] Dimitrios Giannios. Reconnection-driven plasmoids in blazars: fast flares on a slow envelope. *Monthly Notices of the Royal Astronomical Society*, 431(1):355–363, feb 2013.

[32] Fan Guo, Xiaocan Li, Hui Li, William Daughton, Bing Zhang, Nicole Lloyd-Ronning, Yi-Hsin Liu, Haocheng Zhang, and Wei Deng. EFFICIENT PRODUCTION OF HIGH-ENERGY NONTHERMAL PARTICLES DURING MAGNETIC RECONNECTION IN a MAGNETICALLY DOMINATED ION–ELECTRON PLASMA. *The Astrophysical Journal*, 818(1):L9, feb 2016.

[33] E. G. Harris. On a plasma sheath separating regions of oppositely directed magnetic field. *Il Nuovo Cimento*, 23(1):115–121, January 1962.

[34] Christopher Harrison. *Observational constraints on the influence of active galactic nuclei on the evolution of galaxies*. PhD thesis, Durham University, UK, September 2014.

[35] IceCube Collaboration, M. G. Aartsen, M. Ackermann, J. Adams, and Aguilar. Neutrino emission from the direction of the blazar TXS 0506+056 prior to the IceCube-170922A alert. *Science*, 361(6398):147–151, July 2018.

[36] Predrag Jovanović and Luka Č. Popović. X-ray emission from accretion disks of agn: Signatures of supermassive black holes, 2009.

[37] Shai Kaspi, Dan Maoz, Hagai Netzer, Bradley M. Peterson, Marianne Vestergaard, and Buell T. Jannuzi. The Relationship between Luminosity and Broad-Line Region Size in Active Galactic Nuclei. , 629(1):61–71, August 2005.

[38] Katrin Collaboration, M. Aker, A. Beglarian, and J. Behrens. Direct neutrino-mass measurement with sub-electronvolt sensitivity. *Nature Physics*, 18(2):160–166, February 2022.

[39] A. Keivani, K. Murase, M. Petropoulou, D. B. Fox, S. B. Cenko, S. Chaty, A. Coleiro, J. J. DeLaunay, S. Dimitrakoudis, P. A. Evans, J. A. Kennea, F. E. Marshall, A. Mastichiadis, J. P. Osborne, M. Santander, A. Tohuvavohu, and C. F. Turley. A Multimessenger Picture of the Flaring Blazar TXS 0506+056: Implications for High-energy Neutrino Emission and Cosmic-Ray Acceleration. , 864(1):84, September 2018.

[40] S. R. Kelner, F. A. Aharonian, and V. V. Bugayov. Energy spectra of gamma rays, electrons, and neutrinos produced at proton-proton interactions in the very high energy regime. *Phys. Rev. D*, 74:034018, Aug 2006.

[41] Serguei S. Komissarov, Maxim V. Barkov, Nektarios Vlahakis, and Arieh Königl. Magnetic acceleration of relativistic active galactic nucleus jets. , 380(1):51–70, September 2007.

[42] J. H. Krolik. Magnetized accretion inside the marginally stable orbit around a black hole. *The Astrophysical Journal*, 515(2):L73–L76, apr 1999.

[43] M. L. Lister, M. H. Cohen, D. C. Homan, M. Kadler, K. I. Kellermann, Y. Y. Kovalev, E. Ros, T. Savolainen, and J. A. Zensus. MOJAVE: Monitoring of Jets in Active Galactic Nuclei with VLBA Experiments. VI. Kinematics Analysis of a Complete Sample of Blazar Jets. , 138(6):1874–1892, December 2009.

[44] M. L. Lister, D. C. Homan, T. Hovatta, K. I. Kellermann, S. Kiehlmann, Y. Y. Kovalev, W. Max-Moerbeck, A. B. Pushkarev, A. C. S. Readhead, E. Ros, and T. Savolainen. MOJAVE. XVII. Jet Kinematics and Parent Population Properties of Relativistically Beamed Radio-loud Blazars. , 874(1):43, March 2019.

[45] Malcolm S. Longair. *High Energy Astrophysics*. 2011.

[46] N. F. Loureiro, A. A. Schekochihin, and S. C. Cowley. Instability of current sheets and formation of plasmoid chains. *Physics of Plasmas*, 14(10):100703, oct 2007.

[47] A. Mastichiadis and J. G. Kirk. Self-consistent particle acceleration in active galactic nuclei. , 295:613, March 1995.

[48] A. Mastichiadis, R. J. Protheroe, and J. G. Kirk. Spectral and temporal signatures of ultrarelativistic protons in compact sources. *Astronomy &amp Astrophysics*, 433(3):765–776, mar 2005.

[49] Mickaël Melzani, Rolf Walder, Doris Folini, Christophe Winisdoerffer, and Jean M. Favre. The energetics of relativistic magnetic reconnection: ion-electron repartition and particle distribution hardness. , 570:A112, October 2014.

[50] Leonel Morejon, Anatoli Fedynitch, Denise Boncioli, Daniel Biehl, and Walter Winter. Improved photomeson model for interactions of cosmic ray nuclei. *Journal of Cosmology and Astroparticle Physics*, 2019, 11 2019.

[51] Kohta Murase and Floyd W. Stecker. High-energy neutrinos from active galactic nuclei, 2022.

[52] P. Padovani, D. M. Alexander, R. J. Assef, B. De Marco, P. Giommi, R. C. Hickox, G. T. Richards, V. Smolčić, E. Hatziminaoglou, V. Mainieri, and M. Salvato. Active galactic nuclei: what's in a name? *The Astronomy and Astrophysics Review*, 25(1), aug 2017.

[53] P. Padovani, F. Oikonomou, M. Petropoulou, P. Giommi, and E. Resconi. TXS 0506+056, the first cosmic neutrino source, is not a BL Lac. , 484(1):L104–L108, March 2019.

[54] Paolo Padovani. The blazar sequence: validity and predictions. *Astrophysics and Space Science*, 309(1-4):63–71, apr 2007.

[55] Vaidehi S. Paliya, M. Ajello, S. Rakshit, Amit Kumar Mandal, C. S. Stalin, A. Kaur, and D. Hartmann. Gamma-Ray-emitting Narrow-line Seyfert 1 Galaxies in the Sloan Digital Sky Survey. , 853(1):L2, January 2018.

[56] Andrea Palladino, Xavier Rodrigues, Shan Gao, and Walter Winter. Interpretation of the diffuse astrophysical neutrino flux in terms of the blazar sequence. *The Astrophysical Journal*, 871(1):41, jan 2019.

[57] E. N. Parker. Sweet's mechanism for merging magnetic fields in conducting fluids. *Journal of Geophysical Research (1896-1977)*, 62(4):509–520, 1957.

[58] M. Petropoulou, S. Dimitrakoudis, P. Padovani, A. Mastichiadis, and E. Resconi. Photohadronic origin of $\boldsymbol {\gamma }$-ray BL lac emission: implications for IceCube neutrinos. *Monthly Notices of the Royal Astronomical Society*, 448(3):2412–2429, mar 2015.

[59] Maria Petropoulou, Foteini Oikonomou, Apostolos Mastichiadis, Kohta Murase, Paolo Padovani, Georgios Vasilopoulos, and Paolo Giommi. Comprehensive multimessenger modeling of the extreme blazar 3hsp j095507.9355101 and predictions for IceCube. *The Astrophysical Journal*, 899(2):113, aug 2020.

[60] Maria Petropoulou and Lorenzo Sironi. The steady growth of the high-energy spectral cut-off in relativistic magnetic reconnection. *Monthly Notices of the Royal Astronomical Society*, 481(4):5687–5701, oct 2018.

[61] Maria Petropoulou, Lorenzo Sironi, Anatoly Spitkovsky, and Dimitrios Giannios. Relativistic magnetic reconnection in electron–positron–proton plasmas: Implications for jets of active galactic nuclei. *The Astrophysical Journal*, 880(1):37, jul 2019.

[62] H. E. Petschek. Magnetic Field Annihilation. In *NASA Special Publication*, volume 50, page 425. 1964.

[63] Elisa Prandini and Gabriele Ghisellini. The blazar sequence and its physical understanding. *Galaxies*, 10(1):35, feb 2022.

[64] Jörg P. Rachen and P. Mészáros. Photohadronic neutrinos from transients in astrophysical sources. *Phys. Rev. D*, 58:123005, Nov 1998.

[65] Jesú s M Rueda-Becerril, Amanda O Harrison, and Dimitrios Giannios. Blazar jets launched with similar energy per baryon, independently of their power. *Monthly Notices of the Royal Astronomical Society*, 501(3):4092–4102, dec 2020.

[66] George B. Rybicki and Alan P. Lightman. *Radiative Processes in Astrophysics*. 1986.

[67] Narek Sahakyan. Lepto-hadronic i/i-ray and neutrino emission from the jet of TXS 0506056. *The Astrophysical Journal*, 866(2):109, oct 2018.

[68] R. Samtaney, N. F. Loureiro, D. A. Uzdensky, A. A. Schekochihin, and S. C. Cowley. Formation of plasmoid chains in magnetic reconnection. *Phys. Rev. Lett.*, 103:105004, Sep 2009.

[69] Biplob Sarkar. *Active Galactic Nuclei (AGN) and Xray studies of Galaxy M51*. PhD thesis, 06 2011.

[70] M. Schmidt. 3C 273 : A Star-Like Object with Large Red-Shift. , 197(4872):1040, March 1963.

[71] Lorenzo Sironi, Maria Petropoulou, and Dimitrios Giannios. Relativistic jets shine through shocks or magnetic reconnection? *Monthly Notices of the Royal Astronomical Society*, 450(1):183–191, apr 2015.

[72] Lorenzo Sironi and Anatoly Spitkovsky. PARTICLE ACCELERATION IN RELATIVISTIC MAGNETIZED COLLISIONLESS ELECTRON-ION SHOCKS. *The Astrophysical Journal*, 726(2):75, dec 2010.

[73] Lorenzo Sironi and Anatoly Spitkovsky. RELATIVISTIC RECONNECTION: AN EFFICIENT SOURCE OF NON-THERMAL PARTICLES. *The Astrophysical Journal*, 783(1):L21, feb 2014.

[74] Lorenzo Sironi and Anatoly Spitkovsky. Relativistic Reconnection: An Efficient Source of Non-thermal Particles. , 783(1):L21, March 2014.

[75] Lorenzo Sironi, Anatoly Spitkovsky, and Jonathan Arons. THE MAXIMUM ENERGY OF ACCELERATED PARTICLES IN RELATIVISTIC COLLISIONLESS SHOCKS. *The Astrophysical Journal*, 771(1):54, jun 2013.

[76] P. A. Sweet. The Neutral Point Theory of Solar Flares. In B. Lehnert, editor, *Electromagnetic Phenomena in Cosmical Physics*, volume 6, page 123, January 1958.

[77] Alexander Tchekhovskoy, Jonathan C. McKinney, and Ramesh Narayan. EFFICIENCY OF MAGNETIC TO KINETIC ENERGY CONVERSION IN a MONOPOLE MAGNETOSPHERE. *The Astrophysical Journal*, 699(2):1789–1808, jun 2009.

[78] C. Megan Urry and Paolo Padovani. Unified schemes for radio-loud active galactic nuclei. *Publications of the Astronomical Society of the Pacific*, 107:803, sep 1995.

[79] D. A. Uzdensky, N. F. Loureiro, and A. A. Schekochihin. Fast magnetic reconnection in the plasmoid-dominated regime. *Physical Review Letters*, 105(23), dec 2010.

[80] Nektarios Vlahakis and Arieh Konigl. Magnetic driving of relativistic outflows in active galactic nuclei. i. interpretation of parsec-scale accelerations. *The Astrophysical Journal*, 605(2):656–661, apr 2004.

[81] G. R. Werner, D. A. Uzdensky, M. C. Begelman, B. Cerutti, and K. Nalewajko. Non-thermal particle acceleration in collisionless relativistic electron–proton reconnection. *Monthly Notices of the Royal Astronomical Society*, 473(4):4840–4861, 09 2017.

[82] S. Zenitani and M. Hoshino. Particle acceleration and magnetic dissipation in relativistic current sheet of pair plasmas. *The Astrophysical Journal*, 670(1):702–726, nov 2007.

[83] Hao Zhang, Lorenzo Sironi, and Dimitrios Giannios. Fast particle acceleration in three-dimensional relativistic reconnection. *The Astrophysical Journal*, 922(2):261, dec 2021.